

Novel Materials for Silicon Based Photonics

by

Qingyang Du

B.S., Materials Physics
University of Science and Technology of China, 2012

SUBMITTED TO THE DEPARTMENT OF MATERIALS SCIENCE AND
ENGINEERING IN PARTIAL FULFILLMENT OF THE REQUIREMENTS FOR THE
DEGREE OF

DOCTOR OF PHILOSOPHY

AT THE

MASSACHUSETTS INSTITUTE OF TECHNOLOGY

September 2018

© 2018 Massachusetts Institute of Technology. All Rights Reserved.

Signature of Author: _____
Department of Materials Science and Engineering
August 8th, 2018

Certified by: _____
Juejun Hu
Merton C. Flemings Career Development
Associate Professor of Materials Science and Engineering
Thesis Supervisor

Accepted by: _____
Donald Sadoway
John F. Elliott Professor of Materials Chemistry
Chair, Departmental Committee on Graduate Student

To my grandfather 杜绍明

谨以此论文献给我的祖父，愿您在另一个世界永远快乐

Novel Materials for Silicon Based Photonics

by

Qingyang Du

Submitted to the Department of Materials Science and Engineering on August 8th, in Partial Fulfillment of the Requirement for the Degree of Doctor of Philosophy in Materials Science and Engineering

Abstract

A complete photonic chip must include the following components: a light source, usually lasers, an isolator, a waveguide, a modulator and a photodetector. Limited by material intrinsic properties, silicon alone cannot realize all the above mentioned functions. The development of silicon photonics has found its way through exploiting novel materials as hybrid platforms to manufacture various devices and systems.

In this thesis, we focus on the development of novel material in emerging needs of broadband coherent light source and optical isolators. Chalcogenide glass stands out among the candidates for light generation and sensing due to its large non-linear figure of merit and wide transparency window in the IR spectral range, while magnetic garnet still presents the best device performance among magneto-optical isolators owing to the ease of phase formation and relatively low material absorption.

We first investigated the fabrication technology of chalcogenide glass and developed a process flow to produce low loss planar chalcogenide glass waveguides. Using electron beam lithography to minimize sidewall roughness and reactive ion etch to achieve vertical sidewalls. We managed to demonstrate a record low loss of 0.5 dB/cm in single mode core chalcogenide waveguides. Based on this low loss platform, we integrated a supercontinuum light source onto a sensor chip. Our work presented a step forward towards miniaturization photonic sensor chips.

Next, we focused on a hybrid platform of chalcogenide glass and magnetic garnet. By carefully designing device architecture, a monolithically integrated TM polarized magneto-optical (MO) isolator with 3 dB insertion loss and 40 dB isolation ratio was demonstrated. Both parameter sets record among current monolithically integrated on-chip MO isolators. Meanwhile, we also demonstrated a monolithically integrated MO isolator with TE polarization featuring 11.5 dB insertion loss and 20 dB isolation ratio.

Lastly, we leveraged cavity enhanced spectroscopy platform to study radiation induced effect on SiN_x, a-Si and SiC materials. We found a refractive index modulation to the order of 10⁻³ after receiving 10 Mrad Gamma radiation dose.

Thesis supervisor: Juejun Hu

Title: Merton C. Flemings Career Development Associate Professor of Materials Science and Engineering

Table of Content

Abstract	5
Acknowledgement	12
Chapter 1. Introduction	17
1.1 Limitations and Challenges in Silicon Photonics	17
1.2 Chalcogenide glass material	18
1.3 Magnetic garnet oxide material	20
1.4 Thesis outline.....	21
Reference.....	23
Chapter 2. Low Loss Chalcogenide Glass Photonics	24
2.1 Chalcogenide Glass as Waveguide	24
2.2 Current Fabrication Technologies of Chalcogenide Glass Photonics	25
2.3 Fabrication Process Optimization	26
2.4 Loss Analysis	32
2.5 Conclusion.....	36
Reference.....	37
Chapter 3. On-Chip Supercontinuum Integrated Chalcogenide Chemical Sensor ..	38
3.1 Limitation of Current Photonic Sensor Chips	38
3.2 On-Chip Supercontinuum Generation in Chalcogenide Glass	39
3.3 Demonstration of Chloroform Sensing	46
3.4 Conclusion.....	48

Reference.....	49
Chapter 4. Monolithically Integration of On-chip Magneto-optical Isolators	51
4.1 Magneto-optical (MO) Effect	51
4.2 Introduction to isolator	53
4.3 Magnetic Garnet	58
4.4 Novel Design of next generation TM isolator	62
4.5 Demonstration of next generation TM isolator	67
4.6 TE MO isolators	79
4.7 Discussion and outlook	82
4.8 Conclusion.....	86
Reference.....	87
Chapter 5. Radiation Induced Effects in Silicon Photonic Materials and Devices ...	90
5.1 Radiation Overview	90
5.2 Stopping Range of Ions in Mater (SRIM)	91
5.3 Gamma Radiation Damage in a-Si and SiN _x Materials and Devices	96
5.4 Gamma Radiation Damage in a-SiC Materials and Devices	105
5.5 Conclusion.....	108
Reference.....	109
Chapter 6. Conclusion and Future Work	111
5.1 Radiation Overview	111
5.2 Stopping Range of Ions in Mater (SRIM)	112

List of Figures

- Figure 1-1** *A Comparison of transparency window of silica, silicon, chalcogenides, heavy-metal oxides and halides is shown on the bottom. The window is matched to the scale of optical spectrum shown above. On top of the figure, typical functional groups absorption region are displayed. We can see that chalcogenide glass covers most of their spectral range.* 12
- Figure 1-2** *Crystal structure of yttrium ion garnet. The pink and blue region marked tetrahedral site and octahedral site, respectively.* 14
- Figure 2-1** *SEM images of: a, b) chlorine-etched GSS waveguides with silicon oxide passivation coating; the grainy surface texture comes from gold coating applied to reduce electrostatic charging during SEM imaging; c) chlorine-etched GSS waveguide without silicon oxide passivation coating; d, e) fluorine-etched GSS waveguides.* 23
- Figure 2-2** *a) Schematic diagram showing the XPS tilted beam analysis configuration. The grating has a 400 nm line width with 800 nm period. b) XPS spectrum showing the presence of Si and O, and trace amounts of C, F in the coating layer.* 24
- Figure 2-3** *Optical microscope images of fabricated a) micro-disk and b) micro-ring resonators. c-d) Transmission spectra of c) micro-ring resonator; and d) micro-disk resonator etched using the fluorine chemistry. The red curves are Lorentzian fit of the spectra* 27
- Figure 2-4** *Waveguide sidewall roughness analysis example: a) SEM top-view image of a fluorine etched waveguide; the grainy surface texture comes from gold coating applied to reduce electrostatic charging during SEM imaging. b) Waveguide edge extracted from the SEM image. c) PSD function of sidewall roughness (black line). The red line represents exponential model fit.* 28
- Figure 3-1** *(a) Refractive index dispersion of the $Ge_{22}Sb_{18}Se_{60}$ glass film measured using ellipsometry; inset schematically depicts the waveguide structure; (b) Simulated GVD of GeSbSe waveguides with varying widths (W) and a fixed core thickness $H = 400$ nm.* 34
- Figure 3-2** *(a) Top-view optical micrograph of the zigzag GeSbSe waveguides; (b) SEM cross-sectional image of a $0.95 \mu m$ (W) \times $0.4 \mu m$ (H) GeSbSe waveguide; (c) The experimental setup of on-chip SC generation and sensing; (d) Block diagram of home-built femtosecond laser module (OC: Optical coupler, WDM: wavelength division multiplexer, SA: graphene saturable absorber, PC: polarization controller)* 36

- Figure 3-3** *SC spectra in GeSbSe waveguides: (a) SC spectra from waveguides with different widths W ; when $W = 0.95 \mu\text{m}$, the zero-dispersion point of the waveguide coincides with the pump wavelength; (b) SC generation of GeSbSe waveguides with the optimal geometry ($W = 0.95 \mu\text{m}$, $H = 0.4 \mu\text{m}$) and varying lengths; (c) SC spectra from a 21-mm-long GeSbSe waveguide ($W = 0.95 \mu\text{m}$, $H = 0.4 \mu\text{m}$) at different pump power levels. The power quoted here represent the average optical power coupled into the waveguide.* 38
- Figure 3-4** *(a) SC spectra measured on GeSbSe waveguides of different lengths L when immersed in chloroform; the triangle marks the optical absorption at 1695 nm calibrated using a benchtop UV-Vis spectrometer for an equivalent waveguide path length $L = 21$ mm; (b) SC spectra taken on a 21-mm-long GeSbSe waveguide immersed in $\text{CHCl}_3\text{-CCl}_4$ solutions of varying volume concentration ratios; (c) measured peak absorption at 1695 nm versus the GeSbSe waveguide length used in the experiment: the linear relation indicates that the classical Lambert's law is obeyed; inset shows the mode profile simulated by finite difference method.* 40
- Figure 4-1** *(a) Schematic of a nonreciprocal optical resonator structure and cross-section (inset) through the garnet-clad section of the Si waveguide. (b) Schematic showing a Faraday rotation waveguide isolator and cross-section (inset) of the garnet-clad waveguide. (c) Cross-sectional image of a fabricated one-dimensional magneto-photonic crystal consisting of magneto-optical garnet (Ce:YIG, cerium-doped yttrium iron garnet) between two Bragg mirrors. (d) Schematic and cross-section (inset) of a Mach-Zehnder transverse electric (TE) mode isolator with Ce:YIG mesas adjacent to the sidewalls of the waveguide. Note: a-Si:H, hydrogenated amorphous silicon.* 49
- Figure 4-2** *(a) X-ray diffraction (θ - 2θ scans of pulsed laser deposition cerium-doped yttrium iron garnet (Ce:YIG) and YIG multilayer garnet films after rapid thermal annealing at 800 °C for 5 min on silicon, showing characteristic garnet peaks.] (b) Scans of sputtered TbIG (TIG, terbium iron garnet) on Si and quartz substrates, showing characteristic garnet peaks. (c) In-plane hysteresis loops and (d) out-of-plane Faraday rotation hysteresis loops at a wavelength (λ) of 1550 nm, with magnetic field and light propagation perpendicular to the film, for sputtered Ce:YIG on Si substrates annealed at 800 °C for various times. Inset shows the saturation Faraday rotation dependence on annealing time.] (e) Bright-field transmission electron microscope (TEM) cross-sectional image of YIG/Ce:YIG/silica/Si, showing large grained YIG top seed layer and fine grained Ce:YIG. Inset shows the high resolution TEM image of the interface between the film and Si substrate (f) Spectral dependence of figure of merit (FOM) of single-crystal Ce:YIG films with different crystal orientation on a garnet substrate, with magnetic field and light propagation perpendicular to the film.* 53

- Figure 4-3** (a) Schematic transmission spectra of a resonator isolator; (b) resonator isolator structure demonstrated in [6]; (c) cross-sectional SEM image of a SOI waveguide covered with deposited magneto-optical oxides; (d) breakup of loss contributions in the isolator device in [6]. 56
- Figure 4-4** (a) Tilted-view and (b) cross-sectional schematic of the new isolator design; (c) nonreciprocal phase shift and waveguide figure of merit computed as functions of the strip-loaded waveguide core refractive index: the insets are modal profiles of strip-loaded waveguides when the core material is chosen as silicon nitride ($n = 2.0$), GeSbSe glass ($n = 2.7$), and amorphous silicon ($n = 3.6$), where the scale bars correspond to 500 nm; (d) fabrication process flow for the isolator device. 61
- Figure 4-5** (a) Top-view optical micrograph of a fabricated resonator isolator; (b) cross-sectional SEM image of the strip-loaded waveguide showing the layer structures 65
- Figure 4-6** (a) Experimental setup for characterization of the isolator device: (1) and (2) indicate optical paths used to interrogate the device in forward and backward propagating directions, respectively; (b) transmission spectra of the isolator: inset shows the same spectra over several free spectral ranges of the resonator; (c) resonant peak wavelengths of the device repeatedly measured for 5 consecutive times; (d) spectral dispersion of the nonreciprocal resonant wavelength shift measured in the isolator. 66
- Figure 4-7** Transmittance spectrum of a strip loaded GeSbSe racetrack resonator on a SiO₂ substrate with vertical tapers. 72
- Figure 4-8** (a) optical microscope image (top view) of as-fabricated SiN racetrack isolator. (b) forward and backward transmission spectrum of SiN isolator, we observed a 15 pm peak shift. (c) cross-sectional SEM image at the window region. (d) Recorded transmission peak position of SiN racetrack isolator. The measurement was conducted by switching light propagation direction for 5 times consecutively. 74
- Figure 4-9** (a) Quasi-transverse magnetic (TM) mode profile and (b) cross-sectional structure of a magneto-optical (MO)-film capped silicon-on-insulator (SOI) waveguide; (c) ratio of waveguide nonreciprocal phase shift and the Faraday rotation of the MO material in the SOI waveguide illustrated in (b); the dotted line delineates the waveguide single-mode (left) and multi-mode (right) regimes. (d) Simulated insertion losses of isolators versus the MO material figure of merit (FOM). Three different device configurations: micro-ring, Faraday rotator, and Mach-Zehnder interferometers (MZI) are compared. Here, the micro-ring and MZI isolators consist of SOI waveguides shown in (b) with a core width of 450 nm and a height of 220 nm. The dotted line corresponds to the best experimentally assessed FOM in deposited cerium-doped yttrium iron garnet (Ce:YIG) films. 78

Figure 5-1	<i>Stopping range plot of alpha particles with different energies.</i>	85
Figure 5-2	<i>LET and NIEL of alpha particle damage with energies ranging from 20KeV to 100KeV on silicon nitride film. From the simulation, we conclude that for silicon nitride device with 400 nm thickness, alpha irradiation with energy of ~60 keV should be chosen in our irradiation experiments as it can induce most damage inside the material, and can yield insights into the upper and lower limits for rad-hardness.</i>	86
Figure 5-3	<i>Transmission spectra of silicon nitride resonators before and after alpha irradiation</i>	88
Figure 5-4	<i>(a) Top-view optical microscope image of an a-Si micro-ring resonator; (b) transmission spectra of the a-Si resonator before (black curve) and after (red curve) receiving 2 Mrad gamma irradiation</i>	90
Figure 5-5	<i>HRTEM images of a-Si sample before (a) and after (b) 20 Mrad radiation. (c) and (d) are the corresponding images of a SiN_x film before and after radiation under same dose. (e) and (f): XRD spectra of a-Si and SiN_x thin film before and after 20 Mrad gamma irradiation, respectively.</i>	93
Figure 5-6	<i>(a) and (c): Si 2p peak from a high resolution XPS scan of as-deposited (a) a-Si and (c) SiN_x films. The spectra are deconvoluted into different Si bonding states, where the red curves correspond to Si-O bond, the blue curve are assigned to Si-Si bond and the pink curves are associated with Si-N bond. The Insets show the sums of the deconvoluted peaks, indicating good fitting quality; (b) and (d) calculated surface Si-O bond fraction for (b) a-Si and (d) SiN_x samples irradiated in argon (red) and ambient air (black).</i>	95
Figure 5-7	<i>Dependences of refractive index changes on cumulative gamma radiation dose in (a) a-Si and (b) SiN_x inferred from optical resonator measurements.</i>	96
Figure 5-8	<i>(a) Optical microscope image silicon carbide micro-resonator; (b) Optical mode of the fabricated silicon carbide waveguide with 1 μm width; SEM micrographs are shown (c) top view and (d) cross section, respectively.</i>	99
Figure 5-9	<i>(a) Transmission spectra of silicon carbide resonator before and after 2 Mrad gamma radiation in air; (b) quantitative analysis of peak shift with respect to radiation dose; (c) linear extrapolation of effective index change, the result shows a 0.0015 index change in silicon carbide material after receiving 2 Mrad. (d) silicon carbide core refractive index change with radiation dose.</i>	100

Acknowledgement

After staring at this blank page for nearly half an hour, I finally starting typing this very last part of my PhD thesis. Memories of the past four years flashes back and forth in front of my eyes. Happiness and bitterness, joys and tears. It is the time I spent with those around me made my life in MIT. I would like to take this special opportunities to express my gratitude to all of you.

I first would like to express my deepest respect and gratitude to my advisor Prof. Juejun Hu. During your six years of mentorship, you have always been like a father who would instruct me and guide me with patience and wisdom. You never give me up when I make serious mistakes and it is you who always have faith in me correcting my problems. You have also been like a friend who would share his life stories and give me courage when I was down. It is your passion that fascinated me into the field of photonics and your wisdom that illuminated my research directions. Your excellent leadership of the group, addiction to science and broad visions are the valuable treasure I always admire and learn from. Thank you JJ.

Next, I would like to thank Dr. Jurgen Michel and Prof. Caroline Ross as my thesis committee members. Both of your suggestions benefited me on my research works. Dr. Michel's smart mind always shed light upon me when I went into a problem I could not solve. Prof. Ross is so nice to work with. You generously shared me access to all your lab

equipment where I learned plenty of skills from. I also like your lecture on magnetic materials and it filled my knowledge gap of magnetism in materials.

I also would like to thank Prof. Lionel C. Kimerling and Dr. Anuradha Aggarwal. Kim offered me a TA in 2017 spring, where I gained my first experience with teaching. You gave me lots of freedom in developing my own teaching skills and give your experiences on being a good teacher. I worked with Dr. Anu on a research project about radiation induced damage effect in photonic chips. Anu is nice to work with and discussion with you has been very helpful in my researches. I feel our fruitful collaboration full of pleasant.

I would like to thank the entire PMAT family. Dr. Tian Gu, Dr. Yi zou, Prof. Hongtao Lin, Dr. Okechukwu Ogbuu, Dr. Lan Li, Dr. Mikhail Shalaginov, Dr. Haijie Zuo, Dr. Shaoliang Yu, Dr. Carlos A. Rios Ocampo, Dr. Samuel Serna-Otalvaro. Duanhui Li, Derek Kita, Jerome Michon, Sarah Geiger, Gufan Yin, Yifei Zhang, Skylar Deckoff-Jones and Bin Huang. Discussion and doing research with you have always been very helpful. I appreciate all your kindness and I enjoy all my time with you.

I would like to express my thanks to my close collaborators and friends in academia, Prof. Lei Bi, Prof. Qinghui Yang, Prof. Li Zhang, Prof. Zhengqian Luo, and Prof. Wei Zhang. I benefitted a lot both in knowledge and vision from discussion on our researches project. In addition, you are also my close friends in my life. Your generosity and companionship make me warm in my heart. I do miss the days we work and dine together.

I would like to thank my close friends in MIT. Dr. Zhaohong Han, Dr. Junying Li, Dr. Yizhong Huang, Huizhang Zhong and Duanhui Li. “A friend in need is a friend indeed”. You are the ones I can turn into when I’m overwhelmed and depressed. You always are so considerate and nice to me. The days we did research, had fun and dined together shapes my best memories in MIT.

I would like to thank my close friends in UD as well. Xuesong Liu, Dr. Jin Sha, Dr. Zeguang Zou, Chang Liu, Xinhui Jiang, Dr. Changgen Mei, Dr. Xi Lin and Jing Zhang. You are the ones I first meet when I’m alone in a foreign country for the first time. Your companionship and friendship are the most valuable treasure to me. You walked me through the most challenging days in life. Thank you all.

我要在此感谢我的父母，你们从小对我的耐心抚养和教导才让我有了能站在 MIT 舞台上的今天。你们坚忍不拔永不言败的性格与勇往直前的勇气深深影响着我。我爱你们，祝你们永远健康快乐。

I would like to thank all the board members of Chinese Students and Scholars Association (CSSA), after joined CSSA in 2014. I really enjoyed each culture event and seminars hosted by CSSA. The board meeting every two weeks enhanced my communication skill and strategic decision making. It is CSSA that made my life colorful and benefited me from detailed event planning skills and leaderships. I owe CSSA family a big thanks.

Lastly, I would like to express my special thanks and deep affection to Yaner, my closest partner in research and my love in life. You are an angel who shines the sunlight into the darkness and lights up my sky. The time we spent together are the sweetest and the most cherishing days in my life. Whatever life holds in store for us, hand in hand, faith to faith. Believe in our love, nothing can stop us.

Chapter 1. Introduction

1.1 Limitations and Challenges in Silicon Photonics

Silicon microphotronics, active and passive planar photonic components employed in monolithic electronic-photonic circuits, is a preferred platform for power efficient, high performance computing, imaging and sensing systems. This synergistic chip functionality provides distance independent communication with $\times 10^3$ improvements in energy-delay product and bandwidth density. Given the wide range of emerging applications, the development of silicon photonics are still hindered by its limitations: First, silicon material has limited transmittance at UV-vis and mid-IR or longer spectral range. It greatly stopped silicon photonics as candidates of applications in waveguiding and sensing in those wavelengths. In addition, unlike electronics, silicon, as a single crystalline photonic material, which requires a lower index cladding material to confine light, has intrinsic epitaxial growth requirement. Current silicon photonics strongly relies on SmartCut technology to make silicon-on-insulator (SOI) wafers, which is costly and up to \sim \$1000 per wafer. Moreover, large two-photon absorption in silicon makes the material lossy when using high powers and in nonlinear photonics. Therefore, researchers has developed a wide range of other materials, including silicon nitride, amorphous and polysilicon as well as glass materials, metal oxides and semiconductors as hybrid platform to fulfill those application requirements. In this thesis, we focus on chalcogenide glass as waveguide guiding and garnet oxide as hybrid platform to realize on-chip sensing and on-chip isolation device chips.

1.2 Chalcogenide Glass Material

Chalcogenide glasses are referred to a broad family of inorganic amorphous materials containing one or more Group IV chalcogen elements, namely sulfur, selenium, and tellurium. Chalcogenide glasses, like their counterpart oxides, lacks long range order where atoms are connected via glass networks. This amorphous feature allows chalcogenide glass easily be integrated onto any substrate via thermal evaporation [1]. In addition, Unlike SiO₂ and other oxide glasses, chalcogenide glass comp rise of heavy atoms, such as Se, Sb and Te. These ions have lower phonon energy which give rise to its well-known wide transparency window [2]. (Fig. 1-1) Therefore, chalcogenide glass has been widely used as waveguiding and sensing platform in IR spectral range [3, 4]. Moreover, chalcogenide glass yields higher Kerr non-linear figure-of-merit (FOM) which is defined as equation 1:

$$\text{FOM} = n_2/\alpha_2 \quad (1)$$

where n_2 is the non-linear refractive index associated with third order nonlinear susceptibility (χ_3), and α_2 is the non-linear loss. According to Miller's rule [5], the third order susceptibility is usually to the quadrant of first order susceptibility. Therefore, larger linear refractive index chalcogenide glass usually has much higher n_2 value than those in oxide glasses. Meanwhile, nonlinear absorption also can happen in chalcogenide glass, where two photon absorption (TPA) is the dominant loss contributor. In this process, free carriers in the valence band can absorb multiple photons to reach conduction band. Compared with semiconductors, low concentration of free carriers in the glass networks makes the nonlinear absorption small. Based on the discussion above, chalcogenide glasses exhibited both high Kerr non-linear refractive index and low non-linear absorption (i.e.

high non-linear FOM) and hence chalcogenide glass has been a better candidates than semiconductors in nonlinear optics.

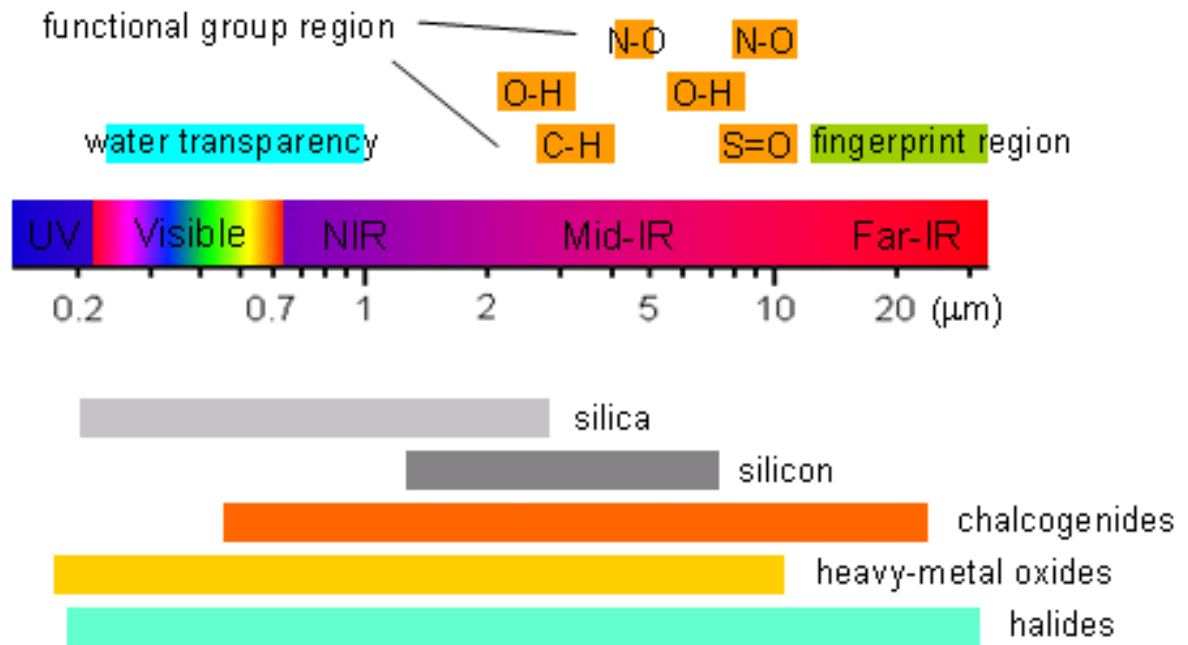


Figure 1-1. A Comparison of transparency window of silica, silicon, chalcogenides, heavy-metal oxides and halides is shown on the bottom. The window is matched to the scale of optical spectrum shown above. On top of the figure, typical functional groups absorption region are displayed. We can see that chalcogenide glass covers most of their spectral range.

1.3 Magnetic Garnet Oxide Material

Magnetic garnet are cubic crystals having 8 chemical formula per unit cell. The formula of garnets are $\{c^{3+}\}_3[a^{3+}]_2(d^{3+})_3O_{12}$, this means there are three possible sites per unit cell for a cation with respect to its surrounding oxygen anion. The dodecahedral sites {c} are usually occupied by large rare earth atoms, like Ce, Y, and Bi, while the octahedral site [a] and tetrahedral site (b) are occupied by smaller atoms like Fe and Al. The crystal structure of $Y_3Fe_5O_{12}$ (YIG) is shown in Figure 1-2. Due to 180 degree superexchange effect, [a] site and (b) site are coupled antiferromagnetically, resulting in a ferrimagnetic crystal.

Typically, to enhance magneto-optical effect, YIG is usually doped with Ce and Bi. Electron transitions in Ce^{3+} are magnetically coupled to Fe^{3+} in Ce:YIG [33] while 6s2 electrons of Bi promotes the orbital splitting of Fe^{3+} in Bi:YIG [32], where both cases contributed to larger magneto-optical effects. However, monolithic integration of these materials has been challenging due to large lattice mismatch of YIG (12.376 Å) and Si (5.43 Å). In addition, coefficient of thermal expansion of YIG ($10.4 \times 10^{-6}/^{\circ}C$) is more than 4 times larger than that of Si ($2.33 \times 10^{-6}/^{\circ}C$). Monolithically integration of polycrystalline YIG film on Si is possible. Nevertheless, cracks tends to form when YIG thickness exceeds certain critical value. [36] Therefore, development of monolithic integration technology of garnet oxide onto Si is the key to make high performance devices.

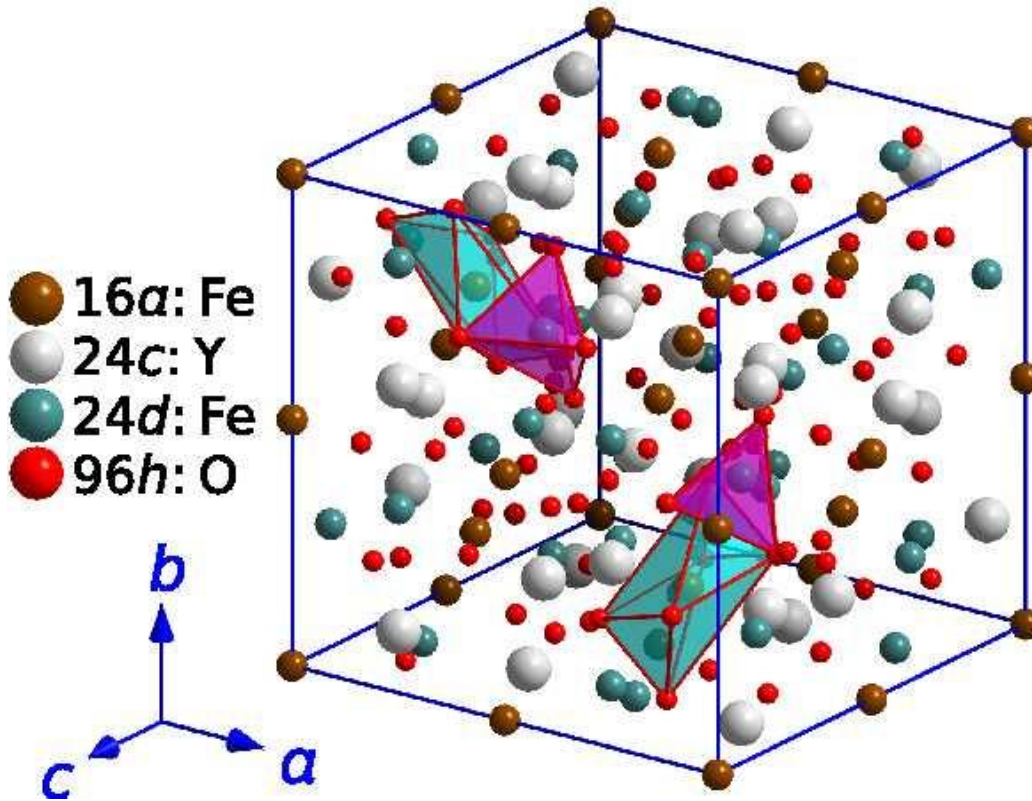


Figure 1-2. Crystal structure of yttrium ion garnet. The pink and blue region marked tetrahedral site and octahedral site, respectively.

1.4 Thesis Outline

In this thesis, we focused on solving the challenges and limitations by integrating chalcogenide glass and magnetic garnet oxide into silicon photonics. We introduced two types of devices: a light source integrated chemical sensor chip and a magneto-optical isolator.

Chapter 1 presented the motivations of exploring novel materials for silicon photonics, and the fundamentals of the two materials: chalcogenide glass and garnet oxide are introduced. In chapter 2, we compared current fabrication technology of making chalcogenide glass photonics and exploited a process utilizing electron-beam-lithography and reactive ion etching to produce low loss chalcogenide glass waveguides and resonators. Our results represented the lowest propagation loss in single mode core chalcogenide glass waveguides. Chapter 3 introduced the work of the first monolithic combination of a supercontinuum light source and a sensor on to a single chip. We made use of large non-linear FOM and wide transparency window advantages of chalcogenide glass. Pumped by a femto-second laser and immersed in chemicals, the chip exhibited excellent broadband coherent light generation without compromising its sensing capabilities. An ultra-compact sensor system could be built if we combine this sensor chip with palm-sized fs-laser and on-chip digital FTIR spectrometer. In Chapter 4, we dedicated to optimize the device performance metrics using facile designs and improved film deposition technology of magneto-optical isolators. Combining material design and device engineering, we successfully reduced the insertion loss to 3 dB and increased the isolation ratio to 40 dB, both values sets the record in current monolithically integrated TM-polarized magneto-optical isolator. The device architecture had a strip-loaded chalcogenide glass strip-loaded waveguide and a garnet oxide cladding. In the meantime, we demonstrated the first monolithically integrated non-reciprocal phase shift based magneto-optical isolator with TE polarization. This device featured an insertion loss of 11.5 dB and 20 dB of isolation ratio. Finally, as a growing trend in the development of silicon photonics, silicon photonic chips are starting to be widely used in radiation-hard environments for example near nuclear reactor and in space. In chapter 5, we conducted a

systematic study of radiation induced effects in SiN_x, a-Si and SiC, all of which are commonly used materials in silicon photonics. We found a modification of refractive index to the order of 10⁻³ while no obvious change in extinction coefficient after receiving up to 10 Mrad cumulative gamma radiation dose. We also developed a technology of making radiation hard devices by engineering the device structure.

Reference

- (1) J. Hu, V. Tarasov, N. Carlie, L. Petit, A. Agarwal, K. Richardson, and L. Kimerling, *Opt. Mater.* **30**, 1560 (2008).
- (2) J. Hu, N. Carlie, L. Petit, A. Agarwal, K. Richardson, and L. C. Kimerling, *J. Lightwave Technol.* **27**, 5240-5245 (2009)
- (3) J. Hu, V. Tarasov, N. Carlie, L. Petit, A. Agarwal, K. Richardson, and L. C. Kimerling, *Opt. Express* **15**, 2307 (2007).
- (4) J. Hu, N. Feng, N. Carlie, J. Wang, L. Petit, A. Agarwal, K. Richardson, and L. C. Kimerling, *Opt. Express* **15**, 14566 (2007)
- (5) E. Vogel, M. Weber, and D. Krol, *Phys. Chem. Glasses* **32**, 231-254 (1991).
- (6) M. Gomi, H. Furuyama and M. Abe, *J. J. Appl. Phys.*, **29**, L99 (1991)
- (7) G. F. Dionne and G. A. Allen, *J. Appl. Phys.*, **75**, 6372 (2004)
- (8) T. Boudiar, B. Payet-Gervy, M. -F. Blanc-Mignon, J. -J. Rousseau, M. Le Berre and H. Joisten, *J. Magn. Magn. Mater.* **284**, 77 (2004)

CHAPTER 2

Low Loss Chalcogenide Glass Photonics

2.1 Chalcogenide Glass as Waveguide

Chalcogenide glasses are glass materials containing chalcogen atoms (S, Se and Te). They are widely recognized as the material of choice for all-optical signal processing and sensing due to its wide transparency window in mid-infrared [1-13]. Their high Kerr non-linearity and low two photon absorption (i.e. high non-linear figure of merit) gives the advantages in non-linear light generation and modulation [1, 3]. In addition, the amorphous nature and room temperature processes allows chalcogenide glass to integrate onto any substrate without considering epitaxial lattice match and thermal budget. This unique feature makes chalcogenide glass suitable for flexible integration [4]. In general, their high refractive index and small mode volume allow chalcogenide glass to suffer less from parasitic excessive radiative losses compared to silica glasses. In fact, chalcogenide glass has been widely used as waveguides in Mid-IR optical fibers and in particular, Vanier [13] has demonstrated a propagation loss as low as 0.002 dB/cm in a chalcogenide microsphere resonators. However, the technology of fabricating low loss integrated chalcogenide glass waveguides are still not fully developed as losses are reported to be 0.05 dB/cm for large core rib waveguide [11] and 0.84 dB/cm for single mode waveguide [12]. This is more than an order of magnitude higher than that in optical fibers. It is apparent fabrication induced sidewall roughness are the dominant loss contributors for on-chip chalcogenide glass waveguide.

In this chapter, we compare current existing fabrication technology and proposed an optimized process for on-chip chalcogenide glasses.

2.2 Current Fabrication Technologies of Chalcogenide Glass Photonics

Planar chalcogenide glass photonic device fabrication using standard semiconductor microfabrication techniques has been studied extensively. Those techniques include plasma dry etching[11, 12], wet etching [6], ion milling [7], nanoimprint [8,9] and lift-off [10]. In wet etching, chips are immersed in liquid solutions to trigger chemical reactions of chemical etching. The etching is usually isotropic and difficult to control the etching profile. Creating vertical and smooth sidewalls are extremely challenging and thus not applicable in mass production lines. In contrast, ion milling, which uses high energy ions, usually Ar^+ , to bombard away materials to be etched. Benefitting from high etching ability to various materials and achieving highly vertical sidewalls, ion milling stands as a better candidate than wet processes. However, lacking of etching selectivity and low etch rate have strongly limited ion milling technology to hard material (high Z number elements) etching process in current fabrication lines. Lift-off processes, where film deposition is performed after chip patterning, have advantages in producing residue-free waveguides after lift-off. This technology is still limited in CMOS lines due to relatively low fabrication yield and tolerance. In nanoimprint technology, a PDMS stamp model is first build and then thermally pressed onto chalcogenide glass chips while heating near its glass transition temperature. The waveguide will be formed thermodynamically and yields smooth sidewalls. Yet, the complex process does not meet large scale fabrication standard. Dry

plasma etching technologies, including inductive coupled plasma (ICP) etching and reactive ion etching (RIE), are the most commonly used process in current fabrication foundries. These technologies provide near vertical sidewall and high fabrication yield. In addition, fast etching rate and highly selective etching chemistry enabled precise etching control. Therefore, we focused on study on plasma dry etching technology

2.3 Fabrication Process Optimization

Our prior work had relied on UV photolithography for ChG microphotonic device fabrication, although large sidewall roughness (10-15 nm root mean square [15]) due to the limited feature resolution can compromise the resulting device performance. In this paper, we report a systematic study of low-loss ChG device processing using electron beam lithography coupled with reactive ion dry etching. Compared to UV photolithography, electron beam (e-beam) lithography is known to offer deep-sub-micron resolution and significantly reduced pattern edge roughness, and is therefore suited for low-loss, high-index-contrast ChG device processing. Both chlorine and fluorine etching gases are investigated, as both chemistries have been adopted for low-loss ChG device patterning [11, 12].

The ChG devices were fabricated on 6" silicon wafers with 3 μm thermally grown oxide coating (Silicon Quest International). A piranha clean was performed prior to film deposition to remove any organic residue from the wafer surface. Subsequently, $\text{Ge}_{23}\text{Sb}_7\text{S}_{70}$ (GSS) bulk glass prepared by conventional melt/quench protocols previously reported [16]

was thermally evaporated onto the wafer to form a 450-nm-thick ChG film using established protocols [16]. We chose the GSS composition over the classical As_2S_3 or As_2Se_3 systems given the superior oxidation-resistance of GSS glass, whereas As_2S_3 or As_2Se_3 glasses are prone to surface oxidation [9]. The deposition rate was maintained at 15 Å/s. A 400-nm-thick ZEP-520A resist (ZEON Chemicals) layer was then spun onto the glass film and exposed by an Elionix ELS-F125 e-beam lithography tool using a beam current of 10 nA. The resist was then developed by immersing in ZED-N50 (ZEON Chemicals) for 1 minute to reveal the patterns.

Reactive ion etching was then carried out on a PlasmaTherm reactive ion etching (RIE) tool (PlasmaTherm Inc.). Both chlorine and fluorine chemistries were investigated. In both cases, the gas flow rate, chamber pressure, radio-frequency (RF) power and etching gas ratio (for the fluorine chemistry) were systematically varied to determine the optimal etching recipes which generate photonic devices with minimal loss (detailed results not shown). Table 1-1 summarizes the optimized etching parameters for both chemistries. Channel waveguides with cross-sectional dimensions of 800 nm \times 450 nm were fabricated by etching through the entire GSS layer. After etching, remaining resists were stripped by soaking the sample in N-Methyl-2-pyrrolidone (NMP) for 2 hours and then sonicating for 30 seconds. The fluorine etched samples underwent an additional oxygen plasma treatment step to remove the fluorocarbon polymer deposited on the waveguide sidewalls formed during the plasma process.

Table 1-1. Summary of the etching conditions for Chlorine chemistry and Fluorine chemistry

	<i>Chlorine</i>	<i>Fluorine</i>
Chemistry	Cl ₂	CHF ₃ :CF ₄
		3:1
Gas flow rate (sccm)	24	45:15
Pressure (mTorr)	10	5
RF Power (W)	200	200

Figure 2-1 shows the top-view and cross-sectional SEM images of GSS waveguides prepared using the recipe listed in Table 1. As seen in Fig 2-1a, chlorine-etched waveguides feature a clean, residue-free morphology consistent with previous report [12]. However, the chlorine-etched waveguide sidewalls are encapsulated by a thin coating layer (the white lines on the waveguide edges shown in Fig. 2-1a) with a composition different from that of GSS, evidenced by the secondary electron image contrast in Fig. 2-1b. In some cases, the coating layer was also formed on the ZEP resist sidewalls, which upon resist removal resulted in a "bunny ear" geometry protruding on top of the waveguide (Fig. 2-1b). We performed X-ray Photoelectron Spectroscopy (XPS) titled beam analysis to ascertain the

coating layer composition. In the experiment, a GSS grating sample was prepared using the same set of parameters used to etch the waveguide devices. Fig. 2-2a illustrates the XPS interrogation configuration: the grating duty cycle and height as well as the X-ray incident angle are chosen so that the X-ray beam pre-dominantly interacts with the grating line sidewalls (and top surface of grating lines to a much lesser extent) to exclude spurious signals from the substrate. Since XPS is a surface-sensitive technique with typical penetration depths less than 10 nm, the XPS spectrum shown in Fig. 2-2b represents the surface coating layer composition. The XPS result indicates that the coating contains Si, O, C (a common atmospheric contaminant routinely observed on samples exposed to ambient environment) and trace amount of F which is likely introduced from the etching chamber. Furthermore, the coating can be removed by rinsing the sample in dilute HF solutions. We therefore conclude that the coating layer mostly consists of silicon oxide. This is not surprising since the plasma etching chamber we used was located in a shared facility and was therefore routinely used for etching silicon compounds. In fact, similar silicon oxide coatings were identified on plasma etched III-V semiconductor nanostructures [17] for the same reason as we identified here.

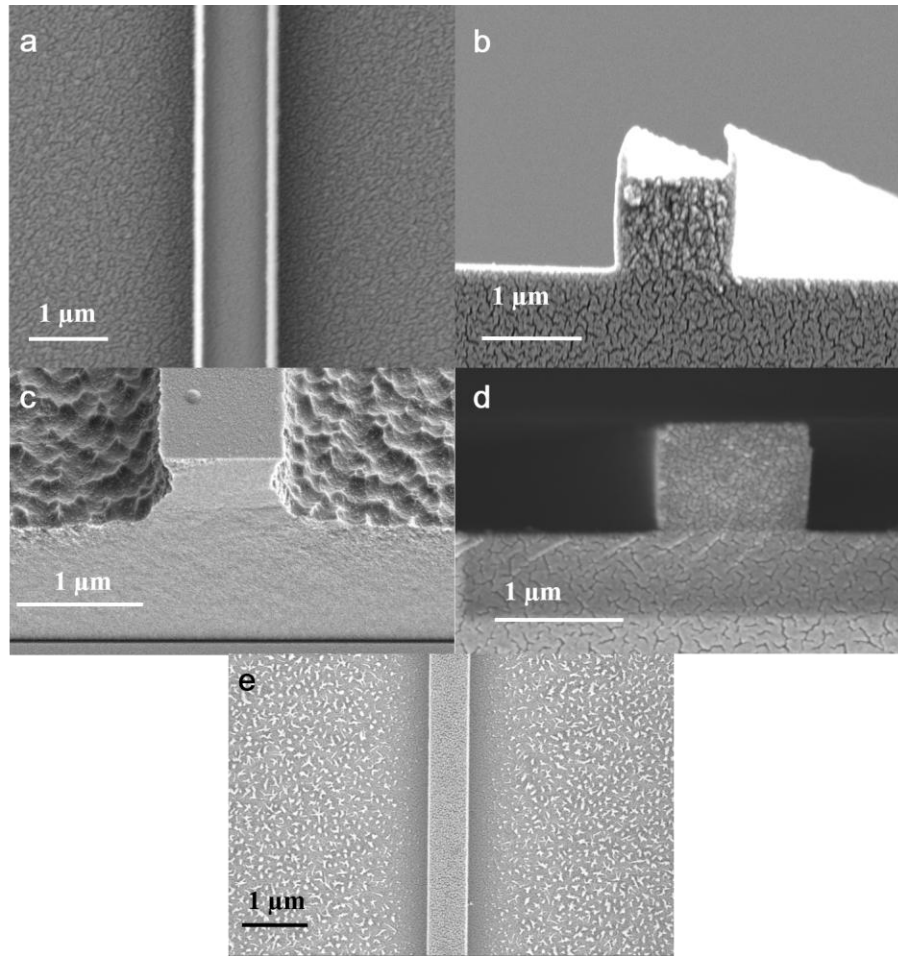


Figure. 2-1. SEM images of: a, b) chlorine-etched GSS waveguides with silicon oxide passivation coating; the grainy surface texture comes from gold coating applied to reduce electrostatic charging during SEM imaging; c) chlorine-etched GSS waveguide without silicon oxide passivation coating; d, e) fluorine-etched GSS waveguides.

To further clarify the role of the silicon oxide coating in defining the etched structure geometry, we performed another set of plasma etching tests after thoroughly cleaning the etching chamber immediately prior to chlorine etching, but otherwise followed identical experimental protocols. Severe undercut was observed in etched waveguides, which is accompanied with significant increase of sidewall roughness as shown in Fig. 2-1c. The

result suggests that the silicon oxide coating which spontaneously forms during the plasma etching step is essential to minimizing radical chemical attack on the GSS pattern sidewalls and maintaining a vertical sidewall profile. This can be envisioned, as silicon oxide is known to be inert in a chlorine plasma.

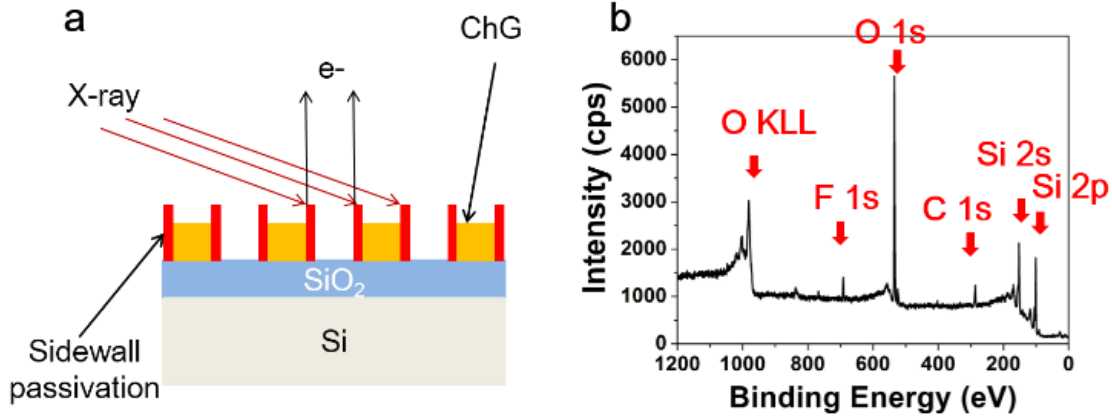


Figure. 2-2. a) Schematic diagram showing the XPS tilted beam analysis configuration. The grating has a 400 nm line width with 800 nm period. b) XPS spectrum showing the presence of Si and O, and trace amounts of C, F in the coating layer.

Figure 2-1d and 2-1e show that fluorine etching similarly generates a nearly vertical sidewall profile. During the fluorine etch, carbon and fluorine radicals generated by the plasma react to form a fluorocarbon polymer passivation layer on the sidewall that prevents lateral etching. The fluorocarbon polymer coating also accounts for the residue observed on the etched surfaces at the two sides of the waveguide (Fig. 2-1d) formed by self-masking [18]. It is interesting to note that the vicinity of the waveguide is free of residues, likely due to shadowing effect. This phenomenon is useful to producing waveguide devices with smooth sidewalls and low optical loss.

2.4 Loss Analysis

Performance of the fabricated devices near 1550 nm wavelength was evaluated using a fiber end fire coupling method on a LUNA Technology laser with built-in Optical Vector Analyzer. To quantitatively assess propagation loss, micro-ring and micro-disk resonators were fabricated by both chlorine and fluorine etching. Optical micrographs of the fabricated resonator samples are shown in Fig. 2-3a and 2-3b. All resonators are 50 μm in radius. Both the micro-ring and the coupling bus waveguides have cross-sectional dimensions of 800 nm \times 450 nm. Fig 2-3c plots a representative transmission spectrum of the micro-ring resonator. The best micro-ring resonator performance is obtained in devices etched by the fluorine chemistry, which yields an intrinsic Q factor of 750,000. The waveguide propagation loss α (in cm^{-1}) is calculated using Eq. 1:

$$\alpha = \frac{2\pi n_g}{Q\lambda_r} \quad (1)$$

where λ_r denotes the resonant wavelength, and n_g represents the group index. The group index is inferred from the Free Spectral Range (FSR) using Eq. 2

$$n_g = \frac{\lambda_r^2}{L \times FSR} \quad (2)$$

to be 2.30, where L is the round trip length of the resonator. Eq. 1 gives a waveguide propagation loss of 0.5 dB/cm. To the best of our knowledge, this value represents the lowest loss figure reported in sub-micron single-mode ChG channel waveguides.

Micro-disk resonators prepared using the same etching protocols yield high quality factors of 10^6 (not shown) for chlorine etched samples and 1.2×10^6 (Fig. 2-3f) for fluorine etched samples, the highest Q-factors in planar ChG optical devices [12, 19-23]. Although both etching chemistries are capable of producing high Q-factors, fluorine etching is preferred over chlorine etching in our case since sidewall passivation using silicon oxide in the case of chlorine etching requires deliberate introduction of trace silica contaminants into the etching chamber, which is far less reproducible compared to fluorocarbon polymer formation during fluorine etching.

To quantify the roughness scattering contribution to optical loss, sidewall roughness of the waveguides was determined from high magnification SEM images using the imaging processing software ImageJ. In the example shown in Fig. 2-4, the waveguide edge profile, represented by a function $f(z)$, was extracted from the image using grayscale analysis. The roughness metrics were subsequently evaluated following procedures described in Ref. [24] and the results were averaged over multiple waveguides. Specifically, the autocorrelation function of the waveguide sidewall roughness is calculated using:

$$R(u) = \langle f(z) \cdot f(z+u) \rangle \quad (3)$$

where the brackets represent ensemble average. The roughness power spectral density (PSD) function is the Fourier transform of $R(u)$. The PSD function is plotted in Fig. 2-4c and a root-mean-square (RMS) roughness of (2.4 ± 0.2) nm for fluorine etched waveguides is obtained from the analysis. Fig. 2-4c further suggests that the roughness distribution does

not comply with either the exponential model or the white noise model. Following the 3-

D

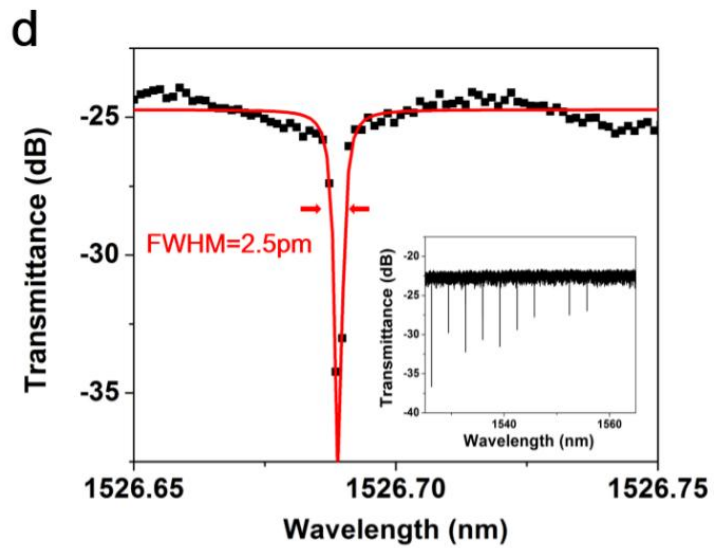
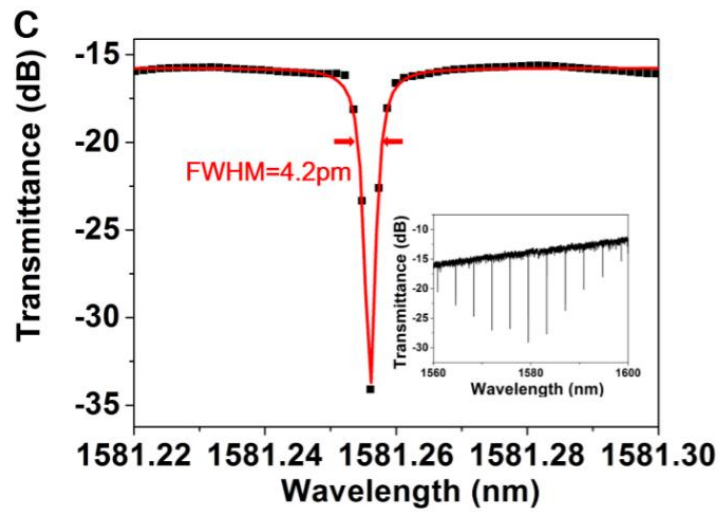
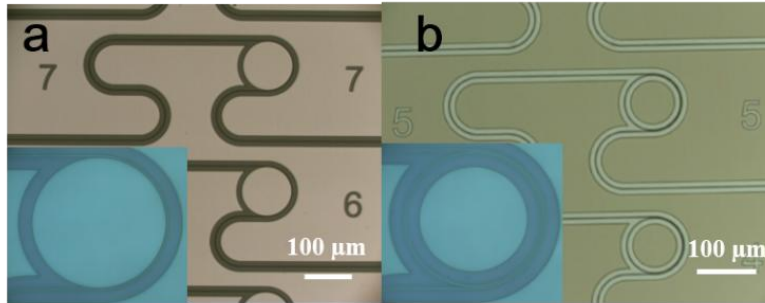


Figure 2-3. Optical microscope images of fabricated a) micro-disk and b) micro-ring resonators. c-d) Transmission spectra of c) micro-ring resonator; and d) micro-disk resonator etched using the fluorine chemistry. The red curves are Lorentzian fit of the spectra.

volume current method in Ref. [24], we estimate that sidewall roughness scattering contributes approximately 0.2 dB/cm optical loss.

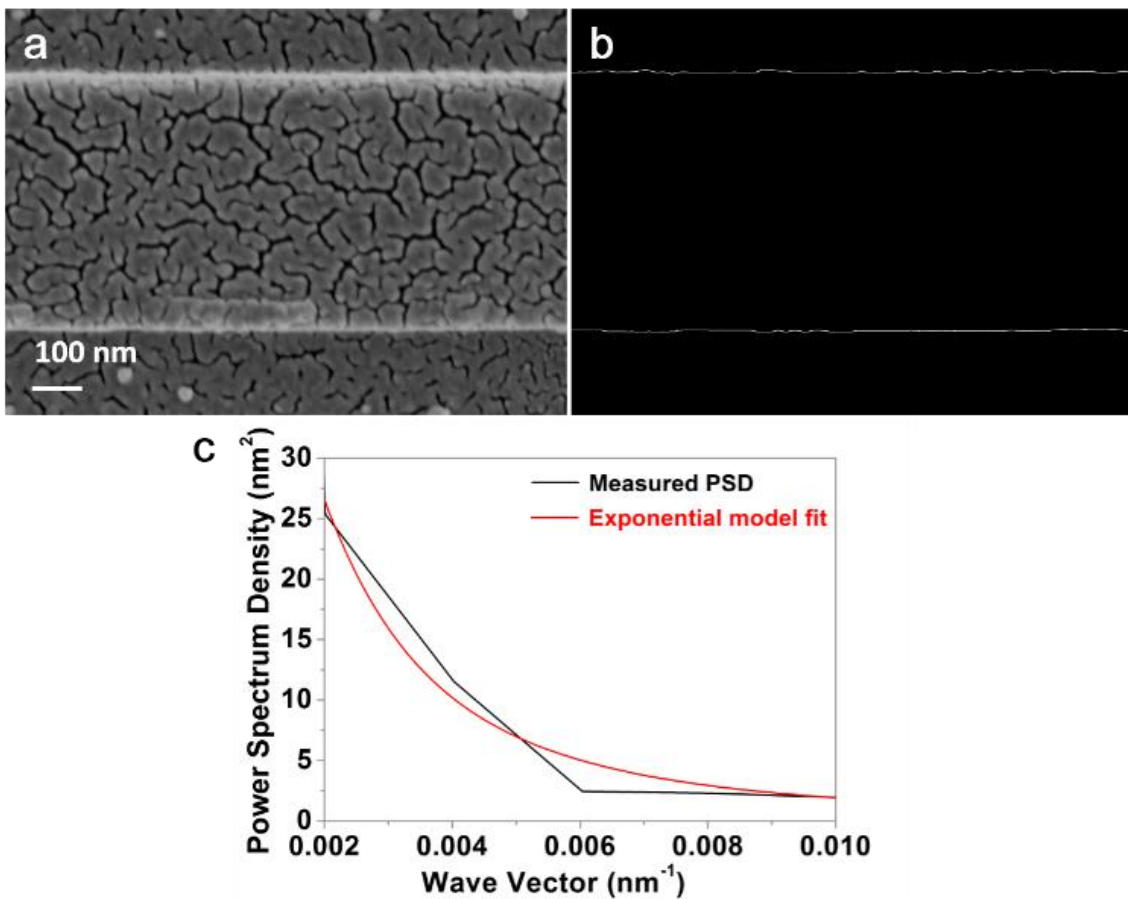


Figure 2-4. Waveguide sidewall roughness analysis example: a) SEM top-view image of a fluorine etched waveguide; the grainy surface texture comes from gold coating applied to reduce electrostatic charging during SEM imaging. b) Waveguide edge extracted from the SEM image. c) PSD function of sidewall roughness (black line). The red line represents exponential model fit.

2.5 Conclusion

In summary, we have demonstrated low-loss GSS photonic device fabrication using electron beam lithography and plasma etching. Optimized chlorine and fluorine etching chemistries are both capable of producing vertical sidewalls and low-loss devices. For fluorine etching, fluorocarbon polymers develop during deposition and provide sidewall passivation, whereas non-intentionally introduced silicon oxide impurities are the primary passivation agent in chlorine etching. A low propagation loss of 0.5 dB/cm and a high Q-factor of 1.2 million were obtained in sub-micron single-mode waveguides and micro-disk resonators patterned using fluorine etching, respectively. These values represent the best low loss performance reported to date in planar chalcogenide glass devices.

Reference

- (1) B. J. Eggleton, B. Luther-Davies, and K. Richardson, *Nat. Photonics* **5**, 141(2011).
- (2) V. Singh, P. T. Lin, N. Patel, H. Lin, L. Li, Y. Zou, F. Deng, C. Ni, J. Hu, and J. Giammarco, *Sci. Technol. Adv. Mater.* **15**, 014603 (2014).
- (3) J. Hu, L. Li, H. Lin, Y. Zou, Q. Du, C. Smith, S. Novak, K. Richardson, and J. D. Musgraves, *Am. Ceram. Soc. Bull.* **94**, 24 (2015).
- (4) L. Li, H. Lin, S. Qiao, Y. Zou, S. Danto, K. Richardson, J. D. Musgraves, N. Lu, and J. Hu, *Nat. Photonics* **8**, 643 (2014).
- (5) M.-L. Anne, J. Keirsse, V. Nazabal, K. Hyodo, S. Inoue, C. Boussard-Pledel, H. Lhermite, J. Charrier, K. Yanakata, and O. Loreal, *Sensors* **9**, 7398 (2009).
- (6) T. V. Galstyan, J. Viens, A. Villeneuve, K. Richardson, and M. Duguay, *J. Lightwave Technol.* **15**, 1343 (1997).
- (7) Y. Ruan, W. Li, R. Jarvis, N. Madsen, A. Rode, and B. Luther-Davies, *Opt. Express* **12**, 5140 (2004).
- (8) T. Han, S. Madden, D. Bulla, and B. Luther-Davies, *Opt. Express* **18**, 19286 (2010).
- (9) Y. Zou, L. Moreel, L. Savelli, H. Lin, J. Zhou, L. Li, S. Danto, J. D. Musgraves, K. Richardson, K. Dobson, R. Birkmire, and J. Hu, *Adv. Opt. Mater.* **2**, 759 (2014).
- (10) J. Hu, N.-N. Feng, N. Carlie, L. Petit, J. Wang, A. Agarwal, K. Richardson, and L. Kimerling, *Opt. Express* **15**, 14566 (2007).
- (11) S. Madden, D.-Y. Choi, D. Bulla, A. V. Rode, B. Luther-Davies, V. G. Ta'eed, M. Pelusi, and B. J. Eggleton, *Opt. Express* **15**, 14414 (2007).
- (12) J. Chiles, M. Malinowski, A. Rao, S. Novak, K. Richardson, and S. Fathpour, *Appl. Phys. Lett.* **106**, 111110 (2015).
- (13) F. Vanier, M. Rochette, N. Godbout, and Y.-A. Peter, *Opt. Lett.* **38**, 4966 (2013).
- (14) R. Wang, A. V. Rode, S. Madden, C. Zha, R. Jarvis, and B. Luther-Davies, *J. Non-Cryst. Solids.* **353**, 950 (2007).
- (15) J. Hu, N.-N. Feng, N. Carlie, L. Petit, A. Agarwal, K. Richardson, and L. Kimerling, *Opt. Express* **18**, 1469 (2010).
- (16) J. Hu, V. Tarasov, A. Agarwal, L. Kimerling, N. Carlie, L. Petit, and K. Richardson, *Opt. Express* **15**, 2307 (2007).
- (17) S. Bouchoule, R. Chanson, A. Pageau, E. Cambril, S. Guilet, A. Rhallabi, and C. Cardinaud, *J. Vac. Sci. Technol., A*, **33**, 05E124 (2015).
- (18) D.-Y. Choi, S. Maden, A. Rode, R. Wang, and B. Luther-Davies, *J. Non-Cryst. Solids.* **354**, 3179 (2008).
- (19) S. Levy, M. Klebanov, and A. Zadok, *Photonics Research* **3**, 63-67 (2015).
- (20) X. Gai, B. Luther-Davies, and T. P. White, *Opt. Express* **20**, 15503 (2012).
- (21) P. Ma, D.-Y. Choi, Y. Yu, Z. Yang, K. Vu, T. Nguyen, A. Mitchell, B. Luther-Davies, and S. Madden, *Opt. Express* **23**, 19969 (2015).
- (22) Y. Zou, D. Zhang, H. Lin, L. Li, L. Moreel, J. Zhou, Q. Du, O. Ogbuu, S. Danto, J. D. Musgraves, K. Richardson, K. Dobson, R. Birkmire, and J. Hu, *Adv. Opt. Mater.* **2**, 478-486 (2014).
- (23) H. Lin, L. Li, Y. Zou, S. Danto, J. D. Musgraves, K. Richardson, S. Kozacik, M. Murakowski, D. Prather, P. Lin, V. Singh, A. Agarwal, L. C. Kimerling, and J. Hu, *Opt. Lett.* **38**, 1470 (2013).
- (24) T. Barwicz, and H. A. Haus, *J. Lightwave Technol.* **23**, 2719 (2005).

Chapter 3

On-Chip Supercontinuum Integrated Chalcogenide Chemical Sensor

3.1 Limitation of Current Photonic Sensor Chips

Infrared (IR) spectroscopy is often considered as a gold standard in analytical chemistry given its ability to unequivocally identify chemical species via “fingerprinting” the molecular vibrational modes. Traditionally, IR spectroscopy relies on benchtop instruments only available in a dedicated laboratory setting. In recent years, integrated photonics has emerged as a promising solution to liberate the technology from the constraint by potentially enabling sensor integration on chip-scale platforms [1-8]. These early demonstrations make use of tunable lasers to perform wavelength interrogation and identify spectral signatures of target molecules. However, the use of tunable lasers, which are bulky instruments involving complex mechanical moving parts, is counterproductive to compact sensing system integration. Moreover, the laser tuning range is bound by gain bandwidth of the lasing medium, which is often merely a small fraction of an octave. Using current or temperature ramping for laser wavelength tuning offers a viable option for miniaturized light sources [9], although the accessible spectral domain using these techniques is small. Consequently, such sensors are limited to the detection of one single species and can be prone to interferences.

3.2 On-Chip Supercontinuum Generation in Chalcogenide Glass

Unlike traditional broadband blackbody sources used in benchtop IR spectrophotometers, waveguide SC sources feature high spatial coherency essential for efficient light coupling and manipulation on a photonic chip. Compared to tunable lasers, SC offers superior bandwidth coverage: for instance, waveguide SC spanning three octaves has been experimentally realized [10]. The broadband nature of SC facilitates access to wavelengths difficult to cover using semiconductor lasers and thereby significantly expands the identifiable molecule repertoire of spectroscopic sensors. In our experiment we use chalcogenide glass (ChG) as the waveguide material for both SC generation and evanescent wave sensing. ChGs are known for its broadband infrared transparency, large Kerr nonlinearity and low two photon absorption (TPA), ideal characteristics for our application [11, 12]. Indeed, ChG waveguides have been separately applied to broadband SC generation [13-17] and IR spectroscopic sensing [18-24]. Here we combine for the first time both functions in a single chip-scale platform, allowing the on-chip photonic sensor to interrogate a broad spectral region from 1.38 μm to 2.05 μm not accessible with a single tunable laser. In addition, unlike previous SC generation experiments in ChGs where bulky pulsed pump lasers were used, we employed a home-built, palm-sized femtosecond laser as the pump source. The laser uses a graphene saturable absorber in an all-fiber system to realize passive mode-locking, and the entire laser can be integrated in a small module of a few centimeters in size [25]. Our work here therefore envisions a standalone, compact spectroscopic sensing system once coupled with miniaturized chip-scale spectrometers we recently developed [26-27].

400 nm thick $\text{Ge}_{22}\text{Sb}_{18}\text{Se}_{60}$ (GeSbSe) films were thermally evaporated onto 4" silicon wafers with 3 μm thermal oxide as an under cladding from GeSbSe glass powders (prepared using melt quenching in a quartz ampoule). Stoichiometry of the film was confirmed by wavelength dispersion X-ray spectroscopy (JEOL-JXA-8200 Superprobe WDS) at 5 different locations on each sample to confirm its compositional uniformity. We choose this glass composition given its large optical nonlinearity (nonlinear index $n_2 = 5.1 \times 10^{-18} \text{ m}^2/\text{W}$) and low TPA (TPA coefficient $\beta = 4.0 \times 10^{-13} \text{ m/W}$), both measured using the Z-scan technique at 1550 nm wavelength. The GeSbSe glass therefore exhibits a nonlinear figure of merit (defined as $n_2/\beta\lambda$, where λ is the wavelength) of 8.3, over one order of magnitude larger than that of silicon at the same wavelength [28]. Refractive index dispersion of the glass film was characterized using Woollam V-VASE32 ellipsometry and plotted in Fig.3-1a. The data were then used to compute the group velocity dispersion (GVD) of the fundamental quasi-TE mode in GeSbSe waveguides with varying widths (Fig. 3-1b). As seen in Fig. 1b, as waveguide width increases from 0.6 to 1.05 μm , the zero-dispersion wavelength progressively shifts towards longer wavelength from 1.35 to 1.68 μm . To efficiently excite SC in a waveguide, the pump wavelength should locate near the zero-dispersion wavelength. Therefore, the optimal GeSbSe waveguide dimensions are 0.95 μm (W) \times 0.4 μm (H) with a zero-dispersion wavelength at 1.56 μm , our pump center wavelength.

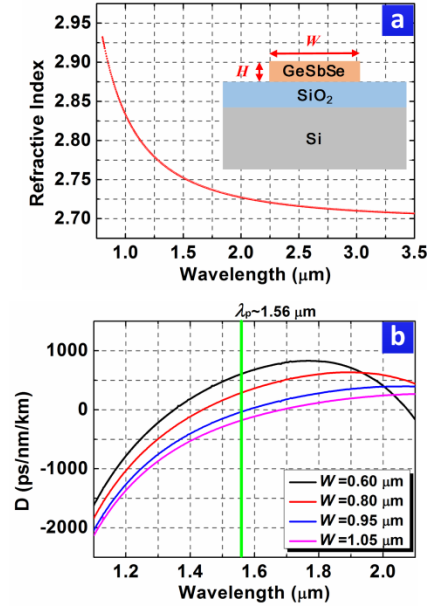


Figure 3-1. (a) Refractive index dispersion of the $Ge_{22}Sb_{18}Se_{60}$ glass film measured using ellipsometry; inset schematically depicts the waveguide structure; (b) Simulated GVD of GeSbSe waveguides with varying widths (W) and a fixed core thickness $H = 400$ nm.

GeSbSe waveguides with varying widths were fabricated using our previously established protocols [29]. In the process, a 350-nm-thick ZEP resist layer was spun onto the substrate followed by exposure on an Elionix ELS-F125 tool at a beam current of 10 nA. The resist pattern was then developed by immersing in ZED-N50 developer for one minute. Reactive ion etching was performed in a PlasmaTherm etcher to transfer the resist pattern to the glass layer. The etching process used a gas mixture of CHF_3 and CF_4 at 3:1 ratio and 5 mTorr total pressure. The incident RF power was fixed at 200 W. Finally, the device was immersed in N-Methyl-2-pyrrolidone (NMP) overnight to remove the ZEP resist and complete device fabrication. The waveguides assume a zigzag geometry with lengths L up to 21 mm (Fig. 3-2a). A cross sectional SEM image of the waveguide is displayed in Fig.

3-2b, showing vertical sidewalls free of etching residue. The waveguides were tested for SC generation using a setup schematically illustrated in Fig. 3-2c. The pump source is a home-built, palm-sized femtosecond laser module (Fig. 3-2d) with a center wavelength of 1560 nm, a repetition rate of 8.1 MHz, and a pulse duration of 800 fs [25]. The laser is assembled on an all-fiber platform and passively mode-locked using a graphene saturable absorber synthesized in-house [30]. The femtosecond seed laser was then amplified by a homemade erbium-doped fiber amplifier (EDFA) to boost the average power from 0.2 mW to a maximum of 5.5 mW, producing a peak power of approximately 0.8 kW after amplification. The fibers used in our experiment can be easily spooled to a centimeter-scale radius with negligible bending loss. Therefore, the all-fiber construction of the laser and amplifier potentially allows the light source module to be further down scaled to an ultra-compact package of a few centimeters in size. The TE-polarized, amplified pulses were coupled into and out of the GeSbSe waveguide devices via taper lensed fibers with a coupling loss of approximately 7 dB per facet. An optical spectrum analyzer (OSA, Yokogawa AQ6375B covering 1.2 – 2.4 μm wavelength range) was used to spectrally resolve output light from the chip. By replacing the OSA with an on-chip spectrometer (for example, the digital Fourier Transform spectrometer we recently developed [8]), we may realize a compact handheld sensing system.

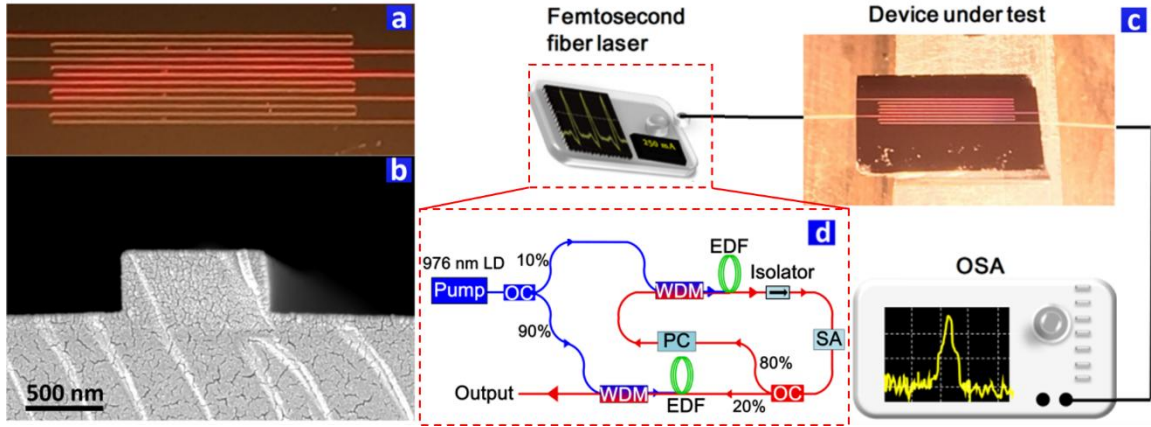


Figure 3-2. (a) Top-view optical micrograph of the zigzag GeSbSe waveguides; (b) SEM cross-sectional image of a $0.95 \mu\text{m}$ (W) \times $0.4 \mu\text{m}$ (H) GeSbSe waveguide; (c) The experimental setup of on-chip SC generation and sensing; (d) Block diagram of home-built femtosecond laser module (OC: Optical coupler, WDM: wavelength division multiplexer, SA: graphene saturable absorber, PC: polarization controller)

Next we investigated the influence of waveguide geometry, waveguide length, and pump power on the SC spectra to elucidate the SC generation mechanism and understand sensor device design trade-offs. Figure 3-3a presents the SC spectra in GeSbSe waveguides of different widths. All the waveguides have the same core thickness of $0.4 \mu\text{m}$ and a uniform length of 21 mm. SC generated by the waveguide with $0.95 \mu\text{m}$ width, whose zero-dispersion point aligns with the pump wavelength, exhibits the maximum bandwidth consistent with our GVD simulations. For waveguides with widths $W = 0.6 \mu\text{m}$ and $0.8 \mu\text{m}$, the pump wavelength is largely away from their zero-dispersion wavelengths. In this regime, SC is formed through initial self-phase modulation followed by self-steepening and other high-order nonlinear effects contributing to spectral broadening. In contrast, for waveguides with $W = 0.95 \mu\text{m}$ and $1.05 \mu\text{m}$, the pump wavelength locates near the zero-

dispersion point. In this case, a broad SC spectrum results from soliton fission, self-frequency shift and dispersive wave emission. To further validate the SC generation mechanism, we compute the nonlinear length ($L_{NL} = 1/P_0\gamma$, where P_0 and γ denote the pump peak power and waveguide nonlinear parameter, respectively) to be 0.29 mm, which is almost one order of magnitude smaller than the waveguide length. Therefore, we conclude that the SC generation mechanism in our device is dominated by high-order soliton fission from various kinds of nonlinear optical effects.

Figure 3-3b plots the SC spectra in GeSbSe waveguides with the different lengths and the optimal dimensions ($W = 0.95 \text{ }\mu\text{m}$, $H = 0.4 \text{ }\mu\text{m}$). As indicated in the figure, the SC bandwidth extends to over half an octave albeit with decreased total output power when the waveguide length increases to 21 mm. This power attenuation is attributed to the GeSbSe waveguide propagation loss, measured using the cut-back method to be $\sim 4 \text{ dB/cm}$. This trade-off between SC spectral coverage and power can be mitigated with reduced waveguide losses.

SC spectra from the 21-mm-long waveguide ($W = 0.95 \text{ }\mu\text{m}$, $H = 0.4 \text{ }\mu\text{m}$) are shown in Figure 3-3c for several pump power levels. Clearly, higher pump power produces SC with an increased bandwidth. The maximum SC spectral span we obtained in our experiment is 1380 nm to 2050 nm (gauged at 20-dB flatness), primarily limited by the optical power available from our compact pump source. If desired, higher pump power and hence even

wider SC spectral coverage can be obtained by adding more amplification stages albeit at the expense of the compactness of the system.

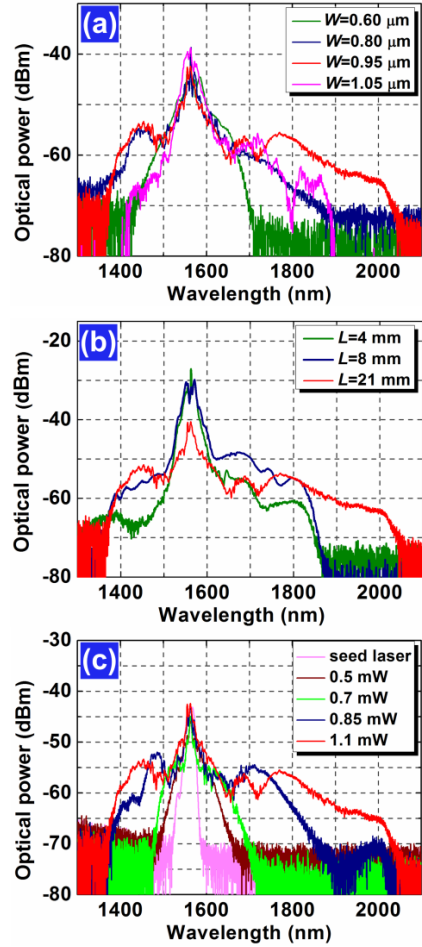


Figure 3-3 SC spectra in GeSbSe waveguides: (a) SC spectra from waveguides with different widths W ; when $W = 0.95 \mu\text{m}$, the zero-dispersion point of the waveguide coincides with the pump wavelength; (b) SC generation of GeSbSe waveguides with the optimal geometry ($W = 0.95 \mu\text{m}$, $H = 0.4 \mu\text{m}$) and varying lengths; (c) SC spectra from a 21-mm-long GeSbSe waveguide ($W = 0.95 \mu\text{m}$, $H = 0.4 \mu\text{m}$) at different pump power levels. The power quoted here represent the average optical power coupled into the waveguide.

3.3 Demonstration of Chloroform Sensing

In the sensing experiment, the GeSbSe waveguide was immersed in carbon tetrachloride (CCl_4) solutions containing varying concentrations of chloroform (CHCl_3). It is worth noting that even though most IR sensing relies on Mid-IR absorption spectrum where the chemical bond vibrational fundamental modes are active, their overtones are still able to present significant amount of absorption in the Near-IR. To increase the vibrational frequency of the C-H covalent bond, a more electron negative C is preferred to make the bond stiffer. This can be realized by connect C to other electron withdrawing group. Chloroform stands out as it has three -Cl to withdraw the electrons from the C. The CCl_4 solvent is optically transparent across the near-IR [19], whereas the C-H bond in chloroform leads to an overtone absorption peak centering at 1695 nm, a wavelength outside the standard telecommunication bands. Here we use the C-H overtone absorption to quantify the sensing performance of our device. SC spectra near the chloroform absorption peak obtained with GeSbSe waveguides of different lengths or solutions of different concentrations are presented in Figs. 3-4a and 3-4b, respectively. The data were normalized to the background (collected in pure CCl_4) and the raw spectra are furnished in the inset. Figure 3-4c plot the absorption at 1695 nm versus waveguide length, indicating that the classical Lambert's law is obeyed in the new SC-enabled sensing mechanism. The optical absorption coefficient α (in dB/cm) of chloroform at 1695 nm was also quantified using a benchtop UV-Vis spectrophotometer, which is used to project the absorption A (in dB) measured from the waveguide sensor (marked with a triangle in Fig. 3-4a) following:

$$A = \Gamma\alpha L$$

Here Γ denotes the waveguide modal confinement factor in the solution, which is 6.8% computed using a finite difference mode solver (shown in Fig. 3-4c inset). The agreement between the two techniques suggests that the waveguide sensor can be applied to quantitative analysis of absorption coefficients in chemical samples.

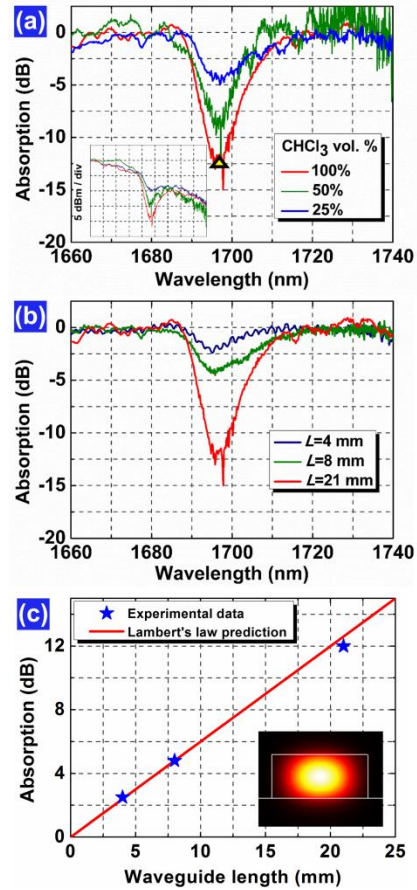


Figure 3-4. (a) SC spectra measured on GeSbSe waveguides of different lengths L when immersed in chloroform; the triangle marks the optical absorption at 1695 nm calibrated using a benchtop UV-Vis spectrometer for an equivalent waveguide path length $L = 21$ mm; (b) SC spectra taken on a 21-mm-long GeSbSe waveguide immersed in $\text{CHCl}_3\text{-CCl}_4$ solutions of varying volume concentration ratios; (c) measured peak absorption at 1695 nm versus the GeSbSe waveguide length used in the experiment: the linear relation indicates that the classical Lambert's law is obeyed; inset shows the mode profile simulated by finite difference method.

3.4 Conclusion

In conclusion, we demonstrated in this work an on-chip spectroscopic sensor where a chalcogenide glass waveguide serves as both the broadband SC light source and the evanescent sensing element. By incorporating highly nonlinear GeSbSe glass in a dispersion engineered waveguide design, SC spanning over half of an octave was achieved using a compact femtosecond laser pumping source. We validated the sensing performance of the device through quantifying the C-H bond overtone absorption of chloroform at 1695 nm wavelength. This prototype envisages a handheld spectroscopic sensing platform with broadband interrogation capability suitable for field-deployed applications.

Reference

- (1) Nitkowski, A.; Chen, L.; Lipson, M., Cavity-enhanced on-chip absorption spectroscopy using microring resonators. *Opt. Express* **2008**, *16*, 11930-11936;
- (2) Nitkowski, A.; Baeumner, A.; Lipson, M., On-chip spectrophotometry for bioanalysis using microring resonators. *Biomed. Opt. Express* **2011**, *2*, 271-277;
- (3) Mizaikoff, B., Waveguide-enhanced mid-infrared chem/bio sensors. *Chem. Soc. Rev.* **2013**, *42*, 8683-8699;
- (4) Wang, X.; Antoszewski, J.; Putrino, G.; Lei, W.; Faraone, L.; Mizaikoff, B., Mercury-cadmium-telluride waveguides—a novel strategy for on-chip mid-infrared sensors. *Analytical Chemistry* **2013**, *85*, 10648-10652;
- (5) Ryckeboer, E.; Bockstaele, R.; Vanslembrouck, M.; Baets, R., Glucose sensing by waveguide-based absorption spectroscopy on a silicon chip. *Biomed. Opt. Express* **2014**, *5*, 1636-1648;
- (6) Chen, Y.; Lin, H.; Hu, J.; Li, M., Heterogeneously integrated silicon photonics for the mid-infrared and spectroscopic sensing. *ACS Nano* **2014**, *8*, 6955-6961;
- (7) Singh, V.; Lin, P. T.; Patel, N.; Lin, H.; Li, L.; Zou, Y.; Deng, F.; Ni, C.; Hu, J.; Giammarco, J., Mid-infrared materials and devices on a Si platform for optical sensing. *Sci. Technol. Adv. Mat.* **2014**, *15*, 014603;
- (8) Smith, C. J.; Shankar, R.; Laderer, M.; Frish, M. B.; Loncar, M.; Allen, M. G., Sensing nitrous oxide with QCL-coupled silicon-on-sapphire ring resonators. *Opt. Express* **2015**, *23*, 5491-5499.
- (9) Tombez, L.; Zhang, E.; Orcutt, J.; Kamlapurkar, S.; Green, W., Methane absorption spectroscopy on a silicon photonic chip. *Optica* **2017**, *4*, 1322-1325.
- (10) Hickstein, D. D.; Jung, H.; Carlson, D. R.; Lind, A.; Coddington, I.; Srinivasan, K.; Ycas, G. G.; Cole, D. C.; Kowligy, A.; Fredrick, C.; Droste, S.; Lamb, E. S.; Newbury, N. R.; Tang, H. X.; Diddams, S. A.; Papp, S. B., Ultrabroadband Supercontinuum Generation and Frequency-Comb Stabilization Using On-Chip Waveguides with Both Cubic and Quadratic Nonlinearities. *Phys. Rev. Appl.* **2017**, *8*, 014025.
- (11) Eggleton, B. J.; Luther-Davies, B.; Richardson, K., Chalcogenide photonics. *Nat. Photon.* **2011**, *5*, 141-148;
- (12) Carlie, N.; Musgraves, J. D.; Zdyrko, B.; Luzinov, I.; Hu, J.; Singh, V.; Agarwal, A.; Kimerling, L. C.; Canciamilla, A.; Morichetti, F., Integrated chalcogenide waveguide resonators for mid-IR sensing: leveraging material properties to meet fabrication challenges. *Opt. Express* **2010**, *18*, 26728-26743.
- (13) Yu, Y.; Gai, X.; Ma, P.; Vu, K.; Yang, Z.; Wang, R.; Choi, D.-Y.; Madden, S.; Luther-Davies, B., Experimental demonstration of linearly polarized 2–10 μm supercontinuum generation in a chalcogenide rib waveguide. *Opt. Lett.* **2016**, *41*, 958-961;
- (14) Yu, Y.; Gai, X.; Ma, P.; Choi, D.-Y.; Yang, Z.; Wang, R.; Debbarma, S.; Madden, S. J.; Luther-Davies, B., A broadband, quasi-continuous, mid-infrared supercontinuum generated in a chalcogenide glass waveguide. *Laser Photon. Rev.* **2014**, *8*, 792-798;
- (15) Lamont, M. R.; Luther-Davies, B.; Choi, D.-Y.; Madden, S.; Eggleton, B. J., Supercontinuum generation in dispersion engineered highly nonlinear ($\gamma=10/\text{W/m}$) As_2S_3 chalcogenide planar waveguide. *Opt. Express* **2008**, *16*, 14938-14944;
- (16) Gai, X.; Choi, D.-Y.; Madden, S.; Yang, Z.; Wang, R.; Luther-Davies, B., Supercontinuum generation in the mid-infrared from a dispersion-engineered As_2S_3 glass rib waveguide. *Opt. Lett.* **2012**, *37*, 3870-3872;

- (17) Tremblay, J.-E.; Lin, Y.-H.; Hsu, P.-K.; Malinowski, M.; Novak, S.; Qiao, P.; Camacho-Gonzalez, G. F.; Chang-Hasnain, C. J.; Richardson, K.; Fathpour, S.; Wu, M. C. In Large Bandwidth Silicon Nitride Spot-Size Converter for Efficient Supercontinuum Coupling to Chalcogenide Waveguide, *Conference on Lasers and Electro-Optics, San Jose, California*, **2017**; p SF1J.7.
- (18) Ganjoo, A.; Jain, H.; Yu, C.; Song, R.; Ryan, J. V.; Irudayaraj, J.; Ding, Y. J.; Pantano, C. G., Planar chalcogenide glass waveguides for IR evanescent wave sensors. *J. Non-Cryst. Solids* **2006**, *352*, 584-588;
- (19) Hu, J.; Tarasov, V.; Agarwal, A.; Kimerling, L.; Carlie, N.; Petit, L.; Richardson, K., Fabrication and testing of planar chalcogenide waveguide integrated microfluidic sensor. *Opt. Express* **2007**, *15*, 2307-2314;
- (20) Hu, J.; Carlie, N.; Petit, L.; Agarwal, A.; Richardson, K.; Kimerling, L. C., Cavity-enhanced IR absorption in planar chalcogenide glass microdisk resonators: experiment and analysis. *J. Lightwave Technol.* **2009**, *27*, 5240-5245;
- (21) Richardson, K.; Petit, L.; Carlie, N.; Zdyrko, B.; Luzinov, I.; Hu, J.; Agarwal, A.; Kimerling, L.; Anderson, T.; Richardson, M., Progress on the fabrication of on-chip, integrated chalcogenide glass (ChG)-based sensors. *J Nonlinear Opt. Phys.* **2010**, *19*, 75-99;
- (22) Charrier, J.; Brandily, M.-L.; Lhermite, H.; Michel, K.; Bureau, B.; Verger, F.; Nazabal, V., Evanescent wave optical micro-sensor based on chalcogenide glass. *Sensors and Actuators B: Chemical* **2012**, *173*, 468-476;
- (23) Ma, P.; Choi, D.-Y.; Yu, Y.; Gai, X.; Yang, Z.; Debbarma, S.; Madden, S.; Luther-Davies, B., Low-loss chalcogenide waveguides for chemical sensing in the mid-infrared. *Opt. Express* **2013**, *21*, 29927-29937;
- (24) Han, Z.; Lin, P.; Singh, V.; Kimerling, L.; Hu, J.; Richardson, K.; Agarwal, A.; Tan, D., On-chip mid-infrared gas detection using chalcogenide glass waveguide. *Appl. Phys. Lett.* **2016**, *108*, 141106.
- (25) Xu, H.; Wan, X.; Ruan, Q.; Yang, R.; Du, T.; Chen, N.; Cai, Z.; Luo, Z., Effects of Nanomaterial Saturable Absorption on Passively Mode-Locked Fiber Lasers in Anomalous Dispersion Regime: Simulations and Experiments. *IEEE J. Sel. Top. Quantum Electron.* **2018**, *24*, 1100209.
- (26) Kita, D.; Lin, H.; Agarwal, A.; Richardson, K.; Luzinov, I.; Gu, T.; Hu, J., On-chip infrared spectroscopic sensing: redefining the benefits of scaling. *IEEE J. Sel. Top. Quantum Electron.* **2017**, *23*, 5900110;
- (27) Lin, H.; Luo, Z.; Gu, T.; Kimerling Lionel, C.; Wada, K.; Agarwal, A.; Hu, J., Mid-infrared integrated photonics on silicon: a perspective. *Nanophotonics* **2017**.
- (28) Ta'eed, V. G.; Baker, N. J.; Fu, L.; Finsterbusch, K.; Lamont, M. R.; Moss, D. J.; Nguyen, H. C.; Eggleton, B. J.; Choi, D. Y.; Madden, S., Ultrafast all-optical chalcogenide glass photonic circuits. *Opt. Express* **2007**, *15*, 9205-9221.
- (29) Du, Q.; Huang, Y.; Li, J.; Kita, D.; Michon, J.; Lin, H.; Li, L.; Novak, S.; Richardson, K.; Zhang, W., Low-loss photonic device in Ge-Sb-S chalcogenide glass. *Opt. Lett.* **2016**, *41*, 3090-3093.
- (30) Luo, Z.; Zhou, M.; Weng, J.; Huang, G.; Xu, H.; Ye, C.; Cai, Z., Graphene-based passively Q-switched dual-wavelength erbium-doped fiber laser. *Opt. Lett.* **2010**, *35*, 3709-3711

Chapter 4. Monolithically Integration of On-chip Magneto-optical Isolators

4.1 Magneto-optical (MO) Effect

A time varying electric and magnetic field in a propagating light wave can be denoted by an inherent property called polarization. The polarization of the light is defined as the direction where its electric field component oscillates. When describing a free space light, a linearly polarization is usually used to show the electric field is either vertical or horizontal, but in light- matter interactions, the two counterpart in circular polarization are the preferred representation. In general, there are two sense of circular polarization, left hand circular polarization (LHCP) and right hand circular polarization (RHCP). The importance of expressing the polarization in circular polarization way emerges when the light is propagate in magnetized media where the magnetization is parallel with light propagation direction. In this case, the two mode of polarization are propagating at different velocity, creating a magnetic circular birefringence (MCB). The overall effect of MCB on a linearly polarized light will rotate the polarization of the light when it transmit from the magnetic material and this phenomena is named Faraday rotation. If the Faraday rotator can achieve 45 degrees rotation of its polarization, then the reflected light will gain a total rotation of 90 degrees, becoming its orthogonal mode in polarization. This idea illustrate how an isolator work by a 45 degrees Faraday rotator.

The origin of MCB comes from the difference in the permeability and permittivity tensor between the two circularly polarization. Mathematically, the product of these two tensors can be expressed as below when all the moments are aligned in the z direction:

$$[\boldsymbol{\varepsilon}] \cdot [\boldsymbol{\mu}] = \begin{pmatrix} \varepsilon_0 & -i\varepsilon_1 & 0 \\ +i\varepsilon_1 & \varepsilon_0 & 0 \\ 0 & 0 & \varepsilon_z \end{pmatrix} \cdot \begin{pmatrix} \mu & -i\kappa & 0 \\ +i\kappa & \mu & 0 \\ 0 & 0 & \mu_z \end{pmatrix} \quad (1)$$

where ε_0 and μ expressed the diagonal components while ε_1 and κ denotes the off diagonal ones. The eigensolutions of this matrix are the mode of LHCP (-) and RHCP (+), respectively. That means, $\varepsilon_{\pm}\mu_{\pm} = (\varepsilon_0\mu + \varepsilon_1\kappa) \pm (\varepsilon_0\kappa + \varepsilon_1\mu)$, where ε_z is neglected. It worth noting that if there are no off diagonal element in one of these two tensor, MCB also vanishes. The above expression then gives $\beta_{\pm} = \frac{\omega}{c} \sqrt{(\varepsilon_0\mu + \varepsilon_1\kappa) \pm (\varepsilon_0\kappa + \varepsilon_1\mu)}$, from which we can define a Verdet constant as the rotation angel of a linearly polarized light when passing through a unit length:

$$\theta_F = \frac{\beta_+ - \beta_-}{2} \quad (2)$$

In on-chip photonics configuration, a similar MO effect non-reciprocal phase shift (NRPS) plays a more important role as Faraday rotation in photonic waveguides is hindered by birefringence. Unlike Faraday rotation, NRPS is implemented with magnetization perpendicular to the light propagation direction and is insensitive to birefringence. Magnetic field lifts the degeneracy between forward and backward propagating quasi-TM modes by inducing an effective index difference Δn_{eff} .

$$\Delta\beta(TM) = \frac{2\beta^{TM}}{\omega\varepsilon_0 N} \iint \frac{\Theta_F}{n_0^4} H_y \partial_x H_y dx dy \quad (3)$$

where n_{eff} is the modal effective index, ε_0 is the vacuum wavelength, N the time-averaged modal power flux, n_0 represents the MO oxide refractive index, Θ_F is the Faraday rotation, and the integration is performed over the MO oxide cross-section. And If the magnetic field is applied along the out of plane direction, similarly the quasi-transverse electric (quasi-TE) modes will exhibit NRPS can be calculated below:

$$\Delta\beta(TE) = \frac{2\omega\varepsilon_0}{\beta^{TE} N} \iint \Theta_F E_y \partial_y E_y dx dy \quad (4)$$

4.2 Introduction to isolator

Isolators, as the photonics counterpart of electrical diodes, play a critical role in photonic integrated circuits (PICs) by preventing harmful feedback between different parts of the circuit [1]. For example, an isolator is often used to protect a laser source from destabilizing feedback or damage from back-reflected light. The need for on-chip isolation becomes imperative as the level of photonic integration continues to scale, since unwanted reflections between the many integrated devices in a PIC are common and can be highly disruptive in a complex optical network.

Fundamentally, optical isolation requires breaking the time-reversal symmetry of light propagation. including magneto-optical (MO) effects [2-24], optical nonlinearity [25-29], dynamic modulation [30-33], and optomechanical interactions [34]. Among these

approaches, magneto-optical isolation benefits from its fully passive operation, simple device architectures, as well as large dynamic range, and therefore it has been the incumbent solution adopted in current bulk optical systems. Traditional optical isolators used in free-space and fiber-optic systems are almost exclusively based on Faraday rotation in MO crystals, in which a magnetic field is applied along the light propagation direction to induce circular birefringence and polarization rotation. These Faraday rotation isolators typically feature an isolation ratio of the order of 30 to 40 dB, an insertion loss below 1 dB, and an operation bandwidth exceeding 50 nm in the near-infrared (IR) telecommunication window around 1.5- μm wavelength. Despite the high performance of these free-space isolators, they are bulky discrete devices not suitable for planar on-chip integration. In addition, at present, the price of a discrete isolator ranges anywhere from USD\$30 up to more than USD\$1000, a prohibitive cost for large-scale PICs.

On-chip magneto-optical isolation can be achieved by Faraday rotation, [10, 11] nonreciprocal phase shift (NRPS), [2-9] and nonreciprocal mode conversion. [22] The Faraday rotator configuration used in free-space isolators is sensitive to waveguide birefringence and is not suitable for on-chip optical isolation, unless a quasi-phase match scheme is implemented (Figure 4-1b). [10, 11] Schemes based on nonreciprocal optical loss in an InGaAsP waveguide coated with iron [23] and active devices, including an amplifier to compensate for the loss, [15] have been demonstrated. Nonreciprocal mode conversion, [35] cutoff, [36, 37] resonant delocalization, [38] and coupling [39, 40] have also been theoretically explored, although experimental realization of on-chip optical isolators and circulators based on these mechanisms has not yet been reported.

Unlike Faraday rotation, NRPS is implemented with magnetization perpendicular to the light propagation direction and is insensitive to birefringence. [2] In a typical NRPS device configuration, an applied magnetic field perpendicular to light propagation direction biases the MO material and lifts the degeneracy between forward and backward propagating waveguide modes by inducing an effective index difference. The directional dependence of waveguide mode effective index can be leveraged to realize asymmetric light transmission in various device platforms, including Mach–Zehnder interferometers (MZIs), [41-43] microring resonators, [44, 45] multimode interferometers, [46, 47] and photonic crystals. [48] Examples of resonator, photonic crystal and interferometer devices are given in Figures 4-1a, c and d. These device configurations suffer from limitations such as the large footprint of interferometers and the low bandwidth and high sensitivity to environment of resonators.

Development of on-chip isolators has been hampered by the incompatibility of traditional MO materials with monolithic integration on semiconductor substrate platforms. Unlike doped-glass-based fiber-optic isolators, the very limited real estate on a chip requires the use of materials with high Verdet constants (i.e., large Faraday rotation) in on-chip isolators. These materials, typically single-crystalline bismuth or cerium doped yttrium iron garnet (Bi:YIG, $\text{Bi}_x\text{Y}_{3-x}\text{Fe}_5\text{O}_{12}$ and Ce:YIG, $\text{Ce}_x\text{Y}_{3-x}\text{Fe}_5\text{O}_{12}$), have attractive figures of merit (FOMs) in the near IR, but cannot be monolithically grown on common semiconductor substrates (Si or InP) due to large lattice and thermal expansion mismatch. [49]

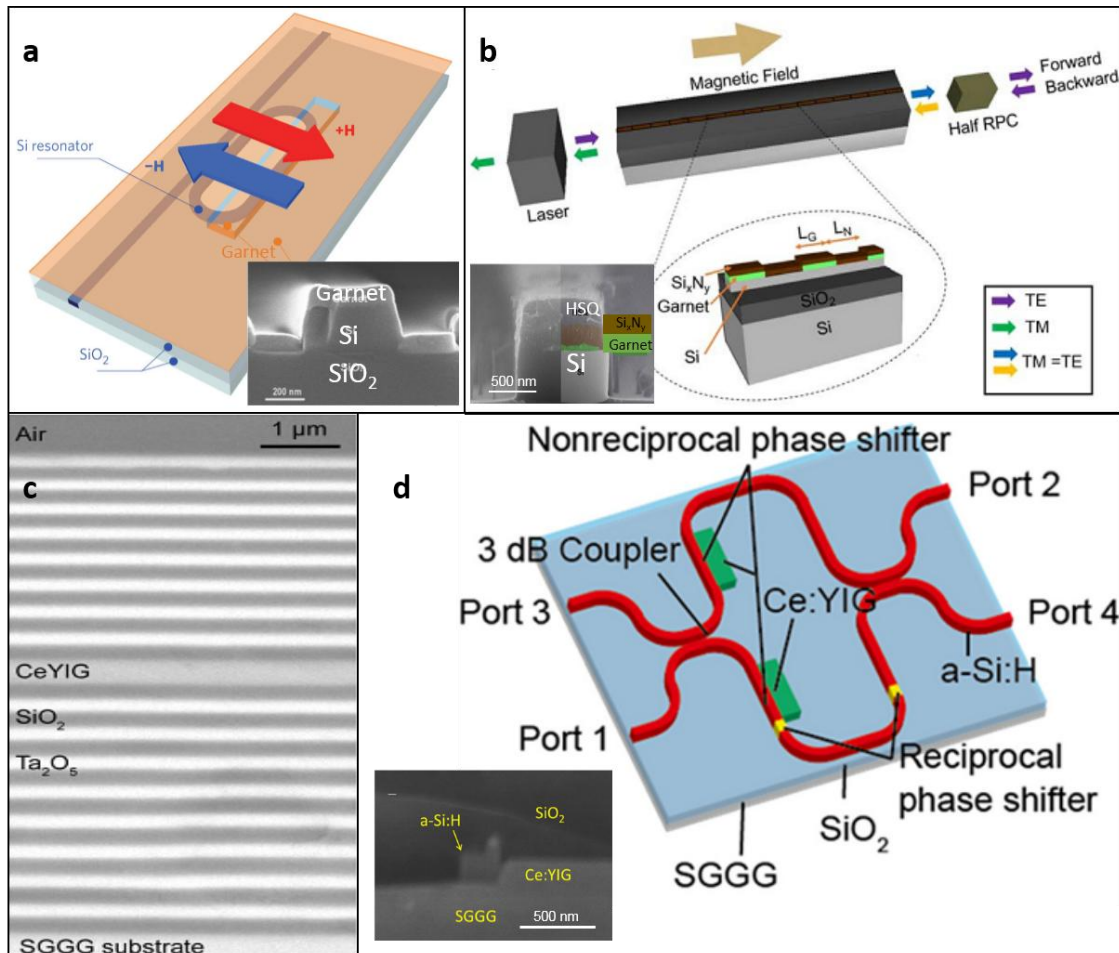


Figure 4-1. (a) Schematic of a nonreciprocal optical resonator structure and cross-section (inset) through the garnet-clad section of the Si waveguide.[40] (b) Schematic showing a Faraday rotation waveguide isolator and cross-section (inset) of the garnet-clad waveguide. Adapted with permission from Reference 6. © 2017 Nature Publishing Group. (c) Cross-sectional image of a fabricated one-dimensional magneto-photonic crystal consisting of magneto-optical garnet (Ce:YIG, cerium-doped yttrium iron garnet) between two Bragg mirrors. [54] (d) Schematic and cross-section (inset) of a Mach-Zehnder transverse electric (TE) mode isolator with Ce:YIG mesas adjacent to the sidewalls of the waveguide. Note: a-Si:H, hydrogenated amorphous silicon. Adapted with permission from Reference 58.© 2017 The Optical Society.

Two routes have been pursued to resolve the integration challenge—the hybrid approach, which relies on wafer bonding of garnet crystals, [12-19] and the monolithic approach, which directly deposits polycrystalline ferromagnetic oxides or doped semiconductors or polymers [6-11] on substrates. The former approach can leverage the large Verdet constant and low material absorption in single-crystalline garnets to achieve good isolation performance; however, the wafer-bonding process required by this approach is expensive and limits fabrication throughput and yield.

Deposited polycrystalline ferromagnetic oxides, on the other hand, offer a promising path toward monolithic integration of optical isolators directly on semiconductor substrates with improved fabrication throughput and yield. One limitation with this approach is the inferior optical performance of these polycrystalline thin films, which so far exhibit lower Faraday rotation and higher optical absorption compared to their single-crystalline counterparts. The isolator performance is ultimately bounded by the material characteristics, and more specifically, the material magneto-optical FOM defined as the ratio of Faraday rotation to optical loss (in units of degrees of rotation per dB loss). Therefore, improving the FOM of MO films is a critical research objective. In addition to enhancing material quality, further reducing the film growth and heat-treatment temperatures to ensure compatibility of the material deposition process with standard complementary metal oxide semiconductor (CMOS) back-end fabrication constitutes another important research thrust.

4.3 Magnetic Garnet

The basis of choose an ideal magnetic material is based on two criteria: high Verdet constant and low propagation loss in telecommunication wavelength [9].. Magnetic garnet can be grown in bulk, but recently, high quality single crystal film can also be achieved by using the gadolinium gallium garnet (GGG) substrate. Methods of liquid phase epitaxy [11], sputtering [12] and pulsed laser deposition [13] has been reported. However, grown of magnetic garnet film onto silicon is still a challenging topic. Substitution of Y ion with Bi and Ce can dramatically increase the Faraday rotation [14]. With increasing substitution concentration, the rotation angle increase, while the optical loss also increases. Thus an optimum Ce concentration can be expected by combining the overall effect.

The growth of high FOM garnets such as Bi:YIG and Ce:YIG requires processes that promote growth of the garnet phase over competing phases such as CeO_2 or Bi_2O_3 , particularly on non-garnet substrates where there is no epitaxial stabilization of a garnet phase. Iron garnet phases have been grown directly on substrates such as silica, and use of seed layers of YIG combined with rapid thermal annealing (RTA) has been shown to promote the growth of MO garnets. Figure 4-2 shows examples of structural characterization, magnetic hysteresis, Faraday rotation, and FOM of MO garnet films on various substrates.

Garnet films have been used in demonstrations of integrated nonreciprocal photonic devices such as isolators and modulators. [4-9] Bi et al. [4] demonstrated the first

monolithically integrated optical isolator on a silicon-on-insulator (SOI) platform (Figure 4-2a) in which the MO garnet was deposited by PLD on a single-mode silicon racetrack resonator through a window in the SiO₂ cladding layer. A 20-nm-thick YIG seed layer was deposited and crystallized by RTA, and then 80-nm Ce:YIG (composition Ce₁Y₂Fe₅O₁₂) was grown. The YIG layer stabilizes the Ce:YIG, and the use of RTA to crystallize the YIG seed layer significantly reduces the overall thermal budget for the garnet film stack. This is beneficial to reduce cracking in the garnet films and to prevent degradation of other parts of the photonic circuit. [50, 51] Films grown using this method exhibited high MO activity with Faraday rotation up to ~3000 degrees/cm at 1550-nm wavelength (Figure 4-2d), compared to single-crystal values of 3300 degrees/cm [53] to 5500 degrees/cm, [52] and bulk-like saturation magnetization (Figure 4-2c).

Seed layers have also been applied in forming sputtered polycrystalline Ce:YIG films. [53, 54] The seed-layer process can be applied to various substrates, including silica and quartz, although oxidation of a silicon nitride-coated substrate was observed during PLD garnet growth. [55] A simplified PLD process was introduced by Sun et al. [8] who placed the YIG seed layer on top of the MO garnet, then crystallized both at the same time by RTA. The film structure resulting from this process is shown in Figure 4-2a, e. This process gives direct contact between the MO garnet and the waveguide, which maximizes the coupling of light from the waveguide to the MO cladding. This avoids the reduction in net Faraday rotation caused by the opposite sign of FR in YIG versus Bi:YIG and Ce:YIG.

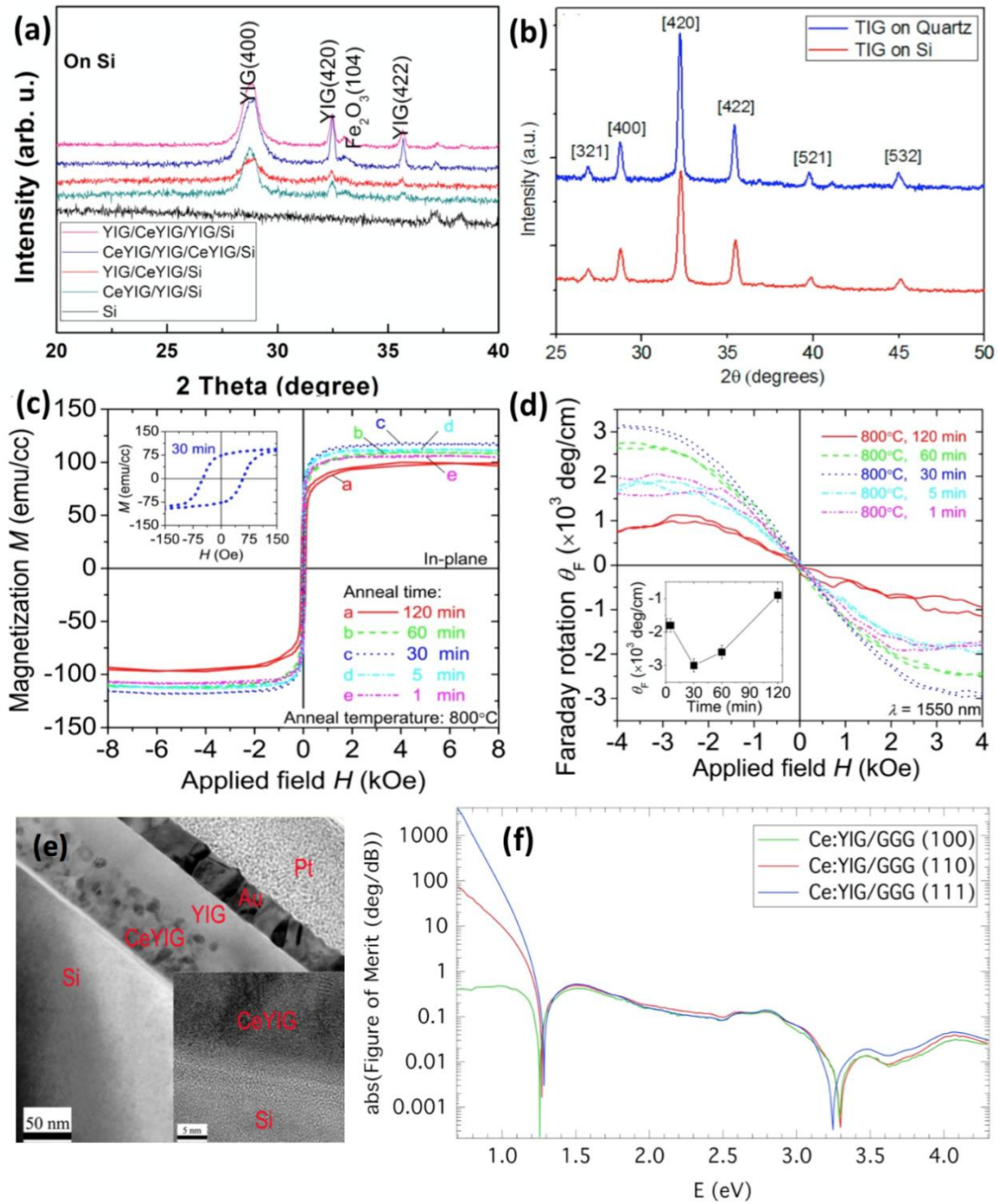


Figure 4-2. (a) X-ray diffraction (θ - 2θ) scans of pulsed laser deposition cerium-doped yttrium iron garnet (Ce:YIG) and YIG multilayer garnet films after rapid thermal annealing at 800 °C for 5 min on silicon, showing characteristic garnet peaks. [48] (b) Scans of sputtered TbIG (TIG, terbium iron garnet) on Si and quartz substrates, showing characteristic garnet peaks. Adapted with permission from Reference 53. © 2016 American Chemical Society. (c) In-plane hysteresis

loops and (d) out-of-plane Faraday rotation hysteresis loops at a wavelength (λ) of 1550 nm, with magnetic field and light propagation perpendicular to the film, for sputtered Ce:YIG on Si substrates annealed at 800 °C for various times. Inset shows the saturation Faraday rotation dependence on annealing time. [45] (e) Bright-field transmission electron microscope (TEM) cross-sectional image of YIG/Ce:YIG/silica/Si, showing large grained YIG top seed layer and fine grained Ce:YIG. Inset shows the high resolution TEM image of the interface between the film and Si substrate [48] (f) Spectral dependence of figure of merit (FOM) of single-crystal Ce:YIG films with different crystal orientation on a garnet substrate, with magnetic field and light propagation perpendicular to the film. [46]

Rare-earth garnets have also been developed for MO applications. Dulal et al. [56] sputter deposited Bi-doped terbium iron garnet (Bi:TbIG), which has the same sign of Faraday rotation as Ce:YIG and Bi:YIG, and with opposite sign of Faraday rotation as TbIG. The TbIG and Bi:TbIG can be grown directly on Si and quartz without a seed layer (Figure 4-2b), and the magnitude of Faraday rotation was up to 500 degrees/cm at 1550 nm.

Garnet films have also been incorporated into multilayer photonic structures to form magneto-photonic crystals (MPCs). For example, Yoshimoto et al. [54] demonstrated a MO structure consisting of a sputtered 423-nm-thick Ce:YIG polycrystalline film integrated between two Bragg mirrors of alternating layers of Ta₂O₅/SiO₂. The resulting Faraday rotation of the MPC was 30× higher (−2.92 degrees at 1570-nm wavelength) compared to a Ce:YIG film without the Bragg mirrors.

4.4 Novel Design of next generation TM isolator

Monolithic isolator devices based on deposited garnet materials so far only exhibit suboptimal performances in terms of isolation ratio (IR, the ratio between forward and backward transmittances, Fig. 4-3a) and insertion loss (IL, optical loss of forward propagating light through the isolator device, Fig. 4-4a), the two most important metrics for optical isolators. The largest IR to date in monolithic isolators, 19.5 dB, was attained in a nonreciprocal resonator near 1550 nm wavelength, which is unfortunately accompanied by an excessive IL of 18.8 dB [6]. A recently demonstrated quasi-phase-matched Faraday rotator achieves a reduced IL of 4.6 dB albeit with a lower IR of 11 dB [11]. These figures are far inferior compared to their free-space bulk counterparts, which claim ILs below 0.5 dB and IRs of around 40 dB at the telecommunication band [35->58]. It is therefore imperative to create new device solutions to narrow the performance gap if monolithic isolators are to secure a place in next-generation PICs.

It is worth pointing out that the quality of deposited polycrystalline garnet films is not the main performance-limiting factor in these early prototypes. For instance, Faraday rotation (FR) up to 2650 degree/cm (measured at saturation magnetization) has been obtained in deposited ferrimagnetic Ce:YIG films [59], approaching values measured in single-crystalline films of similar compositions [60,61]. Admittedly, optical loss of the deposited Ce:YIG films (40 dB/cm at 1550 nm [62]) is still considerably higher than that of their single-crystalline counterpart (< 10 dB/cm [60]). The material figure-of-merit (material

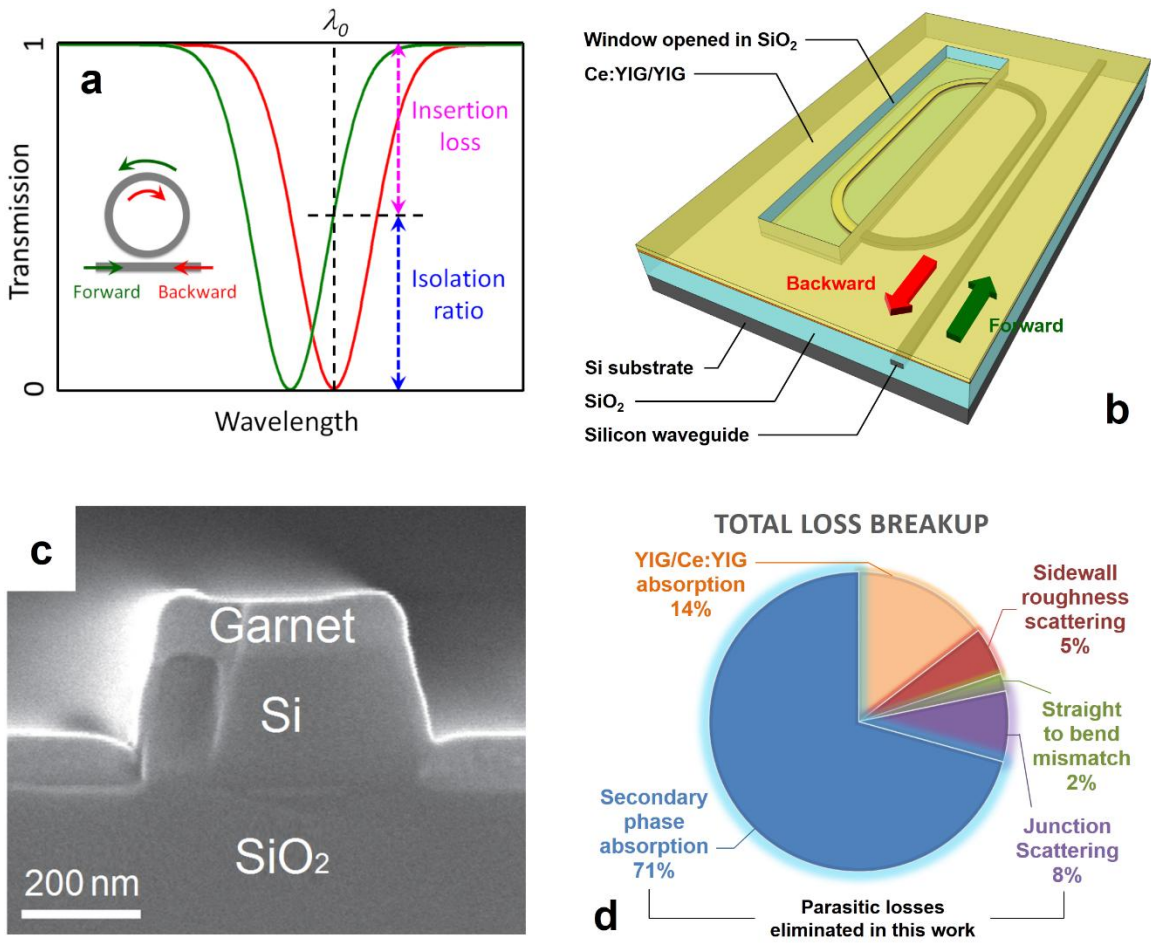


Figure 4-3. (a) Schematic transmission spectra of a resonator isolator; (b) resonator isolator structure demonstrated in [6]; (c) cross-sectional SEM image of a SOI waveguide covered with deposited magneto-optical oxides [6]; (d) breakup of loss contributions in the isolator device in [6].

FOM, defined as the ratio between FR and material loss) reaches 66 degree/dB even with such relatively high material losses, which predicts an IL down to 0.8 dB for a Faraday rotator if parasitic losses (other than material attenuation) are absent – far superior compared to the experimentally obtained performance. Understanding the non-idealities

that account for such subpar device characteristics is thus critical to further improving on-chip isolator performances.

Figure 4-3b schematically illustrates the layout of a resonator-based magneto-optical isolator. When a magnetic field is applied, degeneracy between the clockwise and counter-clockwise propagating modes of the resonator is lifted due to nonreciprocal phase shift (NRPS) in the magneto-optically active waveguide, leading to asymmetric transmission in the bus waveguide for forward and backward propagating light. The sign of NRPS depends on the direction of magnetization with respect to the light propagation direction. Therefore, unidirectional magnetization of an entire closed-loop resonator leads to vanishing resonance splitting, since NRPS on opposite sides of the resonator has different signs and cancels out. This issue can be resolved either by applying a radial magnetic field to each resonator, or keeping only part of the resonator magneto-optically active. Radial magnetization demands a needle-shaped magnet [17] or an electromagnetic micro-coil [18] to be placed in close proximity to each and every resonator, considerably increasing device complexity.

The approach of maintaining magneto-optical activity in only part of the resonator was previously implemented by opening a window in the resonator top cladding prior to garnet film deposition such that the magneto-optical film only contacts the waveguide core in the window region. Figure 1c shows a cross-sectional scanning electron microscopy (SEM) image of a silicon-on-insulator (SOI) waveguide covered with deposited garnet films fabricated using the approach [6]. In this prototypical device, the deposited film consists

of a bottom unsubstituted yttrium iron garnet (YIG) buffer layer and a Ce:YIG layer on top, the latter of which is the main magneto-optically active medium. The unsubstituted YIG buffer layer, which readily crystallizes into the garnet phase and subsequently serves as a template promoting Ce:YIG crystallization, is essential to obtaining a high-quality Ce:YIG film. Our prior work has revealed that when thickness of the YIG buffer layer is reduced to below a certain threshold value, crystallization of the top Ce:YIG layer into the magneto-optically active garnet phase is hindered [63].

The device configuration, however, incurs two undesired sources of parasitic loss. First of all, we found that it was more difficult to fully crystallize garnet films deposited on substrates with sidewall topography (e.g. waveguides) and observed greater formation of secondary phases such as iron oxide with unacceptably high optical absorption and decreased magneto-optical activity. This may be a consequence of the reduced total film thickness (and hence YIG buffer layer thickness) on the sidewalls compared to the film on top of the waveguide, as is evident from Fig. 4-3c. This issue cannot be resolved by simply increasing the overall film thickness, as the stack thickness is bound by CTE mismatch to no more than a few hundred nanometers [64]. Furthermore, the windows opened in the waveguide cladding for garnet deposition introduce junctions with abrupt index changes, causing significant scattering losses.

Figure 4-3d illustrates the different loss contributions in the isolator device in [6]. The total waveguide propagation loss of the isolator device is 58 dB/cm, calculated from the loaded

quality factor (Q-factor) and extinction ratio of the resonator using the coupling matrix formalism. Optical scattering loss at the junction between waveguide sections with and without a magneto-optical oxide top cover is modeled using an eigenmode expansion method (FIMMPROP, Photon Design Ltd.). The simulation shows that each junction causes 0.15 dB scattering loss, equivalent to 4.4 dB/cm in the resonator. Loss due to straight-to-bend waveguide modal mismatch was computed using the same approach to be 1.1 dB/cm. Sidewall roughness scattering in the waveguide was estimated from measured propagation losses of a set of resonator devices without the deposited garnet layer but with an otherwise identical configuration. As optical attenuation of the waveguide materials is negligible at the 1550 nm wavelength, the measured losses in these non-magneto-optical waveguides are pre-dominantly attributed to sidewall roughness scattering. After subtracting the straight-to-bend mismatch loss component, the sidewall roughness scattering loss was calculated to be ~ 3 dB/cm [6]. The authors reported a material absorption of 40 dB/cm measured in a planar YIG/Ce:YIG film [7]. Taking modal confinement factor in the garnet materials into account, the YIG/Ce:YIG layers result in 8.5 dB/cm loss, if the material quality was the same as the planar film. The remaining loss component is 41 dB/cm after subtracting all the contributions above. This is most likely an indication of lower quality of the garnet film grown on the device, for example due to secondary phase formation. Clearly, parasitic absorption resulting from secondary phases and scattering loss at the junctions are the major contributors accounting for 80% of the total loss. In the next section, we focus on an isolator architecture designed to eliminate these parasitic losses.

4.5 Demonstration of next generation TM isolator

The new isolator design is depicted in Figs. 4-4a (perspective view) and 4-4b (cross-section). The basic building block of the isolator is a nonreciprocal magneto-optical resonator comprising strip loaded waveguides on a deposited Ce:YIG film. The film is deposited on a planar silica-on-silicon layer and is fully crystallized into the garnet phase (confirmed by X-ray diffraction and vibrating sample magnetometry measurements) with low optical loss. By sandwiching a vertically tapered oxide spacer layer between the strip-loaded waveguide core and the Ce:YIG film, only a fraction of the micro-ring is in direct contact with the Ce:YIG layer and magneto-optically active. The oxide taper creates an adiabatic mode transformer which minimizes scattering and Fresnel reflection losses between waveguide sections with and without the spacer layer. The design therefore eliminates the two dominant sources of parasitic optical losses, i.e. absorption from secondary phases and waveguide junction scattering, which underpins the superior isolation performance we experimentally obtained in the device.

The design also features an added benefit through enhancing nonreciprocity in the waveguide. The unsubstituted YIG seed layer exhibits Faraday rotation with a sign opposite to that of Ce:YIG [59], which partially cancels out the waveguide NRPS. The deleterious effect is aggravated in the traditional waveguide structure as the YIG layer sits directly on top of the Si core, thereby having large spatial overlap with the evanescent field. In the strip-loaded waveguide configuration, the effect is alleviated since the Ce:YIG layer rather than the YIG layer is in direct contact with the waveguide core. Our numerical

modeling suggests that the configuration contributes to a 26% enhancement in NRPS of the waveguide.

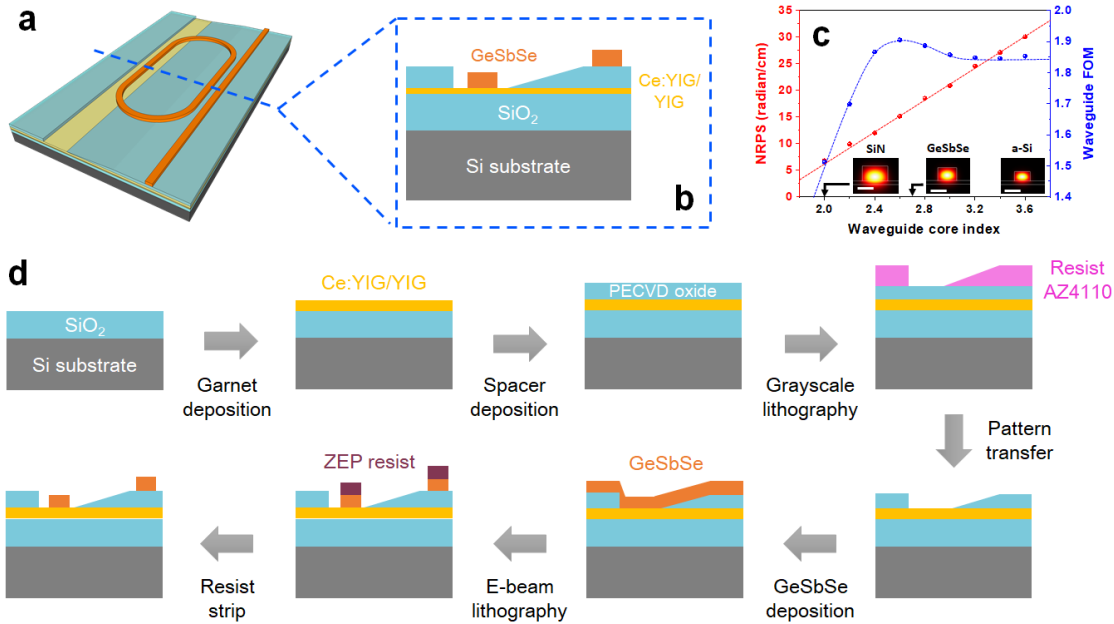


Figure. 4-4. (a) Tilted-view and (b) cross-sectional schematic of the new isolator design; (c) nonreciprocal phase shift and waveguide figure of merit computed as functions of the strip-loaded waveguide core refractive index: the insets are modal profiles of strip-loaded waveguides when the core material is chosen as silicon nitride ($n = 2.0$), GeSbSe glass ($n = 2.7$), and amorphous silicon ($n = 3.6$), where the scale bars correspond to 500 nm; (d) fabrication process flow for the isolator device.

The isolator design is further optimized through judicious choice of the waveguide core material. Figure 4-4c plots the simulated NRPS and FOM of the strip-loaded waveguide on Ce:YIG as functions of the refractive index of the core material. Here the waveguide FOM (a dimensionless quantity) is defined as:

$$\text{FOM}_{\text{WG}} = \frac{\Delta\beta}{\alpha}, \quad (5)$$

where $\Delta\beta$ denotes the waveguide NRPS for the quasi-TM mode, i.e., the propagation constant difference of forward and backward propagating modes in the waveguide (in radian per cm), and α gives the waveguide propagation loss (in cm^{-1}). The waveguide FOM scales with the material FOM defined in the previous section but additionally depends on the waveguide geometry, and ultimately dictates the performance of magneto-optical isolators [8]. In Fig. 4-4c, the waveguide dimensions are optimized to achieve maximum waveguide FOM for each core material index value while ensuring single-mode operation. The corresponding waveguide design parameters are tabulated in the Supplementary Information. The simulations show that while NRPS monotonically rises with increasing refractive index of the core over the range of indices considered, modal confinement in the Ce:YIG layer and hence optical loss also grows as a result of the reduced core thickness and increasing field discontinuity at the boundaries. The trade-off therefore points to an optimal core index of 2.6 to reach the maximum waveguide FOM.

Based on this insight, we selected $\text{Ge}_{22}\text{Sb}_{18}\text{Se}_{60}$ (GeSbSe), a chalcogenide glass (ChG) as the waveguide core material. The glass has a refractive index of 2.7 near 1550 nm wavelength, close to the optimal value of 2.6. The chemical stability and optical transparency of GeSbSe glasses have also been experimentally established [65, 66]. Moreover, we have already matured fabrication protocols for low-loss ChG photonic devices including on-chip resonators with quality factors (Q-factors) exceeding one million [67] and applied the technique to realize a wide array of functional photonic components

and systems [68-71]. The low deposition and processing temperatures of ChG further mitigates the risk of film cracking or delamination due to thermal stress accumulation [72]. We note that the isolator architecture is however generic and can also make use of other low-loss deposited dielectric materials such as silicon nitride [73] and amorphous silicon [74] as the waveguide core. Additionally, the strip-loaded waveguide layout as well as the low-loss vertical taper structure are equally applicable to enhancing the performance of other isolator device platforms such as those based on Mach-Zehnder interferometers (MZIs).

Figure 4-4d schematically illustrates the process flow to fabricate the isolator structure. Si wafers coated with 3 μm wet oxide (MTI Corp.) were used as the substrate. The wafers were first cleaned in a piranha bath to remove contaminants. 50 nm unsubstituted YIG layer was then deposited onto the substrate using pulsed laser deposition (PLD) at a substrate temperature of 400 $^{\circ}\text{C}$ and an oxygen pressure of 5 mTorr. The as-deposited YIG film is amorphous, and the film was subsequently rapid thermal annealed at 850 $^{\circ}\text{C}$ for 2 minutes to form a polycrystalline seed layer. A 90-nm Ce:YIG film was deposited onto the seed layer at a substrate temperature of 750 $^{\circ}\text{C}$ and 10 mTorr O_2 pressure using PLD. Composition of the film was quantified using inductively coupled plasma mass spectrometry (ICP-MS) to be $\text{Ce}_1\text{Y}_2\text{Fe}_5\text{O}_{12}$. The Ce:YIG film formed at the temperature spontaneously crystallizes during growth facilitated by the unsubstituted YIG seed layer. In the following step, a 500-nm silicon oxide spacer layer was deposited on top of Ce:YIG using plasma-enhanced chemical vapor deposition (PECVD) with a gas mixture of silane and N_2O at 500 mTorr pressure and a plasma power of 80 W. The oxide vertical taper

structure was subsequently defined using grayscale lithography. The continuous-tone grayscale photomask was fabricated via electron beam writing in an off-the-shelf High Energy Beam Sensitive (HEBS) glass plate (Canyon Materials, Inc.). The writing dose was calibrated following standard calibration procedures detailed elsewhere [75]. During the grayscale lithography process, 1- μm -thick AZ4110 photoresist (MicroChemicals GmbH) was spin coated onto the substrate and baked at 100 °C for 1 minute. The resist was exposed on a Karl Suss MA-4 mask aligner at a total dose of 100 mJ/cm² and then developed in AZ400K developer solution (with 1:3 dilution) for 30 s to produce the grayscale resist pattern. The pattern was subsequently transferred into the oxide layer via reactive ion etch (RIE) using a mixed etching gas of CF₄ and O₂ at 30 mTorr pressure and 200 W incident power to form the silicon dioxide vertical taper structure. The taper has a height of 500 nm and a width of 80 μm , corresponding to a taper angle of approximately 0.4 degree. The small taper angle ensures adiabatic mode transformation with negligible optical attenuation. A GeSbSe film of 360 nm thickness was thermally evaporated to function as the waveguide core layer. Patterning of the ChG waveguides followed previously established protocols which involve electron beam lithography and dry etching using a CHF₃ and CF₄ plasma [76] to complete the device fabrication.

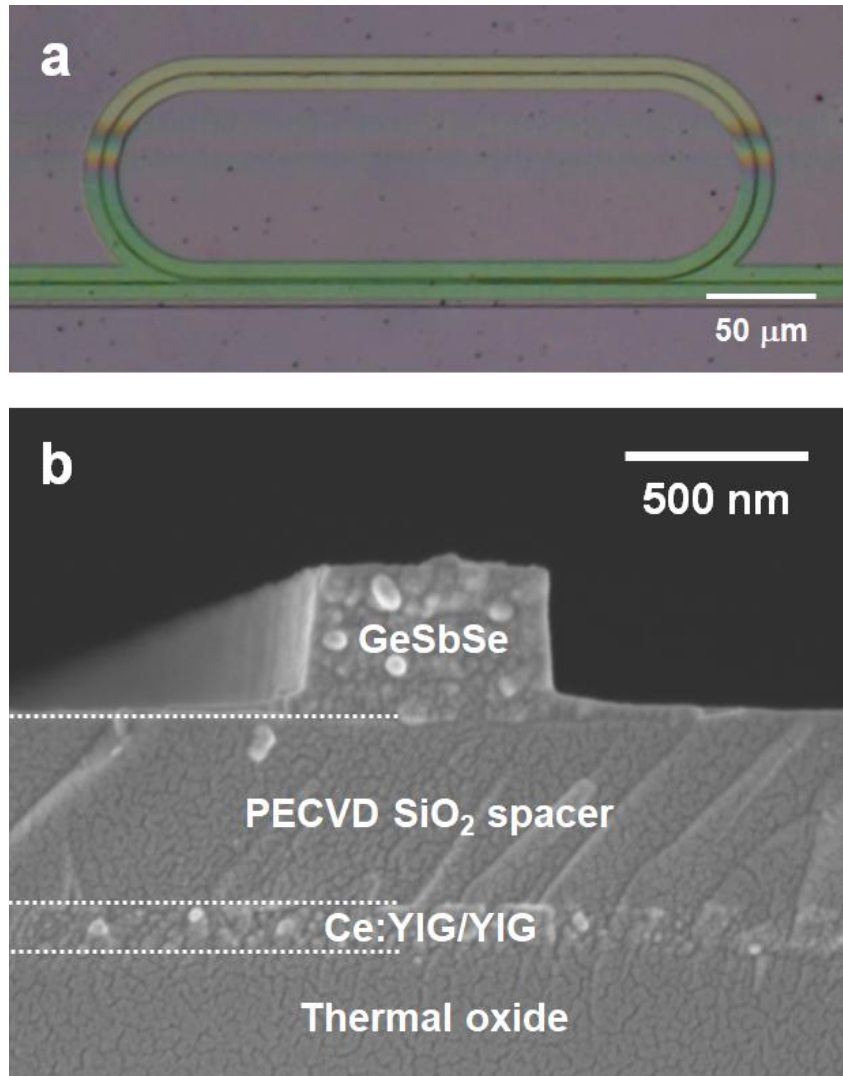


Figure. 4-5. (a) Top-view optical micrograph of a fabricated resonator isolator; (b) cross-sectional SEM image of the strip-loaded waveguide showing the layer structures.

Figure 4-5a shows a top-view optical microscope image of the fabricated resonator isolator, where the color fringes on the substrate manifest the gradual thickness variation of the oxide spacer layer. Figure 4-5b displays a cross-sectional SEM image of the ChG waveguide core sitting on the spacer layer in a region of device without the tapered spacer.

The waveguide has nearly vertical sidewalls and a well-defined width of 650 nm, an optimized value following our numerical simulation results.

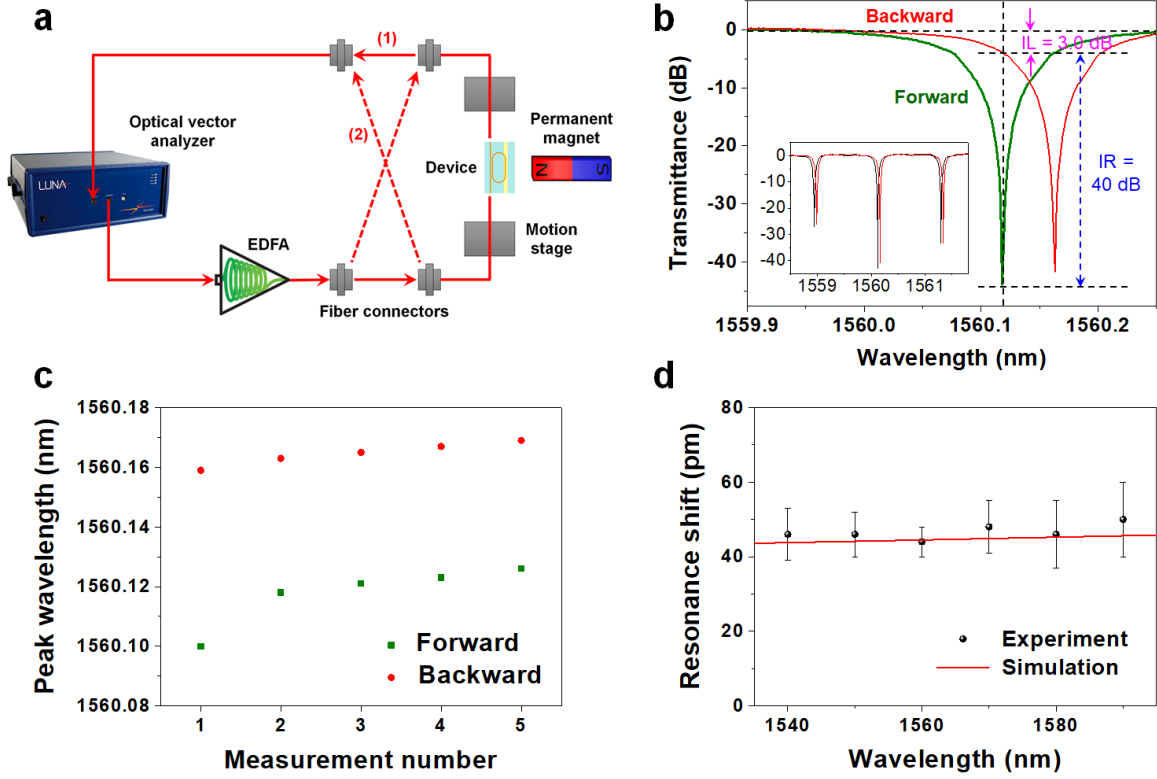


Figure 4-6. (a) Experimental setup for characterization of the isolator device: (1) and (2) indicate optical paths used to interrogate the device in forward and backward propagating directions, respectively; (b) transmission spectra of the isolator: inset shows the same spectra over several free spectral ranges of the resonator; (c) resonant peak wavelengths of the device repeatedly measured for 5 consecutive times; (d) spectral dispersion of the nonreciprocal resonant wavelength shift measured in the isolator.

Figure 4-6a illustrates a schematic diagram of the isolator characterization setup. The fabricated device was tested on a Newport Autoalign station where light was coupled in and out of the waveguides via end fire coupling through tapered fibers (Nanonics Imaging Ltd.) mounted on computerized motion stages. The device chip was covered with an index matching fluid (Cargille-Sacher Laboratories Inc.), which helps to minimize Fresnel reflection in fiber-to-chip coupling. An optical vector analyzer (OVA, Luna Innovations Inc.) with built-in external cavity tunable laser was used in conjunction with an erbium doped fiber amplifier (Amonics Ltd.) as the interrogation light source. The waveguide output spectrum was also monitored by the OVA. During the test, a rare-earth permanent magnet was placed near one end of the device chip to impose a nearly unidirectional magnetic field of approximately 0.1 T on the devices, sufficient to saturate the magnetization of the ferrimagnetic Ce:YIG film. The isolation performance was validated by reversing the light propagation direction. The measurement was repeated five consecutive times and averaged to suppress unwanted resonant peak drift due to temperature fluctuations.

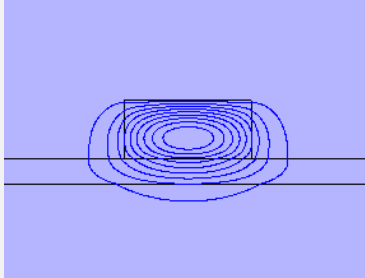
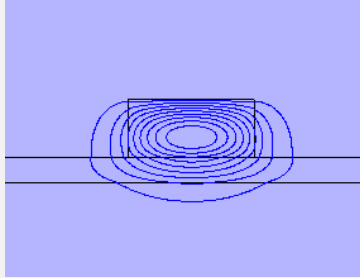
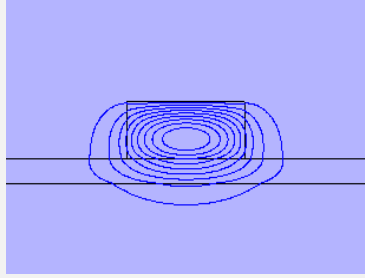
The bidirectional transmission spectra of quasi-TM mode in the isolator device are presented in Fig. 4-6b. As shown in the figure, the device exhibits an IL as low as 3.0 dB and a high IR of 40 dB, both of which set the performance records for monolithic magneto-optical isolators. The spectra, averaged over five consecutive measurements, reveal a nonreciprocal resonant peak shift of (44 ± 4) pm, in agreement with our simulation results. The resonant peak positions at both forward and backward directions recorded during the five repeated measurements are plotted in Fig. 4-6c. Wavelength dependence of the

nonreciprocal resonance shift was characterized in the wavelengths range of 1540 nm to 1590 nm. The measurement results, plotted in Fig. 4-6d alongside theoretical simulations, indicate a nearly wavelength-independent nonreciprocal resonance shift resulting from two opposing contributions: at longer wavelengths, the diminished FR of Ce:YIG [76] is balanced by a wavelength squared dependence of nonreciprocal resonance shift. We performed the simulation by the following method. Zhang et al. reported wavelength dependence of Faraday rotation in YIG/Ce:YIG polycrystalline films of the same composition ($\text{Ce}_1\text{Y}_2\text{Fe}_5\text{O}_{12}$) and grown using identical deposition parameters as films used in our study [7]. The values are quoted in the first row of Table 4-1. Waveguide model profiles simulated using a finite difference mode solver (FIMMWAVE, Photon Design Ltd.) are also included in Table 1. The nonreciprocal resonance shift is given by:

$$\Delta\lambda = \frac{2\lambda^2 L_{\text{MO}} n_{\text{TM}} \Theta_F \iint H_x \partial_y H_x dx dy}{\pi \omega \epsilon_0 n_0^3 N \cdot (L_0 n_{g,0} + L_{\text{MO}} n_{g,\text{MO}})} \quad (6)$$

Here L_0 and $n_{g,0}$ denote the length and group index of the non-magneto-optically active waveguide segment, and $n_{g,\text{MO}}$ gives the group index of the magneto-optically active waveguide segment. The dependence of nonreciprocal resonance shift on λ^2 in the numerator of Equation 6 is partially cancelled out by the decreasing Faraday rotation of the garnet material at longer wavelength, which accounts for the weak wavelength dependence of nonreciprocal resonance shift shown in Fig. 4-6d.

Table 4-1. Parameters used to model the wavelength dependence of nonreciprocal resonance shift

	1515 nm	1555 nm	1595 nm
Faraday rotation Θ_F (rad/cm)	47.7	46.7	44.9
Modal profile (H_x component)			
Confinement factor in Ce:YIG	15.7%	15.9%	16.2%
Waveguide NRPS (rad/cm)	11.81	11.80	11.75
Group index	2.98	3.01	3.04
Nonreciprocal resonance shift (pm)	43	44	46

Based on the isolator characterization outcome, we quantified the different factors contributing to the overall loss in the device. The same analysis method was also implemented to our new isolator device. We first computed the material Faraday rotation (Θ_F) via Equation 7 [2]:

$$\Theta_F = \frac{\Delta\beta_{\text{TM}} \omega \varepsilon_0 N n_0^3}{4n_{\text{TM}} \iint H_x \partial_y H_x dx dy} \quad (7)$$

where ω is the angular frequency of light, ε_0 is the vacuum permittivity, N denotes the power flux along the waveguide direction, n_0 is the refractive index of the magneto-optical material at zero magnetic field, and n_{TM} is the effective index of the waveguide quasi-TM (transverse magnetic) mode. The integration of field component H_x takes place only inside the magneto-optically active materials, and the derivative is taken along the out-of-plane (i.e. perpendicular to the substrate) direction. The waveguide NRPS, given as the propagation constant difference between forward and backward propagating quasi-TM modes, is further derived from Equation 8:

$$\Delta\beta_{\text{TM}} = \frac{2\pi \cdot \Delta\lambda}{\text{FSR} \cdot L_{\text{MO}}} \quad (8)$$

where FSR represents the free spectral range of the resonator, $\Delta\lambda$ is the measured resonant peak shift, and L_{MO} is the length of the waveguide segment that is in contact with the YIG/Ce:YIG film. Using the experimentally measured peak shift of 44 pm and an FSR of 1.17 nm, we estimated the material Faraday rotation to be ~ 2700 degree/cm, which is consistent with the value reported in [52]. In addition, we fabricated reference samples without the Ce:YIG/YIG film using following the same processing protocols, and an exemplary transmittance spectrum taken on a reference device is shown in Fig. 4-7. The device exhibits a loaded Q-factor of $\sim 100,000$, corresponding to a waveguide propagation loss of 3.8 dB/cm. Subtracting this loss value from the total loss we measured in the isolator, we estimate that the garnet material absorption accounts for ~ 13.7 dB/cm attenuation. Considering that the waveguide segment in contact with the YIG/Ce:YIG film is $\sim 200 \mu\text{m}$

in length in a resonator and that the modal confinement factor in the YIG/Ce:YIG film is 15.9% (calculated using a finite difference mode solver), the material attenuation of polycrystalline Ce:YIG/YIG was estimated to be approximately 270 dB/cm.

Total loss in the nonreciprocal resonator is computed from the measured loaded Q-factor and extinction ratio to be 17.5 dB/cm, representing over 70% reduction compared to our prior report [6]. Propagation loss of GeSbSe racetrack resonators without the underlying magneto-optical oxide layers but with an otherwise identical configuration was experimentally assessed to be 3.8 dB/cm, among which 1.1 dB/cm is attributed to scattering losses at the four straight-to-bend junctions in the racetrack resonator according to our finite-difference time-domain (FDTD) simulations. Such scattering losses can be easily eliminated by replacing the circular segments in the racetrack with a curve that has a continuous curvature change along its length, such as Euler spiral or Bezier curve [77, 78]. The remaining 2.7 dB/cm, presumably resulting from sidewall roughness scattering in the GeSbSe waveguide, is higher than the 0.5 dB/cm loss value we previously measured in ChG micro-ring resonators [67], indicating considerable room for further performance improvement. Loss caused by optical absorption in the magneto-optical oxide films is therefore 13.7 dB/cm, corresponding to 270 dB/cm absorption in the magneto-optical oxides. This figure is considerably higher than loss we previously measured in polycrystalline Ce:YIG films (40 dB/cm at 1550 nm [62]). We thus anticipate that the IL of monolithic on-chip isolators can be further minimized with optimized garnet deposition protocols to bring their performance to a level on par with or even superior to their bulk counterparts.

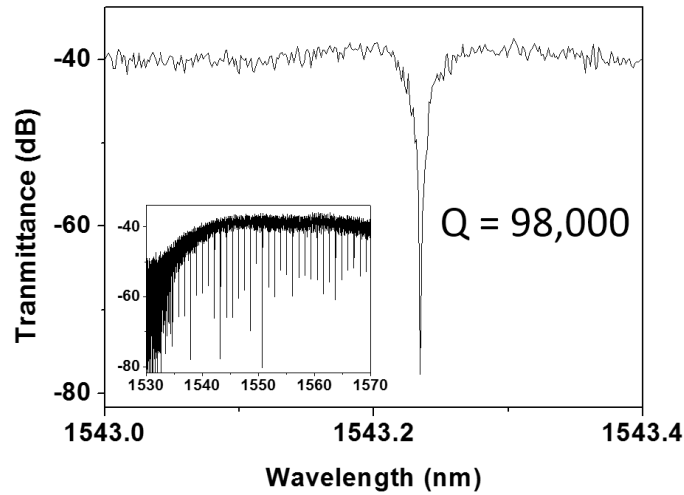


Figure. 4-7. Transmittance spectrum of a strip loaded GeSbSe racetrack resonator on a SiO₂ substrate with vertical tapers.

4.6 TE MO isolators

Besides insertion loss and isolation ratio, polarization diversity is another consideration for isolator device design. This is particularly the case for NRPS-based devices, which to date almost exclusively adopt a waveguide design similar to the one shown in Figure 4-3b. The deposited MO film on top of the waveguide core breaks the structural symmetry in the out-of-plane direction and induces NRPS for the quasi-transverse magnetic (TM) polarized modes. On the other hand, the structure's in-plane symmetry indicates a vanishing NRPS for the quasi-transverse electric (TE) polarized modes. Most integrated photonic devices, however, operate with quasi-TE polarization. The polarization mismatch can be handled

by adding on-chip polarization splitters and converters to transform the TM modes into TE modes. [79] A second solution involves coating MO materials on one waveguide sidewall to lift the in-plane symmetry for TE mode isolation. The latter scheme was recently implemented (Figure 4-3d) by forming an amorphous silicon waveguide adjacent to a patterned mesa of MO garnet grown on a garnet substrate. [21] Angled deposition of MO thin films through windows opened in a thick cladding layer offers another possible route for TE mode isolators.

SiN is another standard waveguide material widely employed in silicon photonics platforms offering unique advantages such as back-end-of-line (BEOL) compatibility and visible light transparency over Si. To date, integrated optical isolators have not yet been demonstrated on the SiN platform [59]. Here we further show that our monolithic approach can be equally applied to isolator integration on SiN through demonstration of the first TE-mode isolator on SiN. The isolator comprises a SiN racetrack resonator encapsulated in SiO₂ cladding. A window are opened in the cladding to expose one waveguide sidewall. The fabricated device is shown in Figs. 4-8a (top-view optical micrograph) and 4-8c (cross-sectional SEM). It worth noting that unlike the TM resonator isolator design demonstrated previously [6], the window can extend along the entire resonator without cancelling out NRPS as the magnetic field is applied along the out-of-plane direction. In our SiN device, the window covers the resonator device except the coupling section to avoid changing the coupling condition to the bus waveguide. Transmittance spectra of forward and backward propagation light are displayed in Fig. 4-8b, which yields an insertion loss of 11.5 dB and an isolation ratio of 20.0 dB at resonance. We further repeated the measurement multiple

times, and the data in Fig. 4-8d consistently show a resonant peak shift of (15 ± 2) pm upon reversing the light propagation direction. The result unambiguously validates nonreciprocal light propagation in the SiN device.

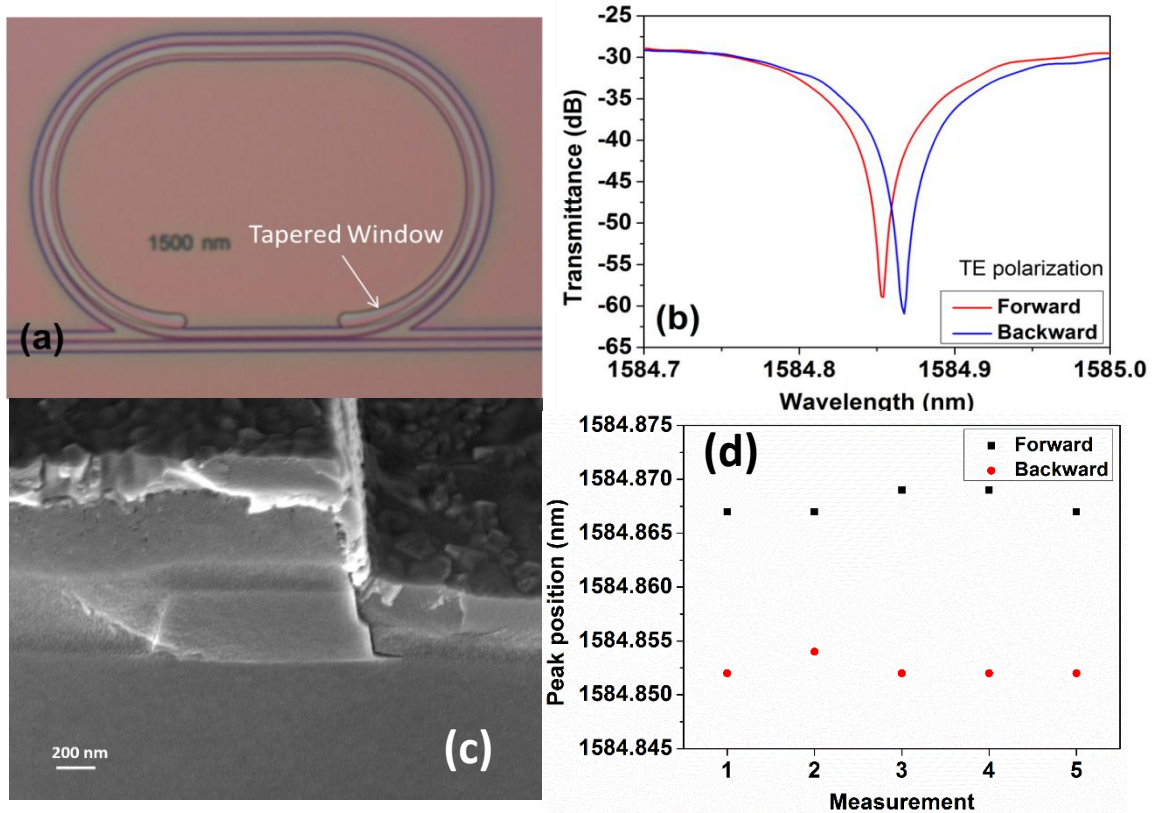


Figure. 4-8. *a) optical microscope image (top view) of as-fabricated SiN racetrack isolator. (b) forward and backward transmission spectrum of SiN isolator, we observed a 15 pm peak shift. (c) cross-sectional SEM image at the window region. (d) Recorded transmission peak position of SiN racetrack isolator. The measurement was conducted by switching light propagation direction for 5 times consecutively.*

The loss of SiN ring resonator can be extracted from its Q quality factor following the analysis protocol we previously established [6]. We measured the transmission spectra of

this device before and after MO oxide deposition, yielding a loaded Q factor of $\sim 45,000$ and $11,000$, respectively. Corresponding to a total propagation loss of 4.2 dB/cm and 17.0 dB/cm. The excess 12.8 dB/cm loss comes solely from MO oxide material absorption. Taking account a modal confinement of 5.4% and again assuming YIG and CeYIG are equally lossy. The MO oxide material loss is extracted to be 237 dB/cm. In our device design, we have added an adiabatic taper to minimize scattering losses from the window. Therefore, the only junction loss we have is the mode mismatch scattering when light propagate between straight regions to bended regions. The loss is simulated by FIMMPROP software and estimated to be 0.6 dB/cm. As we have a large bending radius of 150 μm , bending loss is <0.01 dB/cm and can be neglected. Meanwhile, we extrapolated the NRPS of MO oxide film from the peak shift and estimated to be ~ -1400 degree/cm. It is worth noting that the NRPS of sidewall deposited MO oxide exhibited only half of the FR than that was grown on a planar substrate. It is important to develop a deposition technology that achieves higher NRPS of MO oxide at the sidewall to further improve device performance.

4.7 Discussion and outlook

Performance metrics of on-chip magneto-optical isolators are summarized in Table 2. Our TM device simultaneously claims the smallest footprint, the lowest insertion loss, as well as the highest extinction ratio among monolithic magneto-optical isolators demonstrated thus far and our TE device claim to be the first experimental demonstration of NRPS based MO isolator.

For both Faraday rotators and NRPS-based isolators, performance is ultimately dictated by the FOM of the MO material. For Faraday rotators, the insertion loss (IL) is given by:

$$IL = 45 / \text{FOM} \text{ (in dB)} \quad (6)$$

For NRPS-based isolators, the waveguide design affects the NRPS (measured by phase

Table 2. Performance metrics of on-chip magneto-optical isolators

	Device structure	Monolithic integration?	Device length (mm)	Insertion loss (dB)	Isolation ratio (dB)
This work	Resonator	Y	0.29	3	40
Bi <i>et al.</i> [6]	Resonator	Y	0.29	18.8	19.5
Sun <i>et al.</i> [8]	Resonator	Y	0.29	7.4	13.0
Zhang <i>et al.</i> [11]	Faraday rotator	Y	4.1	4	11
Shoji <i>et al.</i> [12]	Interferometer	N	4.0	8	21
Ishida <i>et al.</i> [13]	Interferometer	N	> 2	10	17.9
Ghosh <i>et al.</i> [15]	Interferometer	N	~ 2	8 - 9	14
Ghosh <i>et al.</i> [16]	Interferometer	N	1.5	~ 8	11
Tien <i>et al.</i> [17]	Resonator	N	2	N/A	9
Huang <i>et al.</i> [18]	Resonator	N	0.05	10.1 - 14.3	14.4
Huang <i>et al.</i> [19]	Interferometer	N	1	9 - 11	29

delay per unit waveguide length in degrees/cm) and device performance as well. Figure 4-9c plots the ratio of waveguide NRPS and the MO material's Faraday rotation (both with the unit of degrees/cm) in an SOI waveguide capped with an MO thin film whose mode profile and cross-sectional configuration are illustrated in Figure 4-9 a-b, respectively.

Note that for all waveguide dimensions, the waveguide NRPS is less than the material's Faraday rotation.

Figure 4-9d presents the ILs of three types of isolator devices (Faraday rotators, MZIs, and micro-rings, where the latter two are both based on NRPS) versus the material FOM. Here the devices considered are ideal—for example, the only source of optical loss results from MO material attenuation, and birefringence of the rotator is assumed to vanish. A semistandard SOI waveguide with dimensions of 450 nm (width) \times 220 nm (height) is used for the MZI and microring devices. In all cases, the isolation ratio can, in theory, reach infinity (e.g., for a critically coupled micro-ring or for a power-balanced MZI), and therefore, IL is the proper device performance measure. Figure 9d indicates that Faraday rotators offer the best-in-class performance for a given MO material FOM, provided that their sensitivity to birefringence is properly addressed. This is a direct consequence of the less-than-unity ratio between waveguide NRPS and material Faraday rotation shown in Figure 4-9c.

Figure 4-9d allows us to project the performances of monolithic isolators based on available deposited MO thin films. Reliable quantification of FOM can be challenging as accurate loss evaluation in low-attenuation ($k < 10^{-3}$) MO thin films is only possible using waveguide measurements. Taking the best experimentally assessed loss data of 40 dB/cm⁵⁶ and Faraday rotation of 2650 degrees/cm⁴⁵ in PLD-deposited Ce:YIG films, we obtain a material FOM of 66 degrees/dB. The metric corresponds to ILs of 0.11 dB (micro-ring), 0.54 dB (Faraday rotator), and 1.1 dB (MZI). The result highlights the viability of

achieving high-performance optical isolation based on monolithically deposited MO thin films.

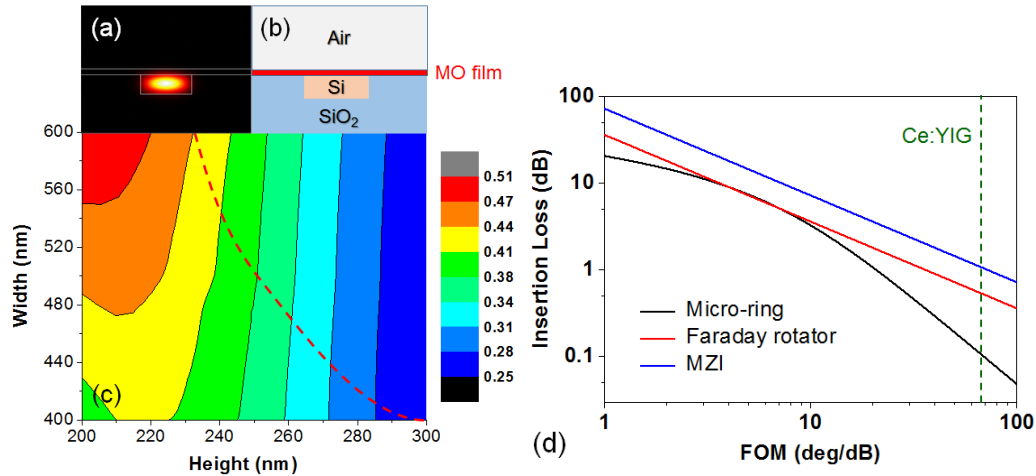


Figure 4-9. (a) Quasi-transverse magnetic (TM) mode profile and (b) cross-sectional structure of a magneto-optical (MO)-film capped silicon-on-insulator (SOI) waveguide; (c) ratio of waveguide nonreciprocal phase shift and the Faraday rotation of the MO material in the SOI waveguide illustrated in (b); the dotted line delineates the waveguide single-mode (left) and multi-mode (right) regimes. (d) Simulated insertion losses of isolators versus the MO material figure of merit (FOM). Three different device configurations: micro-ring, Faraday rotator, and Mach-Zehnder interferometers (MZI) are compared. Here, the micro-ring and MZI isolators consist of SOI waveguides shown in (b) with a core width of 450 nm and a height of 220 nm. The dotted line corresponds to the best experimentally assessed FOM in deposited cerium-doped yttrium iron garnet (Ce:YIG) films.

4.8 Conclusion

In this work, we have significantly advanced the state-of-the-art in monolithic integrated optical isolators by demonstrating an on-chip isolator with a record low insertion loss of 3.0 dB and an isolation ratio of 40 dB. The exceptional isolation performance stems from a novel device architecture combining a strip-loaded waveguide configuration with an adiabatic vertical taper, which effectively eliminates parasitic optical losses due to secondary phase absorption and junction scattering while at the same time boosting waveguide nonreciprocity. In addition, we demonstrated the first NRPS based TE isolator with 11.5 dB insertion loss and 20 dB isolation ratio. The high-performance, all-passive on-chip isolator constitutes a critical step towards planar integration of optical isolation devices with large-scale photonic circuits.

Reference

- (1) D. Jalas, A. Petrov, M. Eich, W. Freude, S. Fan, Z. Yu, R. Baets, M. Popović, A. Melloni, and J. D. Joannopoulos, *Nature Photonics* **7**, 579 (2013).
- (2) H. Däsch, N. Bahlmann, O. Zhuromskyy, M. Hammer, L. Wilkens, R. Gerhardt, P. Hertel, and A. F. Popkov, *Journal of the Optical Society of America B-Optical Physics* **22**, 240-253 (2005).
- (3) B. J. Stadler, and T. Mizumoto, *IEEE Photonics Journal* **6**, 1-15 (2014).
- (4) L. Bi, J. Hu, P. Jiang, H. S. Kim, D. H. Kim, M. C. Onbasli, G. F. Dionne, and C. A. Ross, *Materials* **6**, 5094-5117 (2013).
- (5) Y. Shoji, and T. Mizumoto, *Science and Technology of Advanced Materials* **15**, 014602 (2014).
- (6) L. Bi, J. Hu, P. Jiang, D. H. Kim, G. F. Dionne, L. C. Kimerling, and C. Ross, *Nature Photonics* **5**, 758-762 (2011).
- (7) L. Bi, J. Hu, L. Kimerling, and C. Ross, "Fabrication and characterization of $\text{as}_2\text{s}_3/\text{y}_3\text{fe}_5\text{o}_{12}$ and $\text{y}_3\text{fe}_5\text{o}_{12}/\text{soi}$ strip-loaded waveguides for integrated optical isolator applications," in *Integrated Optics: Devices, Materials, and Technologies XIV* (International Society for Optics and Photonics 2010), p. 760406.
- (8) X. Y. Sun, Q. Du, T. Goto, M. C. Onbasli, D. H. Kim, N. M. Aimon, J. Hu, and C. A. Ross, *ACS Photonics* **2**, 856-863 (2015).
- (9) T. Goto, M. C. Onbasli, D. H. Kim, V. Singh, M. Inoue, L. C. Kimerling, and C. Ross, *Opt. Express* **22**, 19047-19054 (2014).
- (10) D. C. Hutchings, B. M. Holmes, C. Zhang, P. Dulal, A. D. Block, S.-Y. Sung, N. C. Seaton, and B. J. Stadler, *IEEE Photonics Journal* **5**, 6602512-6602512 (2013).
- (11) C. Zhang, P. Dulal, B. J. Stadler, and D. C. Hutchings, *Scientific Reports* **7**, 5820 (2017).
- (12) T. Mizumoto, Y. Shoji, and R. Takei, *Materials* **5**, 985-1004 (2012).
- (13) D. Karki, V. Stenger, A. Pollick, and M. Levy, *J. Appl. Phys.* **121**, 233101 (2017).
- (14) Y. Shoji, T. Mizumoto, H. Yokoi, I.-W. Hsieh, and R. M. Osgood Jr, *Appl. Phys. Lett.* **92**, 071117 (2008).
- (15) S. Ghosh, S. Keyvavinia, W. Van Roy, T. Mizumoto, G. Roelkens, and R. Baets, *Opt. Express* **20**, 1839-1848 (2012).
- (16) S. Ghosh, S. Keyvaninia, Y. Shoji, W. Van Roy, T. Mizumoto, G. Roelkens, and R. G. Baets, *IEEE Photonics Technology Letters* **24**, 1653-1656 (2012).
- (17) M.-C. Tien, T. Mizumoto, P. Pintus, H. Kromer, and J. E. Bowers, *Opt. Express* **19**, 11740-11745 (2011).
- (18) D. Huang, P. Pintus, C. Zhang, P. Morton, Y. Shoji, T. Mizumoto, and J. E. Bowers, *Optica* **4**, 23-30 (2017).
- (19) D. Huang, P. Pintus, Y. Shoji, P. Morton, T. Mizumoto, and J. E. Bowers, *Opt. Lett.* **42**, 4901-4904 (2017).
- (20) D. Huang, P. Pintus, C. Zhang, Y. Shoji, T. Mizumoto, and J. E. Bowers, *IEEE Journal of Selected Topics in Quantum Electronics* **22**, 271-278 (2016).
- (21) E. Ishida, K. Miura, Y. Shoji, H. Yokoi, T. Mizumoto, N. Nishiyama, and S. Arai, *Opt. Express* **25**, 452-462 (2017).
- (22) J. Montoya, K. Parameswaran, J. Hensley, M. Allen, and R. Ram, *J. Appl. Phys.* **106**, 023108 (2009).
- (23) H. Shimizu, and Y. Nakano, *IEEE Photonics Technology Letters* **19**, 1973-1975 (2007).
- (24) M. Levy, T. K. Carroll, and R. El-Ganainy, *Opt. Lett.* **40**, 111-114 (2015).
- (25) Y. Shi, Z. Yu, and S. Fan, *Nature Photonics* **9**, 388-392 (2015).
- (26) L. Fan, J. Wang, L. T. Varghese, H. Shen, B. Niu, Y. Xuan, A. M. Weiner, and M. Qi, *Science* **335**, 447-450 (2012).

- (27) L. Chang, X. Jiang, S. Hua, C. Yang, J. Wen, L. Jiang, G. Li, G. Wang, and M. Xiao, *Nature Photonics* **8**, 524 (2014).
- (28) B. Peng, Ş. K. Özdemir, F. Lei, F. Monifi, M. Gianfreda, G. L. Long, S. Fan, F. Nori, C. M. Bender, and L. Yang, *Nature Physics* **10**, 394 (2014).
- (29) L. Del Bino, J. M. Silver, M. T. Woodley, S. L. Stebbings, X. Zhao, and P. Del'Haye, *Optica* **5**, 279-282 (2018).
- (30) Z. Yu, and S. Fan, *Nature Photonics* **3**, 91 (2009).
- (31) H. Lira, Z. Yu, S. Fan, and M. Lipson, *Phys. Rev. Lett.* **109**, 033901 (2012).
- (32) Y. Yang, C. Galland, Y. Liu, K. Tan, R. Ding, Q. Li, K. Bergman, T. Baehr-Jones, and M. Hochberg, *Opt. Express* **22**, 17409-17422 (2014).
- (33) C. Doerr, L. Chen, and D. Vermeulen, *Opt. Express* **22**, 4493-4498 (2014).
- (34) S. Manipatruni, J. T. Robinson, and M. Lipson, *Phys. Rev. Lett.* **102**, 213903 (2009).
- (35) T. Shintaku, A. Tate, and S. Mino, *Appl. Phys. Lett.* **71**, 1640-1642 (1997).
- (36) H. Hemme, H. Dätsch, P. Hertel, *Appl. Opt.* **29**, 2741 (1990).
- (37) L. Tang, S. Drezdzon, T. Yoshie, *Opt. Express* **16**, 16202 (2008).
- (38) R. El-Ganainy, P. Kumar, M. Levy, *Opt. Lett.* **38**, 61 (2013).
- (39) J. Montoya, K. Parameswaran, J. Hensley, M. Allen, R. Ram, *J. Appl. Phys.* **106**, 023108 (2009).
- (40) J. Hammer, G. Ozgur, G. Evans, J. Butler, *J. Appl. Phys.* **100**, 103103 (2006).
- (41) H. Yokoi, T. Mizumoto, Y. Shoji, *Appl. Opt.* **42**, 6605 (2003).
- (42) J. Fujita, M. Levy, R. Osgood, L. Wilkens, H. Dätsch, *Appl. Phys. Lett.* **76**, 2158 (2000).
- (43) Y. Shoji, T. Mizumoto, *Opt. Express* **15**, 639 (2007).
- (44) N. Kono, K. Kakihara, K. Saitoh, M. Koshihara, *Opt. Express* **15**, 7737 (2007).
- (45) H. Zhu, C. Jiang, *J. Lightwave Technol.* **29**, 1647 (2011).
- (46) J. Yang, J. Roh, S. Ok, D. Woo, Y. Byun, W. Lee, T. Mizumoto, S. Lee, *IEEE Trans. Magn.* **41**, 3520 (2005).
- (47) K. Shui, L. Nie, Y. Zhang, B. Peng, J. Xie, L. Deng, L. Bi, *Opt. Express* **24**, 12856 (2016).
- (48) N. Kono, M. Koshihara, *Opt. Express* **13**, 9155 (2005).
- (49) T. Boudiar, B. Payet-Gervy, M.-F. Blanc-Mignon, J.-J. Rousseau, M. Le Berre, H. Joisten, *J. Magn. Magn. Mater.* **284**, 77 (2004).
- (50) S. Sung, X. Qi, B. Stadler, *Appl. Phys. Lett.* **87**, 121111 (2005).
- (51) S. Sung, X. Qi, B. Stadler, in *Conference on Lasers and Electro-Optics* (Optical Society of America, 2007), p. CThN5.
- (52) M. Onbasli, L. Beran, M. Zahradnik, M. Kučera, R. Antoš, J. Mistrík, G. Dionne, M. Veis, C. Ross, *Sci. Rep.* **6**, 23640 (2016).
- (53) J. Hu, X. Sun, Q. Du, M. Onbasli, C. Ross, *Proc. SPIE* (2016), vol. 9750, p. 97500W-1.
- (54) B. Stadler, T. Mizumoto, *IEEE Photon. J.* **6**, 1 (2014).
- (55) P. Hansen, J. Krumme, *Thin Solid Films* **114**, 69 (1984).
- (56) M.C. Onbasli, T. Goto, X. Sun, N. Huynh, C.A. Ross, *Opt. Express* **22** (21), 25183 (2014).
- (57) P. Dulal, A. Block, T. Gage, H. Haldren, S. Sung, D. Hutchings, B. Stadler, *ACS Photonics* **3**, 1818 (2016).
- (58) "Ir free-space isolators," https://www.thorlabs.com/newgrouppage9.cfm?objectgroup_id=4916.
- (59) M. C. Onbasli, T. Goto, X. Sun, N. Huynh, and C. Ross, *Opt. Express* **22**, 25183-25192 (2014).

- (60) T. Shintaku, A. Tate, and S. Mino, *Appl. Phys. Lett.* **71**, 1640-1642 (1997).
- (61) M. C. Onbasli, L. Beran, M. Zahradnik, M. Kučera, R. Antoš, J. Mistrik, G. F. Dionne, M. Veis, and C. A. Ross, *Scientific Reports* **6**, 23640 (2016).
- (62) L. Bi, J. Hu, G. F. Dionne, L. Kimerling, and C. Ross, "Monolithic integration of chalcogenide glass/iron garnet waveguides and resonators for on-chip nonreciprocal photonic devices," in *Integrated Optics: Devices, Materials, and Technologies XV* (International Society for Optics and Photonics 2011), p. 794105.
- (63) T. Goto, M. C. Onbaşlı, and C. A. Ross, *Opt. Express* **20**, 28507-28517 (2012).
- (64) S.-Y. Sung, A. Sharma, A. Block, K. Keuhn, and B. J. H. Stadler, *J. Appl. Phys.* **109**, 07B738 (2011).
- (65) W.-H. Wei, R.-P. Wang, X. Shen, L. Fang, and B. Luther-Davies, *The Journal of Physical Chemistry C* **117**, 16571-16576 (2013).
- (66) M. R. Krogstad, S. Ahn, W. Park, and J. T. Gopinath, *Opt. Express* **23**, 7870-7878 (2015).
- (67) Q. Du, Y. Huang, J. Li, D. Kita, J. Michon, H. Lin, L. Li, S. Novak, K. Richardson, and W. Zhang, *Opt. Lett.* **41**, 3090-3093 (2016).
- (68) Q. Du, Z. Luo, H. Zhong, Y. Zhang, Y. Huang, T. Du, W. Zhang, T. Gu, and J. Hu, *Photonics Research* **6**, 506-510 (2018).
- (69) L. Li, H. Lin, Y. Huang, R.-J. Shiue, A. Yadav, J. Li, J. Michon, D. Englund, K. Richardson, and T. Gu, *Optica* **5**, 44-51 (2018).
- (70) H. Lin, Y. Song, Y. Huang, D. Kita, S. Deckoff-Jones, K. Wang, L. Li, J. Li, H. Zheng, and Z. Luo, *Nature Photonics* **11**, 798-805 (2017).
- (71) L. Li, H. Lin, S. Qiao, Y. Zou, S. Danto, K. Richardson, J. D. Musgraves, N. Lu, and J. Hu, *Nature Photonics* **8**, 643-649 (2014).
- (72) J. Hu, L. Li, H. Lin, Y. Zou, Q. Du, C. Smith, S. Novak, K. Richardson, and J. D. Musgraves, *Am. Ceram. Soc. Bull.* **94**, 24-29 (2015).
- (73) J. F. Bauters, M. J. Heck, D. John, D. Dai, M.-C. Tien, J. S. Barton, A. Leinse, R. G. Heideman, D. J. Blumenthal, and J. E. Bowers, *Opt. Express* **19**, 3163-3174 (2011).
- (74) S. K. Selvaraja, E. Sleenckx, M. Schaekers, W. Bogaerts, D. Van Thourhout, P. Dumon, and R. Baets, *Opt. Commun.* **282**, 1767-1770 (2009).
- (75) T. E. Dillon, A. Sure, J. A. Murakowski, and D. W. Prather, *Journal of Micro/Nanolithography, MEMS, and MOEMS* **3**, 550-555 (2004).
- (76) Y. Zhang, C. Wang, X. Liang, B. Peng, H. Lu, P. Zhou, L. Zhang, J. Xie, L. Deng, and M. Zahradnik, *J. Alloys Compd.* **703**, 591-599 (2017).
- (77) M. Cherchi, S. Ylinen, M. Harjanne, M. Kapulainen, and T. Aalto, *Opt. Express* **21**, 17814-17823 (2013).
- (78) L. Li, H. Lin, S. Qiao, Y.-Z. Huang, J.-Y. Li, J. Michon, T. Gu, C. Alosno-Ramos, L. Vivien, and A. Yadav, *Light: Science & Applications* **7**, 17138 (2018).
- (79) D. Dai, J. Bauters, J.E. Bowers, *Light Sci. Appl.* **1**, e1 (2012).

Chapter 5. Radiation Induced Effects in Silicon Photonic

Materials and Devices

5.1 Radiation Overview

Understanding radiation damage is of significant importance for devices operating in radiation-harsh environments. High energy radiation tends to create defects in materials and thereby modify their electronic and optical properties. Mitigating radiation-induced damage associated with such defect generation is an important design consideration for devices used in outer space, near nuclear reactors, or close to particle colliders. As satellite communications and data links for next-generation particle accelerators start turning to integrated photonics solutions, [1] the demand to understand radiation-induced degradation mechanisms in photonic devices becomes critical. In nuclear and space environment, radiation includes alpha ray (He ions), beta ray (electrons), gamma ray (photons) and neutrons. In general, radiation damage can be categorized into two types, ionization damage and displacement damage. Ionization dose produces density and polarization variation as well as free carrier accumulation in materials which shifts material refractive index and losses. This type of damage is usually caused by fast moving charged particles and photons. While displacement damage creates defects in mid gap, contributing to a modification of charge trapping and carrier lifetime, thus changes material optical properties, and heavy ions bombardment tends to create such effects.

In crystalline optical materials such as silicon on insulator (SOI), optical property changes occur through both ionization damage and displacement damage [2]. Ionization leads to free carriers which modify refractive index and optical absorption via the plasma dispersion effect. Ionization damage also creates trapped charges at the Si/SiO₂ interface which likely accounts for the phase drift observed in SOI modulators [3]. Displacement damage results in lattice defects which impacts optical properties through local polarizability change and carrier density modulation due to trap states. Gamma radiation-induced effects in SOI have been characterized by both in-situ [4] and ex-situ [5] measurements using optical resonator devices. Besides the aforementioned bulk material structural transformations, surface oxidation was identified as a contributor to observed resonance spectral shift [5].

In this chapter, we first discuss simulation method and show preliminary results from alpha radiation on silicon nitride samples. Then detailed quantitative study is conducted for gamma radiation on a-Si, SiN_x and SiC materials and devices. The origin of the observed device behavior modification is also discussed.

5.2 Stopping Range of Ions in Mater (SRIM)

Even though the energy of the alpha particles is comparable to that of the Co⁶⁰ gamma rays, the nature of the two radiations is fundamentally different. Alpha particles can create damage cascades due to their high mass which creates areas with high densities of defects. The mechanism of interaction of the alpha particles with the lattice atoms is twofold. First, the ion is too energetic to directly interact with the nuclei, but due to its positive charge, it

strongly interacts with the electron cloud of the semiconductor losing energy and creating defects at a constant rate. This is known as the electronic stopping phase. Once it has

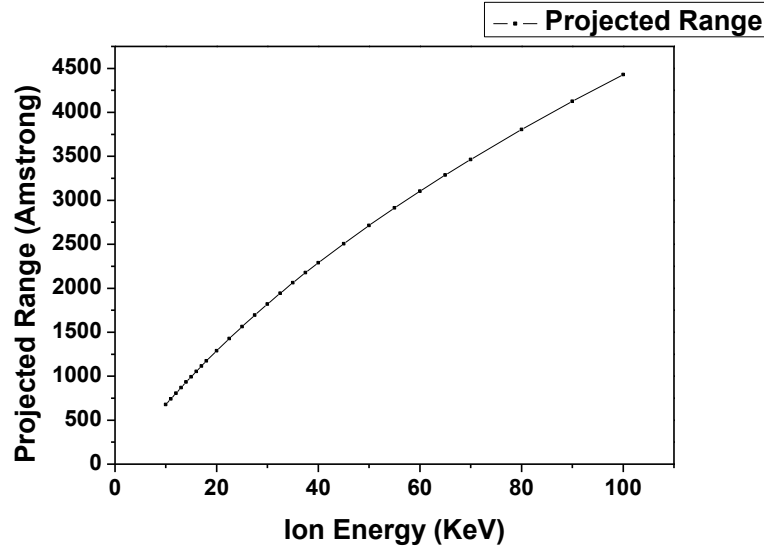


Figure 5-1 – Stopping range plot of alpha particles with different energies.

slowed down enough, the ion starts colliding with nuclei, losing its energy very quickly creating cascaded damage (the knocked-out nucleus can further displace other nuclei). This is known as the nuclear stopping phase, during which the ion loses all of its remaining energy very quickly. Due to these two stopping mechanisms, the damage in the irradiated material is not homogeneously distributed; the defect concentration increases slightly in the electronic stopping region (which is of the order of a micrometer long depending on the initial energy), peaks in the nuclear stopping region (also called end of range (EOR) which is around 100 nanometers long in our experiments). After the end of range, no defects are produced anymore. We used the software “Stopping and Ion Range in Matter” (SRIM) to simulate the damage distribution so that we could determine the optimal

irradiation energy for our experiments. Figure 5-1 shows alpha particle (helium ion) stopping range in silicon nitride. Detailed damage is calculated and shown in Figure 5-2. The ionization energy loss rate as the particles penetrate into the material is described by Linear Energy Transfer function (LET) while the displacement damage event is reflected

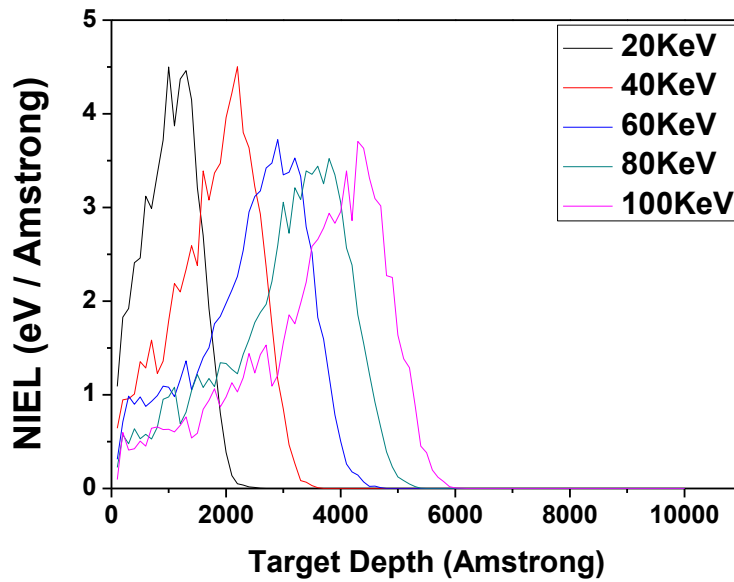
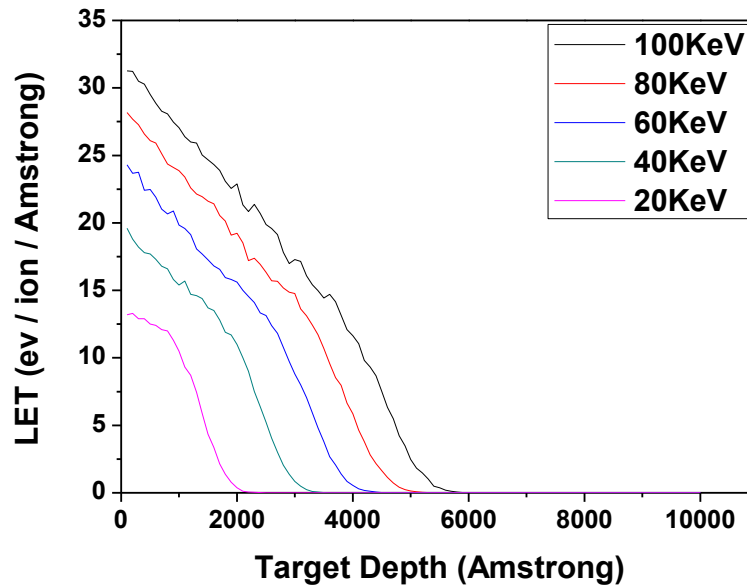


Figure 5-2 – LET and NIEL of alpha particle damage with energies ranging from 20KeV to 100KeV on silicon nitride film. From the simulation, we conclude that for silicon nitride device with 400 nm thickness, alpha irradiation with energy of ~60 keV should be chosen in our irradiation experiments as it can induce most damage inside the material, and can yield insights into the upper and lower limits for rad-hardness.

by Non-Ionization Energy Loss (NIEL). The energy range from 20 keV to 100 keV is used for the calculation.

From the simulation, we conclude that for silicon nitride device with 400 nm thickness, alpha irradiation with energy of ~60 keV should be chosen in our irradiation experiments as it can induce most damage inside the material, and can yield insights into the upper and lower limits for rad-hardness.

Optical resonator devices were used to evaluate the radiation induced optical property modification of the materials and the impact on photonic device performance. The devices were fabricated using the following steps: a 400 nm thick silicon nitride film was first deposited onto silicon wafer with 3 μm thermal oxide on top. SPR-700 photoresist was then spin-coated and an i-line stepper was used to pattern 800 nm wide waveguide resonator. The as-patterned silicon nitride films were patterned in a Reactive Ion Etching (RIE) plasma etcher. An equal amount of CHF_3 and CF_4 gas mixture was flowed into the chamber to transfer the pattern into the silicon nitride. Finally, residual photoresist was removed by putting the chip into a piranha solution (75% H_2SO_4 + 25% H_2O_2).

Transmission spectrum of the resonators were measured via a fiber butt coupling method. A tunable laser of wavelength ranging from 1500 nm to 1600 nm was used as the light source. The optical resonators were measured before and after irradiation and their temperature was controlled within less than 0.2 °C.

The radiation was carried out in PNNL at an alpha irradiator with an energy of 5MeV. Figure 5-3 shows the transmission spectra of alpha irradiated resonators. The large resonant shifts indicate that it is mandatory to protect SiN resonators against surface oxidation if they were used in a radiation environment.

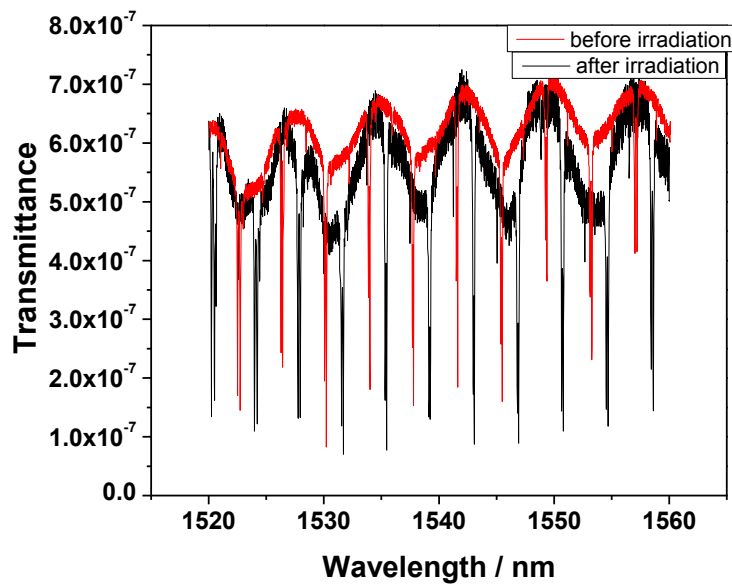


Figure 5-3 – Transmission spectra of silicon nitride resonators before and after alpha irradiation

5.3 Gamma Radiation Damage in a-Si and SiN_x Materials and Devices

In this study, we focus on gamma radiation-induced effects in amorphous silicon (a-Si) and silicon nitride (SiN_x) photonic devices. Both a-Si and SiN_x have low optical loss near 1550 nm telecommunication wavelength [6]. For instance, SiN_x waveguides with a remarkably low optical loss down to 0.045 dB/m have been demonstrated [7]. Their amorphous nature and compatibility with standard Si CMOS processing also qualify them as promising candidates for back end of line (BEOL) photonic integration [8]. Additionally, both materials exhibit large Kerr coefficients useful for nonlinear optical applications [9,10].

Radiation damage in a-Si has been investigated in electronic devices including field effect transistors [11], photodetectors [12] and solar cells [13]. In electronic devices, it was concluded that ionization damage is the primary degradation mechanism [14]. For passive photonic applications, however, bulk optical property changes in a-Si are likely dictated by atomic structural perturbations resulting from displacement defects. This is different from the case of crystalline silicon, because free carrier effects (plasma dispersion and free carrier absorption) are minimal in a-Si given its small carrier mobility. Likewise, we anticipate that displacement is the main damage mechanism in SiN_x materials.

On the experimental side, radiation effects on a-Si and SiN_x photonic devices have only been reported in a few recent studies. Grillanda *et al.* studied gamma radiation damage in a-Si resonators covered with a silicon dioxide cladding grown by chemical vapor deposition (CVD) and found minimal resonance shift up to 15 Mrad absorbed dose [15]. This observation is likely a consequence of cladding compensation as CVD silicon dioxide exhibits a negative refractive index

change upon gamma ray exposure. In nitride devices, proton irradiation up to a total fluence of $\sim 10^{10}$ protons/cm² produced negligible loss change [16]. In silicon oxynitride waveguides, a large index change in the order of 0.01 was measured upon exposure to alpha radiation [17].

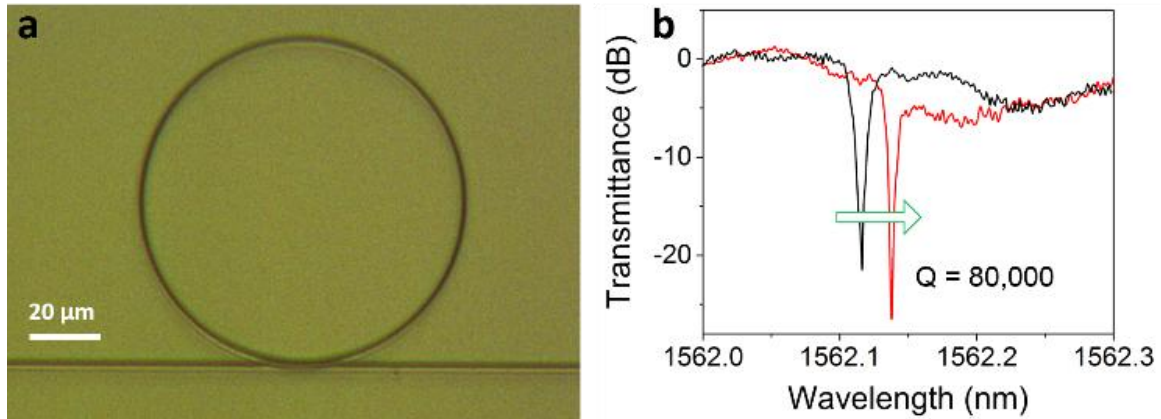


Figure 5-4. (a) Top-view optical microscope image of an a-Si micro-ring resonator; (b) transmission spectra of the a-Si resonator before (black curve) and after (red curve) receiving 2 Mrad gamma irradiation

The present work aims to provide a precise, quantitative measurement of total dose effect of gamma irradiation on a-Si and SiN_x photonic devices. Radiation-induced optical property modifications are evaluated using micro-ring resonators. Refractive index change of a-Si and SiN_x can be calculated from the resonant peak shift whereas optical absorption increase, if any, is inferred from the extinction ratio change [18]. The irradiated a-Si and SiN_x materials were also characterized by high resolution transmission electron microscopy (HRTEM), grazing incidence X-ray diffraction (XRD), and X-ray photoelectron Spectroscopy (XPS) to elucidate the underlying structural transformation mechanisms responsible for the observed optical property modifications.

Fabrication of a-Si and SiN_x resonators followed the standard Si microfabrication processes. Thin film a-Si and silicon nitride was first deposited onto silicon wafers with 3 μm thermal oxide using plasma enhanced chemical vapor deposition (PECVD) and low pressure chemical vapor deposition (LPCVD), respectively. The SiN_x film has a refractive index of 2.1 at 1550 nm wavelength (compared to an index of 2.0 for stoichiometric Si₃N₄) and is thus silicon-rich. The a-Si devices were patterned using electron beam lithography, whereas photolithography performed on an i-line stepper was used to define the SiN_x device structures. Subsequently, the patterns were transferred to the film by reactive ion etch with Cl₂ for a-Si and a mixture of CF₄ and CHF₃ gases for nitride. The as-fabricated a-Si waveguide has dimensions of 450 nm (width) by 250 nm (height), and SiN_x waveguide has a cross section of 800 nm × 400 nm. Figure 5-4a shows the top view of an a-Si resonator used in our experiment.

Optical transmission spectrum of the devices was characterized on a Newport Auto Align workstation equipped with an optical vector analyzer (LUNA Technologies OVA-5000) and a built-in tunable laser. Near-infrared light was coupled in and out of the resonators through bus waveguides using tapered lens-tip fibers. The loaded quality factors (Q-factors) of as-fabricated a-Si and SiN_x resonators are both around 10⁵.

Gamma irradiation of the devices was conducted using a Co-60 source with photon energies of 1.17 MeV and 1.33 MeV. For the experiments described herein, every as-fabricated device chip was diced into two nominally identical pieces. One of them (the “sample”) was exposed to gamma irradiation while the other (the “reference”) was kept in an otherwise identical environment (i.e. at the same temperature, humidity, and lighting conditions). Post-irradiation measurements were

performed with the devices mounted on a thermostat stage maintained at a constant temperature of (19.7 ± 0.2) °C. The radiation-induced resonance shift $\Delta\lambda$ is calculated via:

$$\Delta\lambda = (\lambda_0 - \lambda_{0,r}) - (\lambda_1 - \lambda_{1,r}), \quad (1)$$

where λ_0 and λ_1 denote the resonant wavelengths of the sample before and after gamma irradiation, and $\lambda_{0,r}$ and $\lambda_{1,r}$ are the resonant wavelengths of the reference measured under identical conditions. The use of a reference chip allows us to eliminate environmental noise interfering with precise index quantification. In the experiments, we can reliably measure index change down to 2×10^{-6} in SiN_x and 5×10^{-5} in a-Si, with the measurement accuracy ultimately limited by temperature stability of the thermostat stage. Fig. 5-4b plots an example of device transmission spectra for an a-Si resonator prior to and after exposure to 2 Mrad gamma irradiation (dose calibrated to silicon). The extinction ratio and Q-factor remain unchanged, signaling negligible loss increase after gamma irradiation. To ascertain that the thermal oxide undercladding does not contribute significantly to the observed peak shift, we quantified the refractive indices of thermal oxide films before and after gamma irradiation using variable angle spectroscopic ellipsometry (VASE). The ellipsometry measurement consistently yielded identical indices for thermal oxide before and after gamma irradiation doses up to 20 Mrad. Standard deviation of the index measurement is less than 2×10^{-4} . Considering that the modal confinement factor in the undercladding is only about 6% and 23% in a-Si and SiN_x devices, respectively, we conclude that the contribution from thermal oxide to the post-irradiation resonance shift is insignificant.

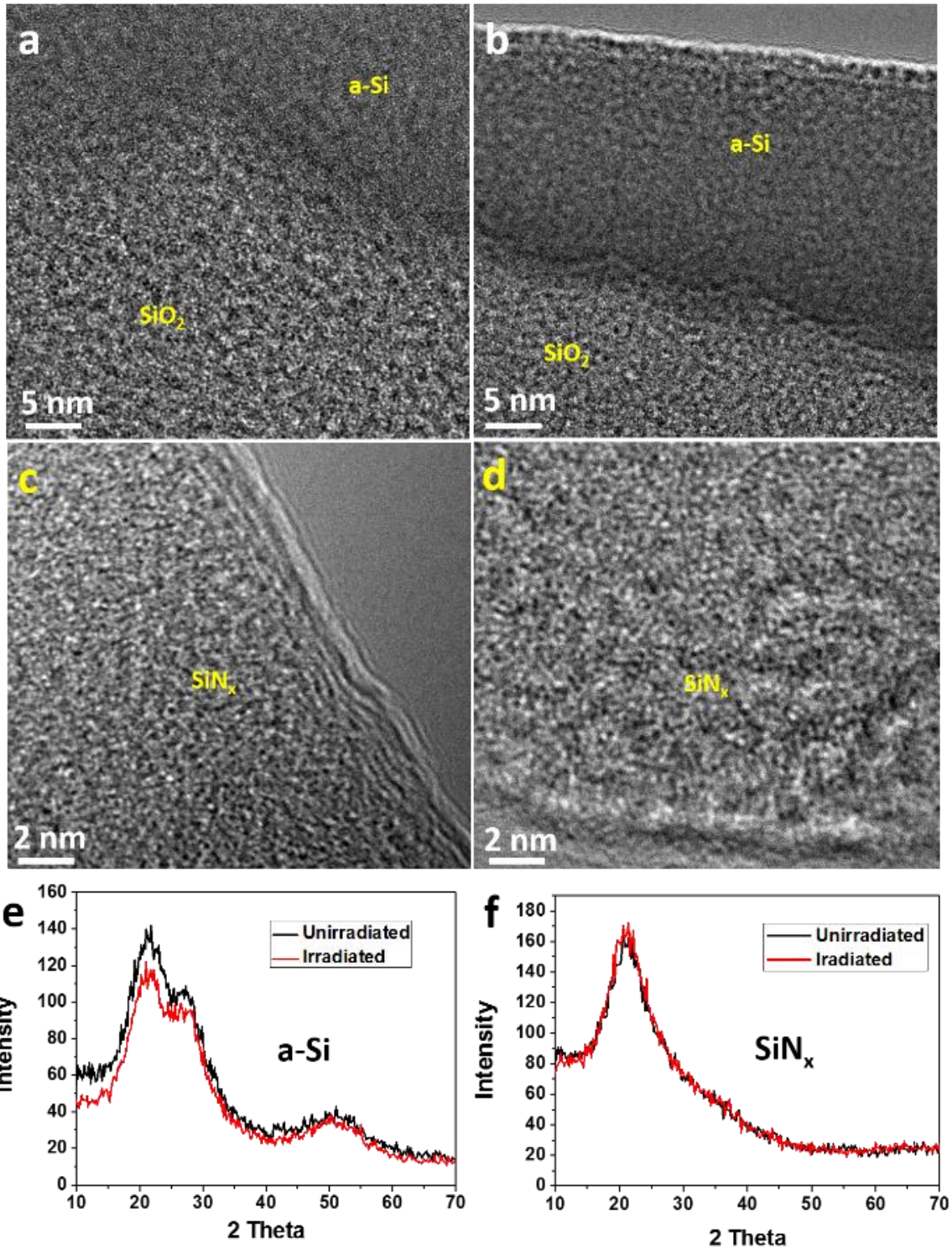


Figure 5-5. HRTEM images of *a*-Si sample before (a) and after (b) 20 Mrad radiation. (c) and (d) are the corresponding images of a SiN_x film before and after radiation under same dose. (e) and (f): XRD spectra of *a*-Si and SiN_x thin film before and after 20 Mrad gamma irradiation, respectively.

HRTEM images (shown in Fig. 5-5) were taken on a-Si and SiN_x films before and after irradiation. The HRTEM samples were prepared by ion milling to obtain a ~20 nm thick lamella for imaging. Images before (Figs. 5-5a and 5-5c) and after (Figs. 5-5b and 5-5d) receiving 20 Mrad radiation dose do not exhibit discernable structural differences. No signs of crystallization were found after examining >10 HRTEM images. The absence of radiation-induced crystallization is further confirmed by the XRD spectra plotted in Figs. 5-5e and 5-5f, where no sharp diffraction peaks were identified after irradiation. The results exclude radiation-induced crystallization found in several amorphous material systems including a-Si [19-21] as a possible mechanism for the observed refractive index increase.

While HRTEM and XRD do not reveal clear signatures of radiation effects, XPS analysis shows surface chemistry modification as a result of gamma irradiation. Figure 5-6a plots the XPS spectrum of the silicon 2p peak in as-deposited a-Si film. The spectra can be deconvolved into two peaks, corresponding to Si-Si bonds at a binding energy of ~99 eV and Si-O bonds at ~103 eV. Relative concentrations of the two types of bonds can be determined by comparing the areas under the deconvolved peaks. The black curve in Fig. 5-6b plots the calculated Si-O bond fractions in as-deposited and gamma irradiated (irradiated at 1 Mrad and 10 Mrad doses in air) a-Si films. The increased Si-O bond fraction indicates native oxide layer growth catalyzed by gamma irradiation. This is not surprising since highly energetic photon beams such as gamma and X-rays are known to decompose oxygen molecules in air into reactive species such as O[•] and ozone, and it has been shown that these highly reactive species contribute to accelerated surface oxide growth in crystalline silicon [5,22]. To unequivocally identify the surface oxidation effect, we performed a second set of irradiation experiments using samples sealed inside ultra-high-purity (oxygen

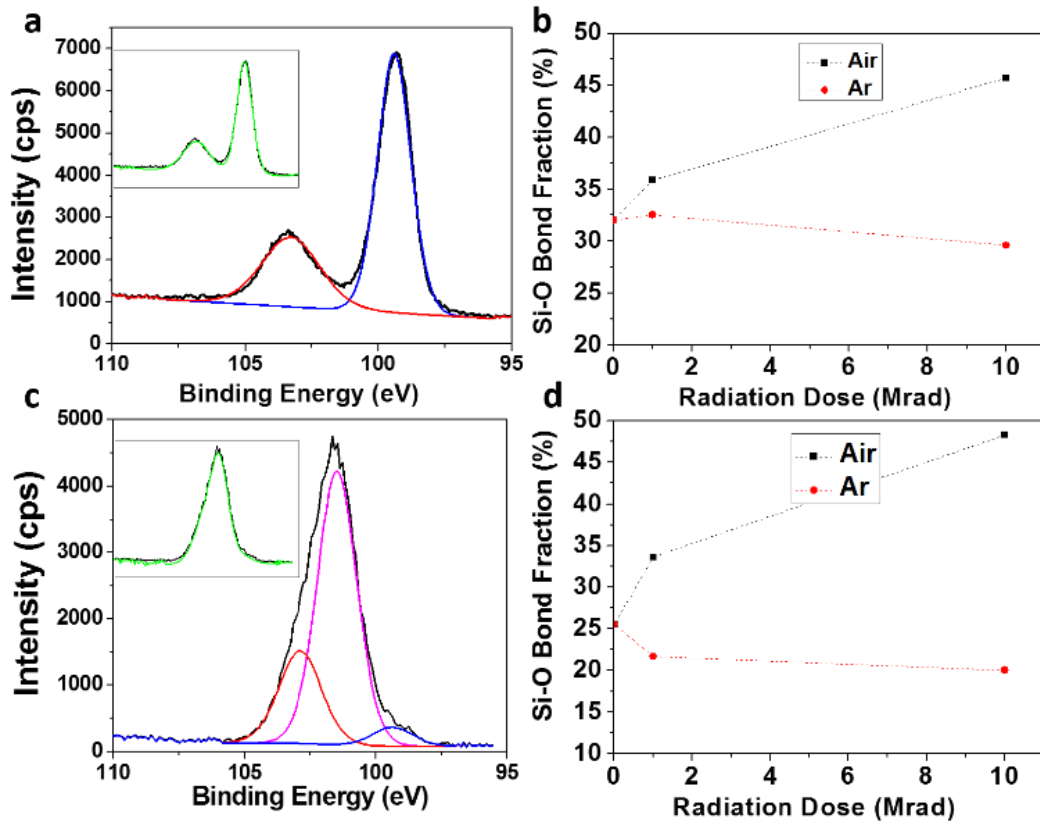


Figure 5-6. (a) and (c): Si 2p peak from a high resolution XPS scan of as-deposited (a) a-Si and (c) SiN_x films. The spectra are deconvoluted into different Si bonding states, where the red curves correspond to Si-O bond, the blue curve are assigned to Si-Si bond and the pink curves are associated with Si-N bond. The Insets show the sums of the deconvoluted peaks, indicating good fitting quality; (b) and (d) calculated surface Si-O bond fraction for (b) a-Si and (d) SiN_x samples irradiated in argon (red) and ambient air (black).

impurity < 5 ppm) argon gas filled glass tubes. Since gamma rays are highly penetrating in glass, the sealing tube has a minimal impact on the irradiation dose received by the sample. The Si-O bond fraction hardly increases in the sample irradiated in argon (Fig. 5-6b), illustrating the suppression of oxide growth. A similar trend was found in SiN_x films as shown in Figs. 5-6c and

5-6d, which confirms that accelerated surface oxidation is also present in SiN_x devices exposed to gamma radiation in air.

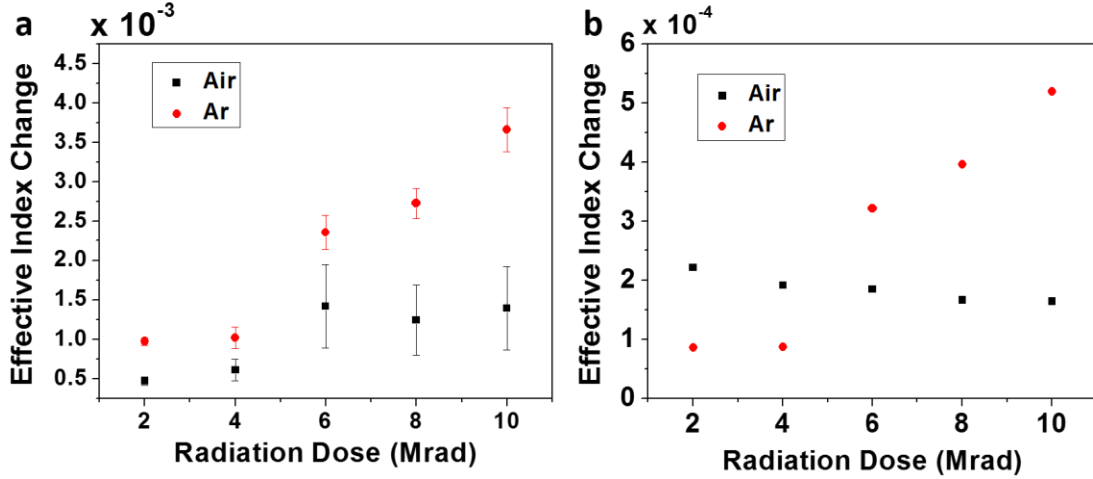


Figure 5-7. Dependences of refractive index changes on cumulative gamma radiation dose in (a) a-Si and (b) SiN_x inferred from optical resonator measurements.

The impact of surface oxidation on optical resonance drift is characterized by sequentially irradiating resonator samples multiple times with 2 Mrad dose increments up to a total cumulative dose of 10 Mrad. Optical transmittance of the devices was collected before and after every irradiation session. The radiation-induced resonant wavelength shift calculated from Eq. 1 was measured in multiple (5 or more) devices, and the average spectral shift $\overline{\Delta\lambda}$ was used to infer the core material index change via:

$$\Delta n_{eff} = \frac{n_g \overline{\Delta\lambda}}{\lambda_r}, \quad (2)$$

where λ_r denotes the resonant wavelength, n_g represents the mode group index, and Δn_{eff} gives the effective refractive index change of the waveguide mode. The group index n_g is related to the free

spectrum range in the wavelength domain (FSR, defined as the spacing between two adjacent optical resonant peaks) by:

$$n_g = \frac{\lambda_r^2}{\text{FSR} \cdot L}, \quad (3)$$

where L is the roundtrip length of the optical resonator. The radiation-induced index change in a-Si and SiN_x measured using this method are plotted in Fig. 5-7. The error bars in Fig. 5-7 take into account the experimental uncertainty due to both temperature fluctuations and sample-to-sample variations. In Fig. 5-7b, the error bars are small ($< 10^{-5}$) and thus hardly visible from the plot. For both a-Si and SiN_x, their refractive indices increase monotonically with increasing radiation dose when irradiated in argon. The index increase follows approximate linear dependences on cumulative total radiation dose in both materials. Since the possibility of radiation-induced crystallization is excluded, the observation suggests that densification or compaction of the amorphous atomic network is the likely cause of the index increase [23]. In comparison, the index increase is retarded in devices irradiated in ambient air and plateaus beyond 6 Mrad dose in a-Si. In SiN_x, its refractive index drops slightly after an initial rise at 2 Mrad dose. Since silicon dioxide has a lower refractive index ($n_{\text{SiO}_2} = 1.45$) than those of a-Si ($n_{\text{a-Si}} = 3.6$) and SiN_x ($n_{\text{SiN}_x} = 2.1$), the trend is attributed to a surface oxide formation which counteracts the index increase due to densification.

5.4 Gamma Radiation Damage in a-SiC Materials and Devices

Silicon carbide (SiC) has been considered as leading candidate in radiation harsh environment due to its strong Si-C covalent bonding. In Micro- (or Nano-) electromechanical systems, MEMS (or NEMS), SiC exhibits advantages over other silicon based material owing to its large band gap, low absorption in telecommunication band and high bulk modulus. In this section, we focused on detecting radiation induced refractive index shift in SiC materials using NOMS devices as testing vehicles. Amorphous silicon carbide (a-SiC) is chosen to be our material of interest as a-SiC can be easily deposited on any substrate via chemical vapor deposition (CVD). As a radiation resistant material, radiation induce effect in SiC material are notably small which can be beyond the detection limit of conventional techniques. To improve detection capability, optical resonators are chosen to be our testing platform as cavity enhancement allows us to detect index change to the order of 10^{-5} .

Fabrication of SiC devices followed the standard Si microfabrication processes. Prior to SiC growth, a 1 μm PECVD silicon dioxide was first deposited onto silicon wafers, and then 170 nm thin film silicon carbide was grown using the same PECVD tool. Electron beam resist ZEP 520A was subsequently spun onto the film, forming an ~ 700 nm layer. The resonator pattern was written by an Elionix electron beam lithography system at an acceleration voltage of 120 KV and a 10 nA beam current. Subsequently, the patterns were transferred to the film by reactive ion etch (RIE) with a mixture of CF_4 and CHF_3 gases. The as-fabricated silicon carbide rib waveguide has an

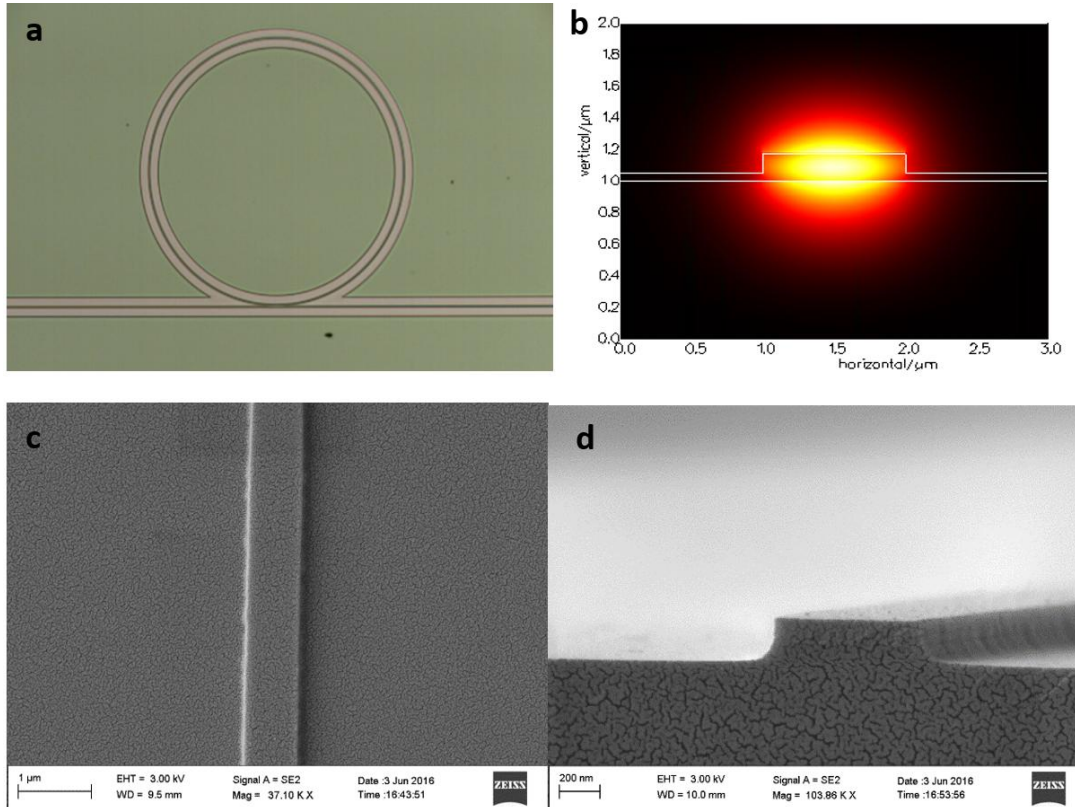


Figure5- 8. (a) *Optical microscope image silicon carbide micro-resonator;* (b) *Optical mode of the fabricated silicon carbide waveguide with 1 μm width;* SEM micrographs are shown (c) *top view and (d) cross section, respectively.*

etching depth of 120 nm and varied width, ranging from 1 μm to 1.6 μm . The radius of the resonator was chosen to be 150 μm to ensure low bending losses. Resist stripping included one hour soaking in N-Methyl-2-pyrrolidone and sonicating for 3 minute. To ensure complete removal of resist and fluorocarbon polymer residue formed in RIE, the device was further piranha cleaned for 10 minutes. Finally, another 1 μm silicon oxide was deposited onto the device as an upper cladding. Figure 5-8a shows a top view optical microscope image of a fabricated micro-ring resonator and its corresponding waveguide mode is provided in 8b. To further observe the waveguide profile, both top and cross section view SEM micrographs were taken and shown in Figure 5-8c and 5-8d, respectively. The SEM images clearly indicated no etching residue was present.

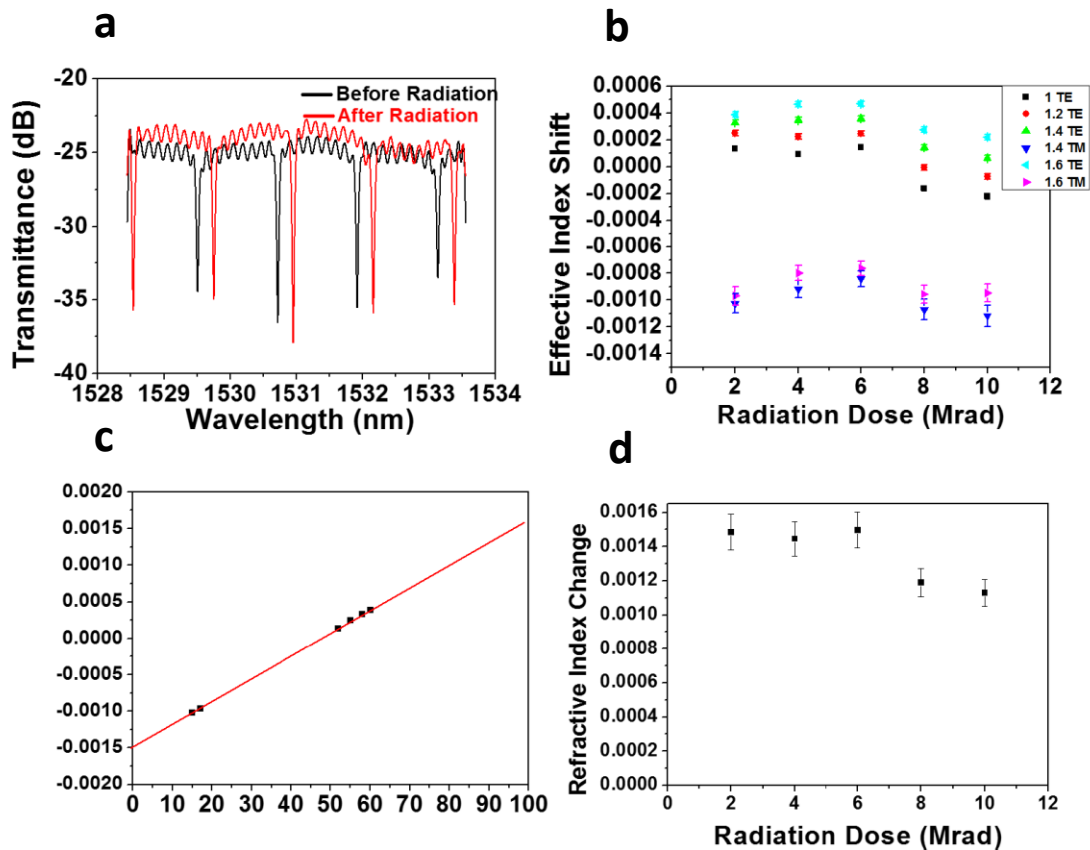


Figure 5-9. (a) Transmission spectra of silicon carbide resonator before and after 2 Mrad gamma radiation in air; (b) quantitative analysis of peak shift with respect to radiation dose; (c) linear extrapolation of effective index change, the result shows a 0.0015 index change in silicon carbide material after receiving 2 Mrad. (d) silicon carbide core refractive index change with radiation dose.

Optical transmission spectrum was characterized on a Newport Auto Align workstation and an optical vector analyzer (LUNA Technologies OVA-5000) with a built-in tunable laser. Near-infrared wavelength light was coupled in and out through the bus waveguide using tapered lens-tip fiber. All measurements were performed at a constant temperature

of (19.7 ± 0.2) °C. The temperature stability ensures that index change down to 2×10^{-5} can be reliably measured.

The samples were irradiated multiple times with 2 Mrad increment in total dose. Figure 5-9a illustrates the transmission spectrum of a SiC resonator near one of its resonance peaks. A peak red shift was clearly discernable after the sample received 2 Mrad radiation. The refractive index modification is calculated from equation 2 and 3:

The index change is plotted in Figure 5-9b. It is interesting to note that the refractive index shifts of those devices irradiated in air exhibit a "saturated" behavior, where the peak shift stays at the same position as dose increases. Similar trend is found in devices with different modal confinement in SiC core. By linearly extrapolating the refractive index shift with respect to modal confinement factor to 100%, we are able to determine the material index change after radiation. The trend is plotted in Figure 9c. We conclude that radiation induced refractive index change in SiC and SiO₂ cladding are in the same order of magnitude but differ in sign, where SiC tends to increase in index while SiO₂ cladding index decreases.

5.6 Conclusion

In summary, we quantified for the first time (to the best of our knowledge) refractive index increase in a-Si and SiN_x materials induced by gamma irradiation through on-chip optical resonator characterization. No measurable changes in optical loss were observed in both materials. When the devices were irradiated in an inert (argon gas) environment, index increase in a-Si and SiN_x follow approximate linear dependence on the total radiation dose attributed to radiation-induced

amorphous network densification in the materials. The index increase is retarded in devices irradiated in ambient air due to the added effect of surface oxidation confirmed by our XPS analysis. The quantitative information on gamma radiation effects in a-Si and SiN_x devices provides useful design guidelines for photonic systems operating in radiation-harsh environments. In the meantime, we quantified radiation induced index modification in a-SiC and we developed a technology to separate core and cladding index modification. It worth noting that the index change of a-SiC and SiO₂ cladding are in opposite direction. We therefore are able to build gamma radiation hard photonic devices by carefully adjust modal confinement factor to allow cancelling out the index change contributions from core and cladding to the effective index.

Reference

- (1) M. Zerler, SPIE Prof., October (2015)
- (2) F. De Leonardis, B. Troia, C.E. Campanella, F. Prudeniano, and V.M. Passaro, IEEE Trans. Nucl. Sci. **62**, 2155 (2015)
- (3) S.S. El Nasr-Storey, F. Boeuf, C. Baudot, S. Detraz, J.M. Fedeli, D. Marris-Morini, L. Olantera, G. Pezzullo, C. Sigaud, C. Soos and J. Troska, IEEE Trans. Nucl. Sci. **62**, 329 (2015).
- (4) P. Dumon, R. Kappeler, D. Barros, I. McKenzie, D. Doyle and R. Baets, In *Optics & Photonics 2005* (International Society for Optics and Photonics. 2005) p. 58970D
- (5) S. Bhandaru, S. Hu, D.M. Fleetwood and S.M. Weiss, 2015. IEEE Trans. Nucl. Sci. **62**, 323 (2015).
- (6) R. Sun, J. Cheng, J. Michel and L.C. Kimerling, Opt. Lett. **34**, 2378 (2009).
- (7) J.F. Bauters, M.J. Heck, D.D. John, J.S. Barton, C.M. Bruinink, A. Leinse, R.G. Heideman, D.J. Blumenthal and J.E. Bowers, Opt. Express, **19**, 24090 (2011).
- (8) Y.H.D. Lee and M. Lipson, IEEE J. Sel. Topics Quantum Electron., **19**, 409 (2013)
- (9) J.J. Wathen, V.R. Pařán, R.J. Suess, K.Y. Wang, A.C. Foster and T.E. Murphy, Opt. Express, **22**, 22730 (2014)
- (10) Y. Okawachi, K. Saha, J.S. Levy, Y.H. Wen, M. Lipson and A.L. Gaeta, Opt. Lett. **36**, 3398 (2011)
- (11) J.M. Boudry and L.E. Antonuk, 1996. Radiation damage of amorphous silicon, thin-film, field-effect transistors. Med. Phys., **23**, 743 (1996)
- (12) L.E. Antonuk, J. Boudry, J. Yorkston, C.F. Wild, M.J. Longo and R.A. Street, Nucl. Instrum. Meth. A, **299**, 143 (1990)
- (13) D. Nikolić, K. Stanković, L. Timotijević, Z. Rajović and M. Vujisić, Inter. J. Photoenergy (2013)
- (14) J.R. Srour, G.J. Vendura, D.H. Lo, C.M.C. Toporow, M. Dooley, R.P. Nakano and E.E. King, IEEE Trans. Nucl. Sci., **45**, 2624 (1998)
- (15) S. Grillanda, V. Singh, V. Raghunathan, F. Morichetti, A. Melloni, L.C. Kimerling, and A.M. Agarwal, Opt. Lett. **41**, 3053 (2016)
- (16) V. Brasch, Q.F. Chen, S. Schiller and T.J. Kippenberg, Opt. Express, **22**, 30786 (2014)
- (17) F. Morichetti, S. Grillanda, S. Manandhar, V. Shutthanandan, L.C. Kimerling, A. Melloni and A.M. Agarwal, 2016. ACS Photon. **3**, 1569 (2016)
- (18) J. Hu, N. Carlie, L. Petit, A. Agarwal, K. Richardson, and L. C. Kimerling, J. Lightwave Technol. **27**, 5240-5245 (2009)
- (19) R.G. Elliman, J.S. Williams, W.L. Brown, A. Leiberich, D.M. Maher and R.V. Knoell, Nucl. Instrum. Meth. B **19**, 435 (1987)
- (20) M.P. Krulikovskaya, A.A. Kuzub, L.I. Chirko and A.M. Shalaev, Bull. Acad. Sci. USSR, Phys. Ser., **6**, 37 (1985)
- (21) H. Cui, E.T. Pashuck, Y.S. Velichko, S.J. Weigand, A.G. Cheatham, C.J. Newcomb and S.I. Stupp, Science, **327**, 555 (2010))
- (22) S. Bhandaru, E.X. Zhang, D.M. Fleetwood, R.A. Reed, R.A. Weller, R.R. Harl, B.R. Rogers and S.M. Weiss, IEEE Trans. Nucl. Sci., **59**, 781 (2012)
- (23) F. Piao, W.G. Oldham and E.E. Haller, J. Non-cryst. Solids, **276**, 61 (2000)

Chapter 6. Conclusion and Future Work

5.1 Conclusion

In my PhD work, I have exploited various novel materials including chalcogenide glass, garnet oxide, and silicon based nitride, carbide and oxide. Leveraging the merit of these materials we have demonstrated world record devices and applications.

In chapter 2, we have developed a fabrication technology in chalcogenide glass photonics that both is compatible with current CMOS industry fabrication line, but also featuring low waveguide losses. We have successfully demonstrated a record low propagation loss of 0.5 dB/cm in single mode waveguide core. In addition, a then record high-Q micro-disk resonator with Q factor up to 1.2 million was also achieved.

In chapter 3, we leveraged this platform and integrated a supercontinuum broad band and coherence light source onto a chemical sensor chip, for the first time. This chip has a supercontinuum spanning over half of an octave and we designed serpentine waveguides which served as both a light source and an evanescent chemical sensor.

In chapter 4, we designed and fabricated a monolithically integrated magneto-optical TM isolator with the lowest insertion loss and highest isolation ratio. We also demonstrated the first monolithically integrated NRPS based TE isolator with the highest isolation ratio and smallest device footprint.

In chapter 5, we focused on radiation induced damage effect in photonic materials and devices. Our systematic study has developed a quantitative relationship between radiation induced refractive index modifications with respect to increasing radiation dose in a-Si, SiN_x and SiC. We also proposed a design of radiation-hard photonic devices.

5.2 Future work

It worth mention that the devices we demonstrated in this thesis are not the ultimate performance and applications. There are still many interesting future work that worth exploring.

Our supercontinuum integrated chemical sensor only spans up to $\sim 2\mu\text{m}$, which is still far from infrared fingerprint region. To precisely identify one chemical out of a solution. We need to track multiple absorption peaks of the analyte. Therefore, a supercontinuum source that expands more than one octave while maintaining miniaturized sensor size. This could be achieved by developing a palm sized femto-second laser emitting mid-IR light.

In on-chip magneto-optical isolators, though we managed to demonstrate a TM isolator with world record low insertion loss and high isolation ratio. However, the performance of our TE isolator is still far from commercial use. Further optimization of device fabrication and material deposition technology to achieve higher figure of merit. In addition, it worth mention that our ring resonator based isolator only operate at a bandwidth $\sim 0.01\text{nm}$. This strongly limited the full scale application of isolators to various on-chip laser systems. A growing need is to develop a low insertion loss, monolithically integrated broadband isolators. The broadband requirement can be achieved by a Mach-Zender Interferometer (MZI). According to the simulation result shown in figure 4-9, relying

on a MZI platform would inevitably sacrifice higher insertion loss, a near 30 nm bandwidth would significantly improve its application variety. By applying the same technology we developed in this thesis, a MZI isolator could be equally demonstrated.

We have also presented a systematic study on gamma radiation induced effects in silicon photonic materials. The fundamental damage event and mechanism, however, is still unclear. A detailed material study combining SIMS, molecular dynamic (MD) simulation with better imaging technology, such as HAADF imaging and in-situ dynamic imaging, could further provide insight in the interaction between high energy ion and substrate atoms. In addition, Fourier transform of high resolution electron diffraction pattern gives the radial distribution function (RDF) of amorphous structures. Comparing the RDF of the samples before and after radiation would be of great interest in providing the change of amorphous networks induced by radiation.